CHARACTERIZATION AND APPLICATIONS OF CVD-GROWN GRAPHENE FOR PASSIVE MICROWAVE DEVICES

A THESIS

Submitted to the Delhi Technological University

for the Award of the degree of

DOCTOR OF PHILOSOPHY

in

APPLIED PHYSICS

by

KAMLESH PATEL

Under the guidance of

DR. PAWAN KUMAR TYAGI

DEPARTMENT OF APPLIED PHYSICS

DELHI TECHNOLOGICAL UNIVERSITY

DELHI- 110042 INDIA

AUGUST 2017

CHARACTERIZATION AND APPLICATIONS OF CVD-GROWN GRAPHENE FOR PASSIVE MICROWAVE DEVICES

by

KAMLESH PATEL

DEPARTMENT OF APPLIED PHYSICS

Under the guidance of

DR. PAWAN KUMAR TYAGI

Submitted to

in fulfilment of the requirements of the degree of

DOCTOR OF PHILOSOPHY

to the

DELHI TECHNOLOGICAL UNIVERSITY

DELHI- 110042 INDIA

AUGUST 2017

DEDICATED

To

MY PARENTS, WIFE& SON

DECLARATION

This is to certify that this thesis entitled **"CHARACTERIZATION AND APPLICATIONS OF CVD-GROWN GRAPHENE FOR PASSIVE MICROWAVE DEVICES"** being submitted for the award of degree of Doctor of Philosophy to Delhi Technological University India, embodies the original research work carried out by me under the supervision of Dr. Pawan Kumar Tyagi, Department of Applied Physics, Delhi Technological University, India. The results obtained in this thesis have not been submitted in part or full to any other University or institution for the award of any degree or diploma.

(Kamlesh Patel)
Research scholar   **Date:**
Enrollment No.: 2K11/PhD/AP/08   **Place: Delhi**

Dr. Pawan Kumar Tyagi
(Supervisor)
Assistant Professor
Department of Applied Physics
Delhi Technological University
Delhi, India

DELHI TECHNOLOGICAL UNIVERSITY

CERTIFICATE

This is to certify that the Ph.D. thesis entitled **"CHARACTERIZATION AND APPLICATIONS OF CVD-GROWN GRAPHENE FOR PASSIVE MICROWAVE DEVICES"** submitted to Delhi Technological University India, for the award of degree of Doctor of Philosophy is based on the original research work carried out by me under the supervision of Dr. Pawan Kumar Tyagi, Department of Applied Physics, Delhi Technological University India. It is further certified that the work embodied in this thesis have not submitted in part or full to any other University or institution for the award of any degree or diploma.

Kamlesh Patel
(Enrollment No.: 2K11/PhD/AP/08)

This is certified that the above statement made by the candidate is correct to the best of our knowledge.

Dr. Pawan Kumar Tyagi
(Supervisor)
Assistant Professor
Department of Applied Physics
Delhi Technological University
Delhi, India

Prof. Suresh C. Sharma
Head of Department
Department of Applied Physics
Delhi Technological University
Delhi, India

ACKNOWLEDGEMENTS

This thesis is the result of about five years of work in which I have been supported by many people. It is a pleasant aspect that God has given me an opportunity to express my gratitude for all of them.

First of all, I would like to express my greatest gratitude to my supervisor **Dr. Pawan Kumar Tyagi** for his proficient guidance and continued encouragement for the fulfilment of the research work. With great pleasure, I express my heartfelt pleasure for his advice, fruitful discussions, numerous suggestions, constructive criticism, and the precious time that he spared for me throughout the period of my research.

I am highly thankful to **Prof. Suresh C. Sharma, Head of Department, Applied Physics, DTU** for his support to my research work and providing necessary suggestions. I am grateful to **Prof. R. K. Sinha** for providing encouragements during my Ph.D.I gratefully acknowledge the suggestions and support provided by **Dr. Amrish K. Pawar**, **Dr. Mohan S. Mehata**, **Dr. Nitin Puri** and other faculty members of Department of Applied Physics. It gives me immense pleasure to thank all non-teaching staff of the Department of Applied Physics for their cooperation and moral supportduring my research work. I express my sincere gratitude to the faculty of Delhi School of Management, DTU for their encouragements during course work.

I humbly acknowledge constructive suggestions from **Prof. P. K. Bhatnagar, Prof. Enakshi K. Sharma**, **Prof. Avinashi Kapoor**, **Prof. Mridula Gupta**and colleagues at my work place, Department of Electronic Science, University of Delhi South Campus. Special thanks mentioned for Mr. Pulkit Sharma and Ms. Shailesh Jayant for helping me on MATLAB programming.

Besides this, I am very thankful to all my Ph. D. colleagues, Ms. Lucky Krishnia, Ms. Reetu Kumari, Mr. Vinay Kumar, Dr. Zaniab Naqvi, Ms. Geetanjali, Ms. Anshika, Mr. C. K. Bohra and Mr. Sandeep for their continuous cooperation during this research work.I gratefully acknowledge the facility support provided by Nanofabrication lab at Delhi Technological University, Delhi, which has CVD facilities and various characterization techniques namely, Raman, AFM, XRD etc. I am thankful to Department of Electronic Science, University of Delhi, South Campus, New Delhi and CSIR-National Physical Laboratory for providing me the support to carry out my research work.

I also acknowledge the financial assistance provided by DST-SERB, Fast Track Program (SR/FTP/PS-055/2012) and DST-FCT, Portugal bilateral Program (INT/PORTUGAL/P-13/2013) at DTU and R & D scheme grant 2014-2015 of University of Delhi during the period of my research.

I am indebted to my parents for everything that they have given me throughout my career. I would like to extend my thanks to my wife for her timely help, continuous support and encouragements throughout my research work. I specially mention the smile of my son which refreshes me every time and his innocent understanding.

Finally, I thank to all those who helped and supported me. Thank you so much!

Date: (**Kamlesh Patel**)

Place: Delhi

ABSTRACT

In this thesis work, the graphene layer transferred on two substrates, glass and quartz and bilayer graphene deposited on copper substrates were characterized using the multilayer microstrip line technique. Graphene transferred on both glass and quartz substrates of the dimension $1''\times1''$ were procured from Graphene Industries, USA. Bilayer graphene was grown by using Hot Filament Chemical Vapor Deposition (HFCVD) system on Cu sheet at two different temperatures 850°C and 950 °C. A new de-embedding method was adopted and verified with standard ABCD de-embedding method by comparing obtained results such as effective relative permittivity, phase velocity and group velocity in 100 MHz - 10 GHz range.We found occurrence of anomalous dispersion in single layer graphene in terms of higher group velocity than phase velocity. Then, the intrinsic properties, complex relative permittivity and refractive index of single layer graphene (SLG) and bilayer graphene (BLG) have been obtained by using expressions of conformal mapping after S-parameter measurements in 10 MHz to 26.5 GHz range. In SLG, the real part ($\boldsymbol{\varepsilon_r'}$) of relative permittivity was found ~ 6.71 to 7.62 whereas the imaginary part ($\boldsymbol{\varepsilon_r''}$) is decreased from ~ 9.58 @ 10 MHz to 8.47 @ 1.92 GHz. For both BLG samples, same values of $\boldsymbol{\varepsilon_r'}$ and $\boldsymbol{\varepsilon_r''}$ are obtained in the range of 5.58 – 5.67 and 6.97 – 7.025, respectively. The value of the refractive index (*n*) and extinction coefficient (κ) for SLG are in the range of 2.95 - 3.15 and 1.43 - 1.52, respectively in the frequency range of study. In both BLG samples, same values of *n* and κ were obtained and these are ~ 2.69 and ~ 1.28, respectively.

To observe the behaviour of waves in SLG and BLG, phase velocity, group velocity and optical effective mass have been evaluated. In BLG, high phase velocity

and group velocity represent faster propagation of energy than in SLG. The mass ratio $\left(m_{op}^*/m_0\right)$ was found from ~10^{-10} @10 MHz to ~ 0.2×10^{-8} @ 26.5 GHz and ~ 0.16×10^{-8} @ 26.5 GHz, respectively for SLG and BLG, where the free electron mass, $m_0 = 9.107 \times 10^{-31}$ kg. In addition, the lower effective mass of photons in BLG has resulted due to smaller refractive index, which in turn suggests minor interaction between photon-charge carriers.

Theoretically, potential application of graphene as an efficient transparent conducting electrode was investigated in silicon heterojunction cells in n/p and p/n configurations and cell parameters were analyzed using AFORS-HET (Automat FOR Simulation of HETero-structures) software under air mass 1.5 (AM1.5) illuminations with power density of 100 mW/cm^2.Independent effects of the layer's parameters on the performance of cell structure and insights behind the cell responses have been discussed. After optimizing the parameters of both layers of graphene and silicon, an efficiency of 9.812 % was achieved and an optimum efficiency of 11.47 % has been achieved for 100 μm thick commercial silicon layer in p-graphene/n-cSi cells, whereas simulation efficiency of 13.66 % was achieved and an optimum efficiency of 8.491 % has been achieved for commercial silicon of same thickness in n-graphene/p-cSi cells.Finally, we demonstrate that p-type and n-type multilayer graphene can act as an efficient transparent conducting electrode in graphene/silicon heterojunction cell.

LIST OF PUBLICATIONS

Paper published in the referred international journals

(Included in the thesis)

1. **Kamlesh Patel** and Pawan K. Tyagi, "*Single layer graphene possessing anomalous dispersion with exotic microwave transmission and dielectric properties,*" **Journal of Alloys and Compounds** 706 (2017) 250-259.
   http://dx.doi.org/10.1016/j.jallcom.2017.02.184 (**IF = 3.014**).

2. **Kamlesh Patel** and Pawan K. Tyagi, "*Optical effective mass of photons in single and bilayer graphene in 10 MHz to 26.5 GHz frequency range,*" **Carbon** 121 (2017) 56-62.
   http://dx.doi.org/10.1016/j.carbon.2017.05.057(**IF = 6.194**).

3. **Kamlesh Patel** and Pawan K. Tyagi, "*P-type multilayer graphene as a highly efficient transparent conducting electrode in silicon heterojunction solar cells.*" **Carbon** 116 (2017) 744-752.
   http://dx.doi.org/10.1016/j.carbon.2017.02.042 (**IF = 6.194**).

4. **Kamlesh Patel** and Pawan K. Tyagi, "*Multilayer graphene as a transparent conducting electrode in silicon heterojunction solar cells,*" **AIP Advances**5 (2015) 077165.
   http://dx.doi.org/10.1063/1.4927545 (**IF = 1.444**).

Paper published in the referred international journals

(Not included in the thesis)

1. Pranjala Tiwari, **Kamlesh Patel**, Lucky Krishnia, Reetu Kumari, Pawan K. Tyagi, "*Potential application of multilayer n-type tungsten diselenide (WSe$_2$) sheet as transparent conducting electrode in silicon heterojunction solar cell,*" **Computational Materials Science** 136 (2017) 102 – 108.
   https://doi.org/10.1016/j.commatsci.2017.04.026 (**IF= 2.086**).

2. Rimjhim Chaudhary, **Kamlesh Patel**, Ravindra K. Sinha, Sanjeev Kumar, and Pawan K. Tyagi, "*Potential application of mono/bi-layer molybdenum disulfide*

(MoS₂) sheet as an efficient transparent conducting electrode in silicon heterojunction solar cells," **Journal of Applied Physics** 120 (2016) 013104. http://dx.doi.org/10.1063/1.4955071 (**IF=2.10**).

3. **Kamlesh Patel** and Pawan K. Tyagi, **"*Technological Advances in A-Si: H/c-Si Heterojunction Solar Cells*,**" **Int. J. Renewable Energy Research** 4(2) (2014) 528-538 (**IF=0.8**).

Paper published in the referred conference proceedings

(Not included in the thesis)

1. **Kamlesh Patel**, Neha, Pawan K. Tyagi, **"*Effective relative permittivity and characteristic impedance of graphene loaded microstrip line by scalar S-parameters*,**" **AIP Conference Proceedings** 1728, 020617 (2016); International Conference on Condensed Matter and Applied Physics (ICC 2015), Bikaner, Rajasthan, 30 -31 Oct, 2015.
http://dx.doi.org/10.1063/1.4946668.

2. **Kamlesh Patel**, Sushil Kumar, O. S. Panwar, Sreekumar C., C. M. S. Rauthan and Pawan Tyagi, "*New approaches for the performance improvement of Heterojunction and HIT solar cells*," **Proc. of 27th European Photovoltaic Solar Energy Conference and Exhibition** (EU PVSEC), 2648-2652 (2012), Frankfurt, Germany, 24-28 Sept, 2012.

CONTENTS

LIST OF FIGURES

(b)graphene/glass, (c) quartz and (d) graphene/quartz.

effective band density $N_C/N_V = 3 \times 10^{19}$ cm^{-3}, the electron affinity $\chi =$ 4.05 eV and thickness 100 μm. The other parameters of silicon as well as p-type graphene are given in Table 6.2.

respectively.

LIST OF TABLES

LIST OF ABBREVATIONS

AFM   Atomic Force Microscopy

AFORS-HET   Automat FOR Simulation of HETero-structures

AM   Air Mass

BLG   Bilayer Graphene

CNT   Carbon Nanotube

CPW   Coplanar Waveguide

CVD   Chemical Vapor Deposition

EQE   External Quantum Efficiency

FF   Fill Factor

FLG   Few Layer Graphene

FR   Flame epoxy Resin

HFCVD   Hot Filament Chemical Vapor Deposition

HOPG   Highly Oriented Pyrolytic Graphite

IQE   Internal Quantum Efficiency

ITO   Indium Tin Oxide

SLG   Single Layer Graphene

SdH   Shubnikov-de Hass

SiC   Silicon Carbide

TCE   Transparent Conducting Electrode

TCO   Transparent Conducting Oxide

VNA   Vector Network Analyzer

Chapter 1

Introduction

1.1. Basic structure and electronic properties of graphene

1.1.1 Graphene: an introduction

Graphene is one-atom-thick planar sheet of sp^2-bonded carbon atoms where atoms are tightly packed into a two-dimensional (2D) honeycomb crystal lattice [1, 2]. First time in 1962, term "graphene" was given by Hanns-Peter Boehm to a single-layer carbon foil [3]. Furthermore, graphene is known as a basic building block of all types of allotropes of carbon having different dimensionality including graphite, charcoal, carbon nanotube and fullerenes. Initially, graphene was presumed not to exist in the free-state, and was believed to be unstable because of long wavelength fluctuations. According to the Mermin Wagner theorem [4] it formed the curved structures such as soot, fullerenes and nanotubes. Suddenly in 2004, this incredible material turned into reality, when free-standing single layer of graphene was unpredictably found and successfully isolated using a mechanical exfoliation method by Prof. A. K. Geim and Dr. K. S. Novoselov at Manchester University [5]. Theoretically, graphene was considered as a parent material for various graphitic structures such as graphite, charcoal, carbon nanotube and fullerenes, it was expected that graphene has an astonishing electronic and mechanical properties due to its honeycomb lattice and electronic band structure in close proximity to first Brillouin zone as shown in **Fig. 1.1** **[2, 6-7]**. The lattice structure has two carbon atoms per unit cell denoted as A and B at a distance ~1.42 Å and possesses two types of C-C bonds σ (red) and π (blue)

constructed from four valence orbitals (2s, $2p_x$, $2p_y$ and $2p_z$), here z-direction is taken along c-axis of graphene sheet. The hybridized fourth bond is associated with the overlap of p_z orbital and forms the bonding (π) and anti-bonding (π^*) (in blue) as illustrated in **Fig.1.1 (b) [2, 6]**.These π-bondings determine the electronic properties of graphene and participate in forming of valence (π) and conduction (π^*) bands in first Brillouin zone near to Fermi level. Electronic bands of graphene always form a cone that touches at the high symmetry points, known as Dirac points labelled as K and K′.
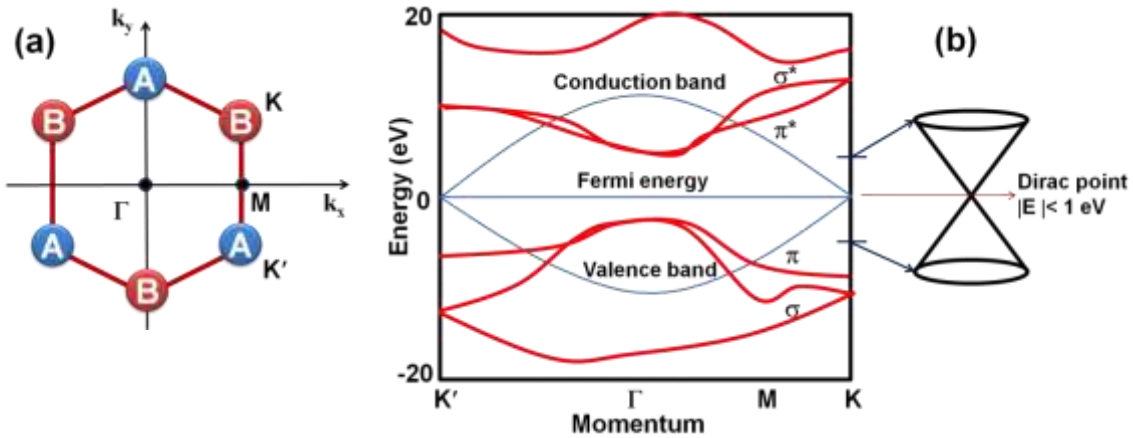
Fig.1.1 (a) Lattice and (b) electronic structure of graphene in Brillouin zone.

Due to this cone shape of electronic bands, graphene is considered as a gapless semiconductor. Near Dirac points, electronic dispersion is found to be linear where energy E and the carrier wave vector k $(=\sqrt{k_x^2 + k_y^2})$ can be related as $E = \hbar v_F k$, consequently carriers in graphene is considered as massless Dirac fermions **[2, 6],** here $\hbar$ is the reduced Planck's constant and $v_F \approx 10^6$ m/s is the electron Fermi velocity in graphene. It has been reported that in graphene, charge carriers can be tuned continuously between electrons and holes in concentration n as high as 10^{14} cm^{-2} **[1]** with mobility (μ) as high as 15,000 cm^2/Vs. The mobility can be further improved even

up to 100,000 cm^2/Vs at room temperature by chemical doping and 2×10^5 cm^2/Vs in suspended graphene **[8]**. Recently, it was reported that even at such high carrier concentration 10^{12} cm^{-2}, ballistic carrier transport with mean free path of $\sim 0.3\mu m$ occurs **[1].** Graphene is also reported to possess other extraordinary properties like an elastic stiffness of 340 N/m **[9]**, high intrinsic mobility ($\sim$200,000 cm^2/Vs) **[8, 10-11**], high thermal conductivity ($\sim$5000 W/mK) **[12]**,large specific surface area ($\sim$2630 m^2/g) **[13]** and Young's modulus ($\sim$ 1.0 TPa) **[9]**, high optical transparency as $\sim$2.3 % absorption of visible light only **[14].**

1.1.2 Comparison of single, bilayer and multilayer graphene

As graphene is a 2D material and electronic structure deeply depends on number of layers till it becomes a 3D limit of graphite at 10 layers **[15]**. Both single layer and bilayer graphene can be considered as a zero-bandgap semiconductor **[1, 7]**. For three or more layers, the electronic spectra becomes more complicated, which results in the appearance of several charge carriers **[5, 16]** and the conduction and valence bands start notably overlapping [**5, 15**]. This kind of behaviour for electronic bands distinguish single, bilayer and few layer (3 to <10) graphene to be considered as three types of graphene. Typical schematic of crystal structure and band structure of single layer graphene, bilayer graphene and trilayer graphene are illustrated in **Fig. 1.2**.

The bilayer graphene consists of two single layer graphene bounded together by weak van der Waals forces. As compared to AA stacking, AB stacking is more stable and explored widely (**Fig. 1.2c**). In bilayer, most of the low energy band dispersion characteristics are expressed by a tight binding calculation through the in-plane nearest neighbour coupling (i.e. hopping from A-B in both layers) and the interlayer coupling between A atom of one layer with B atom of second layer **[17]**. The bilayer' band has a

set of four parabolic bands in each of the two symmetries K and K′ points, which has

bonding π_1 and anti-bonding π_1^* (red) touching each other, whereas π_2 and anti-bonding

π_2^* (blue) develop a bandgap due to interlayer symmetry (**Fig. 1.2d**).
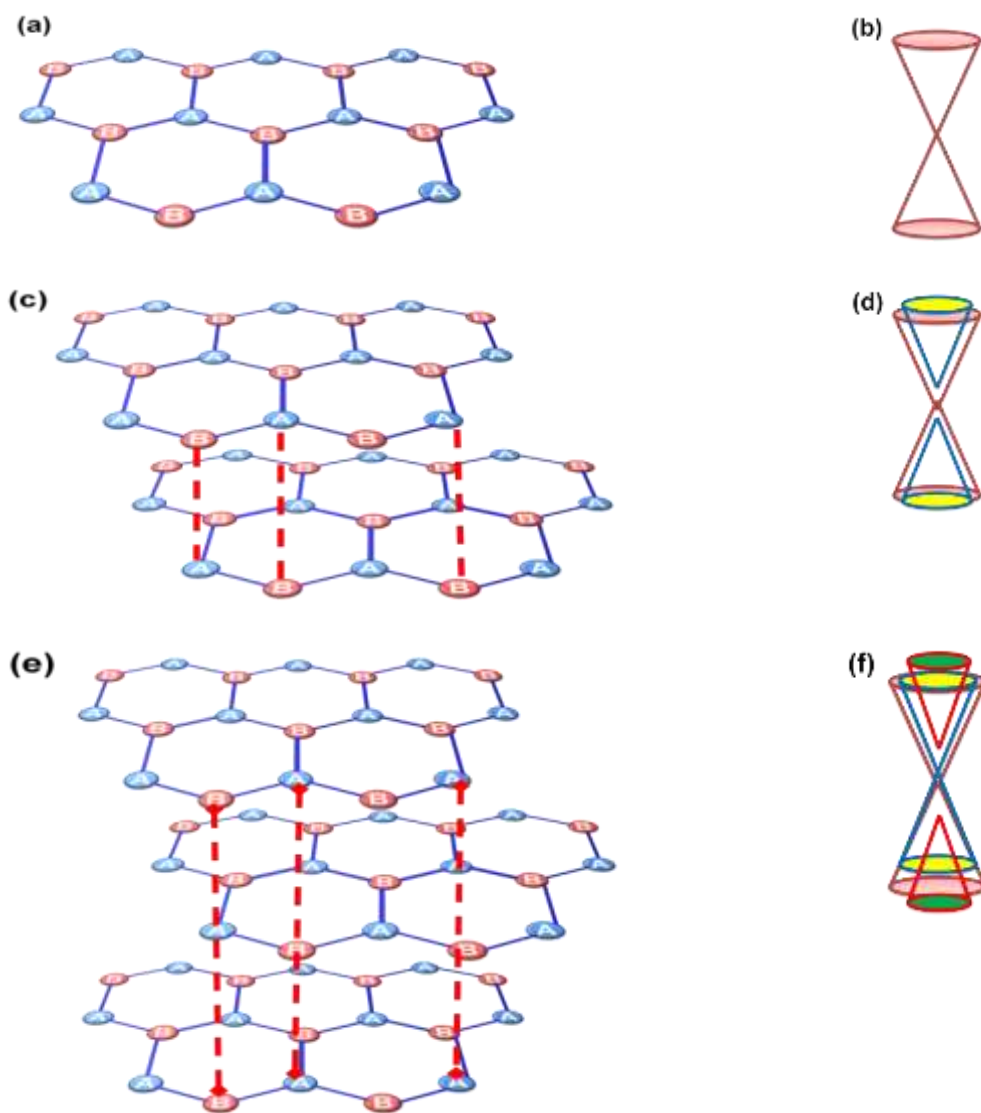
Fig. 1.2 Schematic crystal structure and band structure of single layer graphene (a and

b), bilayer graphene (c and d) and trilayer graphene (e and f).

Between carbon atoms in different layers, the minimum distance is ~3.4 Å **[18]**.

For more than two layers, a gap can be opened in a stack with Bernal ordering shown in

Fig. 1.2e, where the subband structure of a trilayer has included two touching parabolic bands and third one with Dirac dispersion, combining the features of both single layer and bilayer graphene. In experimental studies [18, 5], it has been shown that with an increasing number of layers, the graphene stack based system becomes more metallic and so several types of electron and hole like carriers have appeared near Dirac points. As an inhomogeneous charge distribution between layers becomes very dominant in transport properties of graphene stacks, it is therefore leading to 2D electron and hole systems, which only occupy a few graphene layers near the surface [18].

1.2 Importance of graphene for microwave applications

In recent reports, FLG is reported to exhibit carrier mobility as high as 10^5 cm^2/Vs at room temperature [19], controllable sheet resistance from 100 to 8.8 Ω/square, sheet carrier densities as high as 8.9×10^{14} cm^{-2} and carrier mean free path as large as ~0.6 μm [20] as well as impressive flexibility and controllable conductivity. Due to these properties, graphene has potential to be used in microwave devices operating in the terahertz (THz) and infrared portion of electromagnetic spectrum. Previously, it was demonstrated that due to high impedance greater than 10 kΩ, carbon nanotube (CNT) cannot be used in microwave devices as impedance of 50 Ω is essentially required for such devices [21]. Later on, this limitation has been overcome in perfectly dense and aligned arrays of CNTs. However, it is a very difficult to grow such array of CNT on a large substrate even if using CVD techniques. In graphene, impedance limitation does not occur. Recently, it was reported that a metallic pattern of coplanar waveguide (CPW) line on graphene can be fabricated and 50 Ω impedance with moderate losses in frequency band of 40 MHz-110 GHz was found [22].

Furthermore, in 2D graphene, conductivity has a finite minimum value of $\sigma_{min} = 4e^2/h$[1], where e is the electron charge and h is Planck's constant whereas in CNT, conductance is quantized and equivalent resistance is 6.3 kΩ, impedance of perfectly dense and aligned arrays of CNTs cannot be reduced to 50 Ω[22-23]. With such properties, graphene may be a realistic solution due to its mobility as high as 15000 cm^2/V and reported ballistic transport of micrometre range even on SiO$_2$ substrate [24]. These characteristics enable the design and fabrication of high mobility graphene-FET with cut-off frequency as high as 100 GHz [25-26].To use the graphene in microwave active and passive components such as patch antenna [27-29], graphene microstrip attenuator [30] etc., detailed studies on transmission and dielectric properties of graphene are to be known experimentally.

1.3 Graphene as a transparent conducting electrode in solar cells

In silicon heterojunction, transparent conducting electrode (TCE) develops a built-in electric field across the interface between the electrode and the active layer of silicon and transports the photo-generated charge carriers towards the cell terminals as well as serves the role of anti-reflector [31-33]. In order to perform the task effectively, the TCE must have low sheet resistance, high optical transmission and mobility, for example ITO has typically < 20 Ω/square with 85% optical transmission and mobility as high as > 20 cm^2/Vs [20, 31]. Recently, high mobility has been reported in multilayer graphene and makes it an emerging TCE material [20, 34 - 36]. In 2010, Bae et $al.$[37] reported that sheet resistance of multilayer graphene can be reduced to 10 Ω/square with 85 % optical transmission by stacking four monolayer graphene with chemical doping of HNO$_3$. In further advances, Khrapach et $al.$[20] reported that interaction of multilayer graphene film with FeCl$_3$ reduces its sheet resistance to 8.8 Ω/square with 84 % optical

transmission even for a carrier density as high as 8.9×10^{14} cm^{-2} with mean free path as large as ~0.6 μm. The chemical doping with HNO$_3$ as well as FeCl$_3$ makes graphene film strongly p-type [20, 37] whereas graphene became n-type by doping withZnMgandhydrazine monohydrate [38, 39] or via the aluminium nanoparticle decoration approach [40]. Furthermore, epitaxial graphene grown on silicon carbide has been found naturally n-doped [41]. Recently, in order to explore possible applications of graphene as TCE, few layer graphene (FLG) and graphite film grown by using chemical vapor deposition (CVD) were probed and observed to posses sheet resistance as low as 200 Ω/sq with 85 % transmission. Furthermore, it was reported that conductivity of graphene films can be enhanced by chemical doping with some volatile oxidants like HNO$_3$, SOCl$_2$, H$_2$O$_2$, and HCl [42]. Above-mentioned properties certify that multilayer graphene can be used as a new TCE material in the graphene/silicon heterojunction solar cells.

1.4 Techniques used for synthesis of single layer and multi layer graphene

Graphene can be synthesized by adopting both processes i.e. top-down and bottom-up. In a top-down process, graphene is derived by stripping layers from graphite. For example, method such as mechanical exfoliation or scotch tape stripping, ion sputtering, pulsed laser deposition, ball milling and arc discharge etc. are known to be top-down [43]. Since, in bottom-up, processes initiate at atomic scale and then build up by atom to atom to the desired shape, thickness or size. The examples of bottom-up processes are: graphitization of silicon carbide, wet chemical route, chemical vapour deposition (CVD), annealing solid sources, ion implantation etc. [43]. A detailed review

on these processes followed by characterization methods reported by Kim *et al.* (2010)

[44] is summarized here in Table 1.1 and Table 1.2.

Table 1.1: Bottom-up processes for graphene synthesis [44]

Method	Typical dimensions		Advantage	Disadvantage
	Thickness	Lateral		
confined self assembly	single layer	1000s nm	thickness control	existence of defects
CVD	few layers	very large (cm)	large size; high quality	small production scale
arc discharge	single-, bi-, and few layers	few 100 nm to a few μm	can produce ~10 g/h of graphene	low yield of graphene; carbonaceous impurities
epitaxial growth on SiC	few layers	up to cm size	very large area of pure graphene	very small scale
reduction of CO	multiple layers	sub-μm	unoxidized sheets	contamination with α-Al$_2$O$_3$ and α-Al$_2$S
unzipping of carbon nanotubes	multiple layers	few μm long nanoribbons	size controlled by selection of the starting nanotubes	Expensive starting material; oxidized graphene

A brief review for some of these techniques is given as follows with regard to the

realisation of graphene **[45]**.

Table 1.2: Top-down processes for graphene synthesis [44]

	Typical dimensions			
Method	**Thickness**	**Lateral**	**Advantage**	**Disadvantage**
directly from graphite				
Micromechanical exfoliation	few layers	μm to cm	large size and unmodified graphene sheets	very small scale production
direct sonication of graphite	single and multiple layers	μm or sub-μm	unmodified graphene; inexpensive	low yield; separation
superacid dissolution of graphite	mostly single layer	300-900 nm	unmodified graphene; scalable	use of hazardous chlorosulfonic acid; cost of acid removal
Electrochemical exfoliation/ functionalization of graphite	single and few layers	500-700 nm	single step functionalization and exfoliation; high electrical conductivity of the functionalized graphene	cost of ionic liquids
From graphite derivatives (graphite oxide (GO) or graphite fluoride)				
Li alkylation of graphite fluoride	single layer	Mm	large size; functionalized sheets; no oxygen functionality	cost of the starting material; restacking after annealing
chemical reduction of colloidal GO in water	single and multiple layer CRG	μm or sub-μm size	large sheet size; some routes use only water	some of these methods use hazardous chemicals; only dispersed in hydrophilic polymers
Thermal exfoliation/reduction of GO	single and few layer TRG	~500 nm	1-step exfoliation/reduction; short heating time; dry basis	high heating temperature; smaller sheet size
chemical reduction of organically treated GO	mostly single layer CRG	few 100 nm to a μm	colloidal stability in organic solvents; better exfoliation	low thermal stability; in situ chemical reduction degrades some polymers

Mechanical exfoliation

Graphene possessing high crystalline quality can be obtained through repeated peeling of highly ordered pyrolytic graphite (HOPG) using scotch tape and this method is recognized as mechanical exfoliation[1, 5]. It is well-known that in graphite, due to weak van der Waals force binding energy which is of the order ≈ 2 eV/nm^2 is responsible for stacking of the graphene layers along c-axis and force ~ 300 nN/μm^2 can peel off single layer graphene from graphite [46]. In this process, after repeated peeling, a graphene layer from adhesive tape is transferred on to SiO$_2$/Si substrate [5, 46]. The thickness of SiO$_2$ layer is taken either 90 nm or 280 nm which is able to distinguish the number of layers because graphene contrast on SiO$_2$ is maximized by about 12 % at 550 nm and can easily be identified by human eyes. [47]. This technique has limitations such as small size depending on grain size as well as physical dimension of HOPG and residues of adhesive tape on graphene surface which can suppress the mobility [10, 24].

Graphitization of silicon carbide

Ultrahigh vacuum heating of silicon carbide (SiC) nearly at 1400°C leads to sublimation of silicon consequently segregation of carbon results in graphene formation [48]. Highly corrugated surface covered by small graphene regions having non-uniform thickness [49] is main drawback of this technique. It was reported that this can be avoided by using C terminated SiC in place of Si terminated SiC [50]. The graphene coverage as large as 50 μm was reported by using this technique under Ar ambient. However, mobility drops by five times as compared to exfoliated graphene [51].

Wet chemical route

In this method, in order to weaken the van der Waals interaction first graphite is intercalated with various reactants and as a result graphene layer or graphene oxide gets obtained. In this process, first graphite precursor is reacted with either strong acids or oxidants to produce graphite oxide [52]. During this reaction, various hydroxyl and epoxide groups are attached to the carbon atoms in graphite oxide through covalent bonds [53-54] and severely distorted conjugated native graphitic structure [52]. Depending on reducing agents like hydrazine, dimethyl hydrazine and hydroquinone, obtained graphene oxide exhibits entirely different properties in terms of mobility, conductivity, layer number and size [52]. To overcome this, non covalent functionalization for conjugated carbon network in graphite is applied using 1-pyrene carboxylic acid [55] and 9-anthracene carboxylic acid [56]. However, non-covalent functionalization improves electrical properties but this technique is not scalable. This technique in general is mostly used to obtain graphene nanoribbons (GNR) through the chemical unzipping of carbon nanotubes [57].

Chemical vapor deposition (CVD)

In CVD process, carbon containing gases /liquids is used as a carbon source and pass through the high temperatures (@700-1100 °C: strongly depend on carbon precursors and catalyst) in the presence of a metal catalyst. Here the role of catalyst is to facilitate the decomposition of a gaseous or volatile carbon precursor and eventually leads to the nucleation of the graphene lattice. The growth mechanism of graphene on the metals is strongly influenced by several factors, including the carbon solubility limit in the metal, its crystalline nature, lattice parameters and thermodynamic parameters such as the temperature and pressure of the system. But the most influencing factors are bulk, sub-

surface and surface diffusion of carbon in/on the metal. However, if metals such as Co and Ni have intermediate-high solubility (0.1 atom %) then synthesis of graphene seems to be proceed by the combination of bulk diffusion into the metal at the elevated temperature, and segregation from bulk to the metal surface at the time of fast cooling (after the completion of the CVD process). In the case of very low carbon solubility metals (0.001 atomic %), like in Cu, the synthesis of graphene is limited to the diffusion of carbon atoms on the surface of the Cu. Furthermore, it is worth noting that single crystal substrates are highly desirable to grow the defect-free graphene films, but in practice for the large scale applications less expensive polycrystalline substrates of large grain size must be used. Here, transition metals (Cu, Ni, steel) serve as efficient catalysts in transforming hydrocarbons into graphitic materials [58] and graphite layers were obtained from either hydrocarbons or evaporated carbon on Nickel surface [59]. In typical CVD shown in **Figure 1.3**, a metal substrate such as Cu is kept into a furnace and heated to around 1000°C under low vacuum. Annealing of Cu increases grain size [37].

Details of some synthesis conditions reported for single to few layer graphene are given in Table 1.3 [43].
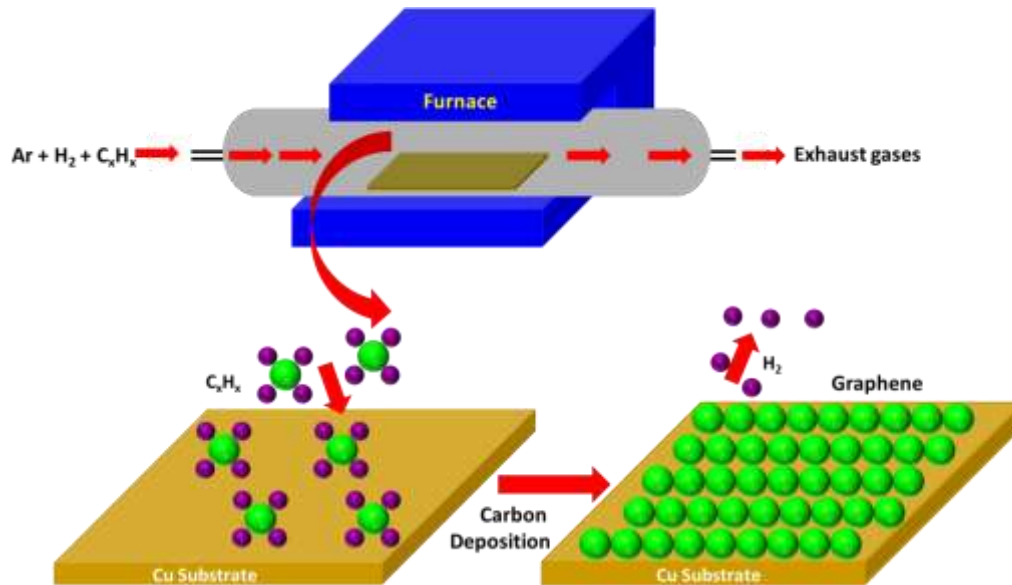
Fig. 1.3 Typical set up and process of CVD.

Annealing solid carbon sources

In this technique, various precursors such as Polymethylmetacrylate (PMMA) **[60]**, amorphous carbon **[61]** were spin-coated on Cu substrates and Polyacrylonitrile (PAN), Polystyrene (PS), PMMA **[62-63]**, C60 **[64]** on nickel substrates. In other ways, first carbon source is deposited on SiO_2/Si and then metal film is deposited though evaporation before annealing at high temperatures. This technique has advantage that obtained graphene need not to be transferred to other insulating substrate and it has been demonstrated for C60 **[64]** and self assembled monolayer (SAM) **[65]** on nickel thin film evaporated on SiO_2/Si. This technique has severe limitation like polycrystalline growth with small grain boundaries.

Table 1.3: Synthesis conditions used for single to few layer graphene [43]

Precursor	Type of CVD	Temperature	Pressure	Catalyst
Hydrocarbons	RF-CVD	-	Std P	Bi-metallic
Hydrocarbons	Epitaxial CVD	900 - 1000 ^{o}C	Std P	c-sapphire, Co/SiO$_2$ and H$_2$ (annealing)
Ethylene	RF-CVD			Bi-metallic
Methane				Ni and Cu in Ammonia
Methane	APCVD LPCVD UHVCVD		Atm, Torr Vacuum	Cu
Methane	PECVD	700 ^{o}C		Fe
Methane		1000 ^{o}C		Co on MgO Argon flow
Methane	PECVD	1400-1900 ^{o}C		6H SiC
Methane on HOPG				Fe
Iron tetra-pyridino-porphyrazine	Pyrolysis			

1.5 Aim of thesis

The behaviour of carriers in graphene is frequency dependant therefore properties like relative permittivity, refractive index, phase and group velocity, optical effective mass of photon in graphene have to be determined for effective utilization of graphene in microwave passive devices. Thus, it is essential to investigate these properties using a non-destructive method. The optical effective mass of photons inmicrowave frequency will help to understand interaction of photons with graphene atoms. When graphene get doped it becames n-type or p-type and its conductivity enhances with improvement in work function, which led to increase the developed built-

in potential at graphene/silicon interface. So, in order to have an effective application of doped graphene, the properties of graphene as well as silicon is required to optimize in solar cell simulation for high efficiency.

In this thesis, objectives of performed research work are:

(1) To extract the properties of CVD-grown graphene at microwave frequencies using non-destructive method.

(2) Validation of adopted simple and straight de-embedding method based on the propagation constants using microstrip line based measurement fixture.

(3) Determination of the complex relative permittivity and refractive index of single/bilayer graphene.

(4) To study group and phase velocity and dispersion relation in single/bilayer graphene in microwave frequency range.

(5) Potential application of FLG in Si based heterojunction solar cell as transparent conducting electrode.

References

[1] A. K. Geim, K. S. Novoselov, The rise of graphene, Nat. Mater. 6 (2007) 183-191.

[2] F. Giannazzo, S. Sonde, V. Raineri, Electronic properties of graphene probed at the nanoscale, in: S. Mikhailov (Ed.), Physics and Applications of Graphene Experiments, InTech, 2011, pp. 353-376.

[3] H. P. Boehm, R. Setton, E. Stumpp, Nomenclature and terminology of graphite intercalation compounds, Carbon 24(2) (1986) 241-245.

[4] N. D. Mermin, and H. Wagner, Absence of ferromagnetism or antiferromagnetism in one- or two-dimensional isotropic Heisenberg models, Phys. Rev. Lett. 17(22) (1966) 1133-1136.

[5] K. S. Novoselov, A. K. Geim, S. V. Morozov, D. Jiang, Y. Zhang, S. V. Dubonos, I. V. Grigorieva, A. A. Firsov, Electric field effect in atomically thin carbon films, Science306 (2004) 666-669.

[6] A. K. Geim, and A. H. MacDonald, Graphene: Exploring carbon flatland, Physics Today 60 (2007) 35-41.

[7] S. D. Sarma, S. Adam, E. H. Hwang, and E. Rossi, Electronic transport in two dimensional graphene, Reviews of Modern Physics 83 (2011) 407- 470.

[8] X. Du, I. Skachko, A. Barker, E. Y. Andrei, Approaching ballistic transport in suspended graphene, Nat. Nanotechnol. 3 (8) (2008) 491–495.

[9] C. Lee, X. Wei, J. W. Kysar, J. Hone, Measurement of the elastic properties and intrinsic strength of mono-layer graphene Science 321 (2008) 385–388.

[10] K. I. Bolotin, K. J. Sikes, Z. Jiang, M. Klima, G. Fudenberg, J. Hone, P. Kim, H. L. Stormer, Ultrahigh electron mobility in suspended graphene, Solid State Commun.146 (2008) 351-355.

[11] S. V. Morozov, K. S. Novoselov, M. I. Katsnelson, F. Schedin, D. C. Elias, J. A. Jaszczak, A. K. Geim, Giant intrinsic carrier mobilities in graphene and its bilayer, Phys. Rev. Lett. 100 (2008) 016602.

[12] A. A. Balandin, S. Ghosh, W. Z. Bao, I. Calizo, D. Teweldebrhan, F. Miao, C. N. Lau, Superior thermal conductivity of single-layer graphene, Nano Lett. 8 (2008) 902- 907.

[13] A. Peigney, Ch. Laurent, E. Flahaut, R.R. Bacsa, A. Rousset, Specific surface area of carbon nanotubes and bundles of carbon nanotubes, Carbon 39 (2001) 507–514.

[14] R. R. Nair, P. Blake, A. N. Grigorenko, K. S. Novoselov, T. J. Booth, T. Stauber, N. M. R. Peres, A. K. Geim, Fine structure constant defines visual transparency of graphene, Science 320 (2008) 1308.

[15] B. Partoens, and F. M. Peeters, From graphene to graphite: Electronic structure around the K point, Phys. Rev. B 74 (2006) 075404.

[16] S. V. Morozov, K. S. Novoselov, F. Schedin, D. Jiang, A. A. Firsov, and A. K. Geim, Two-dimensional electron and hole gases at the surface of graphite, Phys. Rev. B 72 (2005) 201401.

[17] E. McCann, Asymmetry gap in the electronic band structure of bilayer graphene, Phys. Rev. B 74 (2006) 161403(R).

[18] A. H. Castro Neto, F. Guinea, N. M. R. Peres, K. S. Novoselov and A. K. Geim, The electronic properties of graphene, Rev. of Modern Phys 81 (2009) 109-162.

[19] A. S. Mayorov, R. V. Gorbachev, S. V. Morozov, L. Britnell, R. Jalil, L. A. Ponomarenko, P. Blake, K. S. Novoselov, K. Watanabe, T. Taniguchi, A. K. Geim, Micrometer-scale ballistic transport in encapsulated graphene at room temperature, Nano Lett. 11 (2011) 2396-2399.

[20] I. Khrapach, F. Withers, T. H. Bointon, D. K. Polyushkin, W. L. Barnes, S. Russo, M. F. Craciun, Novel highly conductive and transparent graphene-based conductors, Adv. Mater. 24(2012) 2844-2849.

[21] G. Deligeorgis, M. Dragoman, D. Neculoiu, D. Dragoman, G. Konstantinidis, A. Cismaru, R. Plana, Microwave propagation in graphene, Appl. Phys. Lett. 95 (2009) 073107.

[22] M. Dragoman, D. Neculoiu, A. Cismaru, A. A. Muller, G. Deligeorgis, G. Konstantinidis, D. Dragoman, R. Plana, Coplanar waveguide on graphene in the range 40 MHz–110 GHz, Appl. Phys. Lett. 99 (2011) 033112.

[23] M. Dragoman, D. Neculoiu, D. Dragoman, G. Deligeorgi, G. Konstantinidis, A. Cismaru, F. Coccetti, R. Plana, Graphene for microwaves, IEEE Microwave Magazine 11 (2010) 81-86.

[24] J. H. Chen, C. Jang, S. Xiao, M. Ishigami, M. S. Fuhrer, Intrinsic and extrinsic performance limits of graphene devices on SiO_2, Nature Nanotechnol 3 (2008) 206 -209.

[25] Y. M. Lin, C. Dimitrakopoulos, K. A. Jenkins, D. B. Farmer, H. Y. Chiu, A. Grill, P. Avouris, 100-GHz transistors from wafer-scale epitaxial graphene, Science 327 (2010) 662.

[26] L. Liao, Y. C. Lin, M. Bao, R. Cheng, J. Bai, Y. Liu, Y. Qu, K. L. Wang, Y. Huang, X. Duan, High-speed graphene transistors with a self-aligned nanowire gate, Nature 467(2010) 305 -308.

[27] I. Llatser, C. Kremers, A. Cabellos-Aparicio, J. M. Jornet, E. Alarco´n, D. N. Chigrin, Graphene-based nano-patch antenna for terahertz radiation, Photonics and Nanostructures- Fundamentals and Applications 10 (2012) 353-358.

[28] J. S. Gomez-Diaz, J. Perruisseau-Carrier, Microwave to THz properties of graphene and potential antenna applications, in Proc. International Symposium On Antennas and Propagation (Isap2012), Nagoya, Japan (2012) 239 -242.

[29] M. Dragoman, A. A. Muller, D. Dragoman, F. Coccetti, R. Plana, Terahertz antenna based on graphene, J. Appl. Phy. 107(2010) 104313.

[30] L. Pierantoni, D. Mencarelli, M. Bozzi, R. Moro, S. Moscato, L. Perregrini, F. Micciulla, A. Cataldo, S. Bellucci, IEEE Trans. Micro. Theo. Techni. 6 (2015) 2491 -2497.

[31] S. De Wolf, A. Descoeudres, Z. C. Holman and C. Ballif, High-efficiency silicon heterojunction solar cells: A review, Green 2 (2012) 7–24.

[32] Y. Lin, X. Li, D. Xie, T. Feng, Y. Chen, R. Song, H. Tian, T. Ren, M. Zhong, K. Wang, and H. Zhuet, Graphene/semiconductor heterojunction solar cells with modulated antireflection and graphene work function, Energy Environ. Sci. 6 (2013) 108–115.

[33] X. Li, H. Zhu, K. Wang, A. Cao, J. Wei, Z. Li, Y. Jia, Z. Li, X. Li, D. Wu, Graphene-   on-silicon Schottky junction solar cells, Adv. Mater. 22 (2010) 2743-2748.

[34] W. Cai, Y. Zhu, X. Li, R. D. Piner, and R. S. Ruoff, Large area few-layer graphene/graphite as a transparent conducting electrodes, App. Phy. Lett. 95 (2009) 123115.

[35] X. Li, D. Xie, H. Park, M. Zhu, T.H. Zeng, K. Wang, J. Wei, D. Wu, J. Kong, H. Zhu, Ion doping of graphene for high-efficiency heterojunction solar cells, Nanoscale 5 (2013) 1945-1948.

[36] H.-J. Shin, W. M. Choi, D. Choi, G. H. Han, S.-M. Yoon, H.-K. Park, S.-W. Kim, Y. W. Jin, S. Y. Lee, J. M. Kim, J.-Y. Choi, and Y. H. Lee, Control of electronic structure of graphene by various dopants and their effects on a nanogenerator, J. Am. Chem. Soc. 132 (2010) 15603–15609.

[37] S. Bae, H. Kim, Y. Lee, X. Xu, J.S. Park, Y. Zheng, J. Balakrishnan, T. Lei, H.R. Kim, Y.I. Song, Y.J. Kim, K.S. Kim, B. Ozyilmaz, J.H. Ahn, B.H. Hong,

S. Iijima, Roll-to-roll production of 30-inch graphene films for transparent electrodes, Nat. Nanotech 5 (2010) 574-578.

[38] X. Meng, S. Tongay, J. Kang, Z. Chen, F. Wu, S.S. Li, J.B. Xia, J. Li, J. Wu, Stable p and n-type doping of few-layer graphene/graphite, Carbon 57 (2013) 507-514.

[39] I.-Y. Lee, H.-Y. Park, J.-H. Park, J. Lee, W.-S. Jung, H.-Y. Yu, S.-W. K., G.-H. Kim, J.-H. Park, Hydrazine-based n-type doping process to modulate Dirac point of graphene and its application to complementary inverter, Organic Electronics 14 (2013) 1586–1590.

[40] X. Shi, G. Dong, M. Fang, F. Wang, H. Lin, W.-C. Yen, K. S. Chan, Y.-L. Chueh, and J. C. Ho, Selective n-type doping in graphene via the aluminium nanoparticle decoration approach, J. Mater. Chem. C 2 (2014) 5417 - 5421.

[41] I. Gierz, C. Riedl, U. Starke, C. R. Ast, and K. Kern, Atomic hole doping of graphene, Nano Lett. 8 (2008) 4603-4607.

[42] T. Cui, R. Lv, Z.H. Huang, S. Chen, Z. Zhang, X. Gan, Y. Jia, X. Li, K. Wang, D. Wu, F. Kang, Enhanced efficiency of graphene/silicon heterojunction   solar cells by molecular doping, J. Mater. Chem. A 1 (2013) 5736-5740.

[43] B. W. Mwakikunga and K. T. Hillie, Graphene Synthesis, Catalysis with Transition Metals and Their Interactions by Laser Photolysis, 5, in: J. R. Gong (Ed.), Graphene − Synthesis, Characterization, Properties and Applications, Intech, 2011, pp. 59-78.

[44] H. Kim, A. A. Abdala and C. W. Macosko, Graphene/Polymer nanocomposite, Macromolecules 43 (2010) 6515–6530.

[45] Ali Mohsin, Thesis "Graphene synthesis and characterization on copper", University of Iowa, 2012. http://ir.uiowa.edu/etd/3354.

[46] Y. Zhang, J. P. Small, W. V. Pontius, P. Kim, Fabrication and electric-field-dependent transport measurements of mesoscopic graphite devices, Appl. Phys. Lett. 86 (2005) 073104.

[47] P. Blake, E. W. Hill, A. H. Castro Neto, K. S. Novoselov, D. Jiang, R. Yang, T. J. Booth, A. K. Geim, Making graphene visible, Appl. Phys. Lett. 91 (2007) 63124.

[48] I. Forbeaux, J. Themlin, J. Debever, High-temperature graphitization of the 6H-SiC (0001) face, Surf. Sci. 442 (1999) 9-18.

[49] P. Sutter, Epitaxial graphene: How silicon leaves the scene, Nat. Mater. 8 (2009) 171-172.

[50] J. Hass, R. Feng, T. Li, X. Li, Z. Zong, W. A. de Heer, P. N. First, E.H. Conrad, C. A. Jeffrey, C. Berger, Highly ordered graphene for two dimensional electronics, Appl.Phys. Lett. 89 (2006) 143106.

[51] K. V. Emtsev, A. Bostwick, K. Horn, J. Jobst, G. L. Kellogg, L. Ley, J. L. McChesney, T. Ohta, S. A. Reshanov, J. Röhrl, E. Rotenberg, A. K. Schmid, D. Waldmann, H. B. Weber, T. Seyller, Towards wafer-size graphene layers by atmospheric pressure graphitization of silicon carbide, Nat. Mater. 8 (2009) 203-207.

[52] S. Park, and R. S. Ruoff, Chemical methods for the production of graphenes Nat. Nanotech. 4 (2009) 217-224.

[53] A. Lerf, H. He, M. Forster, and J. Klinowski, Structure of graphite oxide revisited, J. Phys. Chem. B 5647 (1998) 4477-4482.

[54] H. He, T. Riedl, A. Lerf, Solid-state NMR studies of the structure of graphite oxide, J. Phys. Chem. B 1996, 3654, 19954-19958.

[55] X. An, T. Simmons, R. Shah, C. Wolfe, K. M. Lewis, M. Washington, S. K. Nayak, S. Talapatra, S. Kar, Stable aqueous dispersions of noncovalently functionalized graphene from graphite and their multifunctional high-performance applications, Nano letters 10 (2010) 4295-301.

[56] S. Bose, T. Kuila, A. K. Mishra, N. H. Kim, J. H. Lee, Preparation of non-covalently functionalized graphene using 9-anthracene carboxylic acid, Nanotech. 22 (2011) 405603.

[57] L. Jiao, L. Zhang, X. Wang, G. Diankov, H. Dai, Narrow graphene nanoribbons from carbon nanotubes, Nature 458 (2009) 877-80.

[58] C. Soldano, A. Mahmood, E. Dujardin, Production, properties and potential of graphene, Carbon 48 (2010) 2127-2150.

[59] C. Mattevi, H. Kim, M. Chhowalla, A review of chemical vapour deposition of graphene on copper, J. Mat. Chem. 21 (2011) 3324.

[60] Z. Sun, Z. Yan, J. Yao, E. Beitler, Y. Zhu, J. M. Tour, Growth of graphene from solid carbon sources, Nature 468 (2010) 549-552.

[61] H. Ji, Y. Hao, Y. Ren, M. Charlton, W. H. Lee, Q. Wu, H. Li, Y. Zhu, Y. Wu, R. Piner, R. S. Ruoff, Graphene growth using a solid carbon feedstock and hydrogen, ACS nano 5 (2011) 7656-7661.

[62] S.-J. Byun, H. Lim, G.-Y. Shin, T.-H. Han, S. H. Oh, J.-H. Ahn, H. C. Choi, T.-W.Lee, Graphenes converted from polymers, J. Phys. Chem. Lett. 2 (2011) 493-497.

[63] Z. Yan, Z. Peng, Z. Sun, J. Yao, Y. Zhu, Z. Liu, P. M. Ajayan, J. M. Tour, Growth of bilayer graphene on insulating substrates, ACS nano 5 (2011) 8187-8192.

[64] L. M. A. Perdigao, S. N. Sabki, J. M. Garfitt, P. Capiod, P. H. Beton, Graphene formation by decomposition of C_{60}, J. Phys. Chem. C 115 (2011) 7472-7476.

[65] H. J. Shin, W. M. Choi, S.-M. Yoon, G. H. Han, Y. S. Woo, E. S. Kim, S. J. Chae, X.-S. Li, A. Benayad, D. D. Loc, F. Gunes, Y. H. Lee, J.-Y. Choi, Transfer-free growth of few-layer graphene by Self-Assembled Monolayers, Adv. Mater. 23 (2011) 4392-7.

Chapter 2

Literature review

2.1 Introduction

In this chapter, literature review on graphene properties, graphene based microwave passive components and status of graphene/silicon heterojunction solar cells is presented. First, few reports on dielectric and optical properties of graphene determined using coplanar waveguide (CPW) structure and other methods are discussed. Theoretical and experimental performances of few passive components fabricated on graphene are then described. Since graphene is actively used in silicon heterojunction solar cells, progress in such solar cell with reported efficiency is summarized. At the end, the scope of this research work is presented for the application of CVD grown graphene.

2.2 Graphene properties in the microwave range

For optimum utilization of graphene in microwave applications, its electromagnetic (EM) properties need to be studied at the microwave range. Previously, Wu Y *et al.* (2012) **[1]** investigated the microwave transmission properties of graphene using fixture based on coplanar waveguide (CPW) loaded with glass and graphene/glass (graphene transferred on glass substrates) and was characterized in 0.5 - 6 GHz **[1]**.They found that the permittivity of graphene has frequency-dependent behaviour below 4 GHz and a conductivity of graphene is calculated to about 1.4×10^5 S/m by fitting.The effective permittivity of graphene/glass was found between3 to 6. Furthermore, it was reported that the real and imaginary part of complex permittivity of single layer

graphene is inthe order of 10^6 and 10^4 in 0.5- 6 GHz [1]. In another report, a coupled line graphene CPW and CPW reference which has identical dimension but without graphene under the metallic electrode were studied and effective permittivity was found between 2 to 16 in 5- 40 GHz range [2]. In order to study the effect of applied DC voltage on microwave properties of graphene, a CPW structure was made on graphene/SiO_2/Si substrate and characterized in the frequency range of 40 MHz-110 GHz [3]. In this work, they reported that reflection parameter (S_{11}) is independent of voltage range (- 4 to + 4 V), whereas the transmission coefficient (S_{21}) varies with bias voltage which was applied between the centre and ground electrodes of CPW. This CPW was modelled as a parallel RC circuit and it was observed that S_{21} slightly changed with appliedbias where aslarge variation was observed in R and C. R has maximum value (~ 72 Ω) at 0 V and then reduced to ~ 50 Ω after applying biasing in the range of -2 V and + 2 V. In 2009, this group [4], reported that S-parameters of CPW on graphene exhibits the characteristic of passive device for which $|S_{11}| = |S_{22}|, |S_{12}| = |S_{21}|$ and graphene resistance can be tuned up to 50 Ω.This becomes possible due to quantization of conductivity in 2D nature of graphene.

Skulason *et al.*[5] have studied microwave scattering parameter of large area multilayer graphene by making electrically shorted CPW structure with a trace gap of 38 μm, and the same CPW structure with graphene in the gap. They found that resistive impedance of graphene increases S_{12}, whereas S_{11} decreased [5]. They have further analyzed results by using the equivalent lossy transmission line model and concluded that due to insignificant skin-effect and negligible kinetic inductance, single layer graphene might be an ideal broadband resistive medium in the integrated microwave circuits. Wu *et al.* (2014) [6] have assessed the suitability of multilayer graphene for

microwave applications by carrying out the microwave absorption and radiation measurements. Through the microwave cavity measurements, it has been revealed that as conductivity of multilayer stacked graphene increased resonance peak as well as quality factor of the cavityget reduced. Due to inherently absorptive behavior of the ultra-thin resistive graphene film material, it can be used as optically transparent microwave absorbers. They found that making higher the number of graphene layers at the lossy dielectric region increases the absorption and lead to reduce the radiation amplitude. They further concluded that the reductionin sheet resistance by doping or electrical biasing in few-layer graphene patches paves ways to use them as optically transparent and mechanically flexible microwave antennas.

Furthermore, the complex refractive index, which consists of refractive index (n) and extinction coefficient (κ) were determined for CVD graphene using non-destructive method such as broadband spectrophotometery [7] and spectroscopic ellipsometry [8].In these reports, n and κ were found in the range of ~2.7 – 3 and ~1.4 – 1.8 in $300 - 1000$ nm wavelengths, respectively. Recently, occurrence of strong optical anomalous dispersion in graphene has been reported by determining the complex refractive index ñ ≈ 2.98 - 1.44î for single layer graphene (SLG) and around ñ ≈ 2.7 - 1.45î for bilayer graphene (BLG) at 633 nm using Picometrology [9]. It was reported that anomalous dispersion is likely occurred due to strongly modified quantum level structure of SLG [8] as well as to interparticle interaction, impurities, lattice deformation in graphene with small concentration [10]. Alisultanova *et al.* (2013) [10] noted an appearance of anomalous dispersion regions due to deformation of the graphene lattice. They have proposed a method for describing graphene in an anomalous dispersion region in terms of deviation from the linear dispersion. They further suggested that the explicit

dependence of the parameter α on factors leading to such a deviation can be obtained from the microscopic theory of fractional power deviation of the energy spectrum of graphene. The estimation of effective mass of electron only provides the information about the electron-electron and electron-phonon interactions. Till date, only effective electron mass (m_e^*) was reported to be $0.012m_0$[11] and $0.041m_0$[12] in SLG and BLG, respectively, where free electron mass $m_0 = 9.107 \times 10^{-31}$ kg. Tiras *et al.* (2013) [11] have determined the two dimensional carrier density (N_{2D}) and effective mass (m*) for electrons in the monolayer graphene from the Shubnikov de Haas (SdH) oscillations and the temperature dependencies of the SdH amplitude, respectively. In the acoustic phonon regime, they investigated energy-loss rates of 2D electrons in a monolayer graphene. They found that acoustic phonon emission via piezoelectric and deformation-potential scattering led to the energy relaxation of electrons. Zou *et al.* (2011) [12] reported the measurement of the effective mass *m** in bilayer graphene with different electron and hole densities. Their results have demonstrated that the interlayer hopping parameter v_4 can be accurately determined in the tight-binding description of the band structure from a pronounced electron-hole asymmetry. Compared with single-particle predictions, the suppressed effective mass is obtained due to interaction-induced band renormalization.

Taking account of wave-particle duality and semi-classical definition of the particle momentum, Ariel (2012) reported that particle velocity is associated with the group velocity (v_g) of wave-packet [13] where v_g is approximated by $v_g = \frac{\partial E}{\partial p}$, $p = \hbar k$ is the momentum, *E* is energy and function of *p* and *k* is the wave vector ($k = n\omega/c$). In 2D graphene, due to non-parabolic *E-k* relationship in the vicinity of the Dirac points, energy dispersion relationship is $E = v_f p$ and leads $v_g \approx v_f$ where v_f is the Fermi velocity

of the particle.Therefore, we can presume that in 2D graphene $v_g \approx v_f \approx v_p$ is exhibited and photons can propagate with the velocity same as v_g in graphene and have effective mass m_{op}^*[13, 14].

2.3 Graphene based passive microwave devices

Extraordinary frequency independent properties of graphene led to extensive research in the fabrication of graphene based active devices upto frequency $\approx$100 GHz [15-17]. Few reports are available on graphene based passive microwave devices. In 2012 [18], a graphene-based nano patch antenna on Si/SiO$_2$ substratewas proposed and scattering of terahertz radiation was numerically analyzed. It was proposed that a resonant behaviour of patch antenna in terahertz range might be due to the propagation of the surface-plasmon polariton waves in graphene. In further advance, graphene based patch antenna was modelled by using the commercial high frequency electromagnetic field simulation solution (HFSS) software [19] and resonant frequency was found to be dependent on the chemical potential and limited tuneability observed. Radiation efficiency was also improved up to 90 % at microwaves and 60 % at THz. This might be due to behaviour of graphene at THz that dominated by large surface reactance not by losses. In another report, a single THz dipole antenna based on graphene transferred over SiO$_2$/Si substrate was configured using gold coating [20] and gain of ~2.72 dBi at 1.05 GHz was observed. After optimizing dipole antenna design and arranged in 4 × 4 identical dipoles gain was increased to 13.9 dBi. Pierantoni et.al have designed and fabricated graphene-based tuneable microstrip attenuator, operated at 1-20 GHz [21, 22] and insertion loss up to 5.5 dB was reported by applying DC bias voltage in the range 0 to 5.5 V and frequency in range of 1 to 20 GHz. In other report, graphene CPW with a

fork-like central conductor was proposed as phase-shifter and it was observed that at 65 GHz, the phase shift changes with 22° when DC voltage was applied in the range of 0 V to 4 V. These applications of graphene encouraged the future scope and improvement for other passive microwave devices like interconnect, substrate material, phase shifter etc.

2.4 Graphene as a TCE in silicon heterojunction solar cells

In recent reports, carrier mobility in graphene is approached to 10^5 cm^2/Vs at room temperature, which is close to theoretical estimated value of $>2 \times 10^5$ cm^2/Vs [23]. Recently, in chemical doped few layer graphene (FLG) sheet resistance as low as 8.8 Ω/square along with sheet carrier density as high as 8.9×10^{14} cm^2 with mean free path large as ~ 0.6 mm and 84 % optical transparency was reported [24]. Such extraordinary electronic and optical properties have stimulated research to explore the application of multilayer graphene as a transparent conducting electrode in silicon heterojunction solar cells. In these cells, Schottky junction is formed at the graphene/silicon interface and a built-in electric field developed. This built-in electric field could be enhanced by tuning the work function of either multilayer graphene or silicon. It has been reported theoretically and experimentally [25-26] that chemical doping graphene with HNO$_3$, FeCl$_3$ and AuCl$_3$ makes graphene strongly p-type and its work function can be tuned in the range of 3.5 eV-5.1 eV. Lin *et al.* in 2012 [27] modelled a Gr/Si heterojunction as a circuit consisting of a constant current source, a Schottky diode, a series resistance, and a parallel resistance. Maximum conversion efficiency of $\sim$11% was achieved after optimizing the layer number, work function, and antireflection coating whereas the fabricated cells with these optimized values have shown efficiency only up to 5.5 %

only. In 2013, Li *et al.*[28] reported that if multi layer graphene was chemically doped with $SOCl_2$ and HNO_3 then conversion efficiency enhanced from 5.52 % to 8.94 % and 9.27 %, respectively.They have discussed the impact of p-type chemical doping onthe performance of graphene films for solar energy conversion. They reported that the chlorine and nitrate anions made contact with the surface of the graphene film for charge separation and easier transport. They found that nitrate ions are more effective for chemical doping of graphene films compared to chlorine to decrease of R_s and increase of V_{oc} and FF and conductivity. Such chemical treatment has proved to a simple and practical method to improve the work function of graphene for optimization of solar cells.

As described by Meng *et al.*[29] that intercalation of $NbCl_5$ and ZnMg in few layer graphene/graphite flake makes it effective p- and n-type, respectively. In this intercalation process, $NbCl_5$ and ZnMg interact with the FLG and increase the disorder via sp^2 to sp^3 hybridization transformation. In further advances, Lin *et al.* in 2013 [26] proposed a simple model for graphene/semiconductor heterojunction solar devices. The performance of device can be improved by using an antireflection technique and by modifying the work function of graphene. They achieved a maximum theoretical efficiency of 9.2 %, whereas fabricated cell with optimized parameters was reported to achieve~ 7.7 % efficiency. It has been reported theoretically and experimentally that by chemical doping work function of p-type graphene increases whereas it decreases for n-type and sheet resistance was reduced with increase of work function [30-31]. Li *et al.* (2010) [30] reported that Schottky junctions formed at graphene/n-Si interface. They have studiedthe photovoltaic responses from taking the J-V data for graphene sheet of different thickness. They observed that more carrier recombination occurred in the

thicker films leads to low J_{SC} and V_{OC} and they have estimateddepletion width to be in range of 0.5 - 0.7 μm, which has to be further increase to improve power conversion efficiency. Miao *et al.* (2012) **[31]** have shown that doping with TFSA overlayers on the graphene/n-Si Schottky junction solar cell junctions and this doping increases power conversion efficiencies of from 1.9 to 8.6%. They found that such doping reduces the graphene's sheet resistance and the built-in potential V_{bi} is found to increase.With molecular doping, increase in the work function as well as conductivity of graphene was achieved which results in higher fill factor by reducing the series resistance of Gr/Si heterojunction cell **[26, 32]**.

Cui *et al.* (2013) **[32]** have developed graphene/Si Schottky junction solar cells by transferring graphene film onto n-Si. They noted initial power conversion efficiency (PCE) of these cells in the range of 1.94–2.66%. Molecular doping with HNO_3, $SOCl_2$, H_2O_2, and HCl has increased the work function and conductivity of the graphene film by reducingsheet resistance R_s and improve the quality of G/Si Schottky junction. After doping, PCEs have increased to 213.1%, 230.0%, 212.2% and 211.6% of their original values. Maximum efficiency is achieved up to 5.95% upon $SOCl_2$ treatment. Feng *et al.* (2012) **[33]** have constructed a graphene/silicon Schottky junction solar cell using a graphene film and a pillar-array patterned silicon substrate. After HNO_3 treatment, this cell has shown enhancement in energy efficiency up to 4.35% from 2.90%. They noticed that an effective p-type HNO_3 doping downshifts the work function of graphene and reduces its resistivity. Ruan *et al.* (2015) **[34]** have developed flexible graphene/silicon heterojunction solar cells by using ultrathin c-Si as substrates. They demonstrated a PCE of 8.42% for a 40 mm-thick c-Si based solar cell after performing surface passivation on Si, inserting a layer of P3HT as an electron blocking layer, and controlling the layer number and doping of graphene. Excellent flexibility and durability

of devices are shown as unchanged performance even with a bending radius of 8 mm. They suggested that without improving the conductivity of the graphene fllm, increasing the device area will lead to device degradation. So by adding a mesh electrode on graphene or using metallic nanowires is better solution to enhance the conductivity of graphene and device area. Shi *et al.* (2013) **[35]** reported monolayer graphene-Si solar cells by applying a colloidal antireflection coating on top of the graphene layer and these cells exhibited efficiencies up to 14.5%. The anti-reflection coating significantly improved a short-circuit current density by 30% and it is found to stable. In general, p-graphene/n-silicon configuration has been mostly studied **[25-35]** and the maximum efficiency of about 9.27 % **[28]** without coating and 14.5 % **[35]** with colloidal anti-reflection coating have been reported, However, n-graphene/p-silicon configuration is less reported **[36-38]**. Mohammed *et al.* (2012) **[38]** reported the synthesis of graphene at large scale and low cost using CVD. They found Schottky junction with rectification behavior formed by graphene coating on n-Si wafer. In their results, the supernatant graphene is found to be the most desirable material for the fabrication of G/n-Si junction with excellent rectifying capability and good photovoltaic conversion efficiency. The rectification behavior is also observed in G/p-Si, but this configuration has shown poor photovoltaics conversion efficiency due to the weak p-type conductivity.Tongay *et al.* (2012) **[39]** have characterized the Schottky barriers formed when graphene made intimate contact with the n-type semiconductors Si, GaAs, GaN and SiC using current-voltage and capacitance-voltage measurements. They found that graphene's Fermi level shifts during the charge transfer across the graphene/semiconductor interface due to a low density of states.

2.5 Scope of the present work

Graphene properties in the microwave frequency are not much explored, therefore in order to have potential application of graphene in microwave passive devices, graphene properties such as complex relative permittivity, refractive index and phase and group velocities along with optical effective mass of photons in graphene need to be studied experimentally. However, few microwave passive components such as patch antenna, microstrip attenuator and phase shifter etc. based on graphene were explored. Hence, experimentally reliable non-destructive method is required to study the properties of CVD-grown graphene in microwave devices. In addition, due to insignificant skin-effect and negligible kinetic inductance, graphene may have properties independent of frequency.

In this work, single layer graphene (SLG) transferred on two substrates, glass and quartz and as-grown bilayer graphene (BLG) on Cu samples were characterized using the multilayer microstrip line technique **[40]**. A de-embedding method was adopted and verified with standard ABCD de-embedding method **[41]** by comparing effective relative permittivity, phase velocity and group velocity in 100 MHz - 10 GHz range.We have investigated occurrence of anomalous dispersion in SLG by phase velocity and group velocity of the multilayer microstrip line. Then, the intrinsic properties like complex relative permittivity and refractive index of SLG and BLG have been obtained by using expressions of conformal mapping **[42-44]** from S-parameter measurements in 10 MHz to 26.5 GHz range. To observe the behaviour of waves in SLG and BLG, phase velocity, group velocity and optical effective mass of photons have been evaluated. The outcome of this study will provide the relationship between the graphene properties and its performance at the microwave frequencies. It will

further pave the way to explore the controllable applications of graphene in the field of high-frequency electronics. As an efficient transparent conducting electrode, graphene was used in silicon heterojunction cells in n/p and p/n configuration and cell parameters were analyzed using AFORS-HET.Independent effect of the layer's parameters on the performance of cell structure and insights behind the cell responses have been discussed in detail.

References

[1] Y. Wu, Y. Xu, Z. Wang, C. Xu, Z. Tang, Y. Chen, and R, Xu, Microwave transmission properties of chemical vapor deposition graphene, Appl. Phy. Lett. 101 (2012) 053110.

[2] M. Dragoman, A. Cismaru, A. Stefanescu, A. Dinescu, D. Dragoman, The electromagnetic properties of graphene in the microwave and millimeterwave spectrum, In Proceedings: The 43rd European Microwave Conference, Nuremberg, Germany, 2013, p.530-532.

[3] M. Dragoman, D. Neculoiu, A. Cismaru, A. A. Muller, G. Deligeorgis, G. Konstantinidis, D. Dragoman, and R.Plana, Coplanar waveguide on graphene in the range 40 MHz–110 GHz, Appl. Phys. Lett. 99 (2013) 033112.

[4] G. Deligeorgis, M. Dragoman, D. Neculoiu, D. Dragoman, G. Konstantinidis, A. Cismaru, R. Plana, Microwave propagation in graphene, Appl. Phys. Lett. 95 (2009) 073107.

[5] H. S. Skulason, H. V. Nguyen, A. Guermoune, V. Sridharan, M. Siaj, C. Caloz, and T. Szkopek, 110 GHz measurement of large-area graphene integrated in low-loss microwave structures, Appl. Phys. Lett. 99 (2011) 153504.

[6] B. Wu, H. M. Tuncer, A. Katsounaros, W. Wu, M. T. Cole, K. Ying, L. Zhang, W. I. Milne, Y. Hao, Microwave absorption and radiation from large-area multilayer CVD graphene, Carbon 77 (2014) 814 -822.

[7] A. Gray, M. Balooch, S. Allegret, S. D. Gendt, and W. E. Wang, Optical detection and characterization of graphene by broadband spectrophotometry, J. Appl. Phys. 104 (2008) 053109.

[8] F. J. Nelson, V. K. Kamineni, T. Zhang, E. S. Comfort, J. U. Lee and A. C. Diebold, Optical properties of large-area polycrystalline chemical vapor deposited graphene by spectroscopic ellipsometry, Appl. Phys. Lett. 97 (2010) 253110.

[9] X. Wang, Y. P. Chen and D. D Nolte, Strong anomalous optical dispersion of graphene: complex refractive index measured by Picometrology, Optics Express 16(26) (2008) 22105.

[10] Z. Z. Alisultanova and R. P. Meilanov, On the theory describing graphene in an anomalous-dispersion region, J. of Surface Investigation. X-ray, Synchrotron and Neutron Techniques 7(1) (2013) 46–50.

[11] E. Tiras, S. Ardali, T. Tiras, E. Arslan, S. Cakmakyapan, O. Kazar, *et al.* Effective mass of electron in monolayer graphene: Electron-phonon interaction, J. Appl. Phys. 113 (2013) 43708.

[12] K. Zou, X. Hong, and J. Zhu, Effective mass of electrons and holes in bilayer graphene: electron-hole asymmetry and electron-electron interaction, Phys. Rev. B 84 (2011) 085408.

[13] V. Ariel, Effective mass and energy-mass relationship, 2012, e-print arXiv:1205.3995.

[14] V. Ariel and A. Natan, Electron effective mass in graphene, 2012, e-print arXiv:1206.6100v2 [physics.gen-ph]

[15] J. H. Chen, C. Jang, S. Xiao, M. Ishigami, M. S. Fuhrer, Intrinsic and extrinsic performance limits of graphene devices on SiO_2, Nature Nanotechnol 3 (2008) 206-209.

[16] Y. M. Lin, C. Dimitrakopoulos, K. A. Jenkins, D. B. Farmer, H. Y. Chiu, A. Grill, P. Avouris, 100-GHz transistors from wafer-scale epitaxial graphene, Science 327 (2010) 662.

[17] L. Liao, Y. C. Lin, M. Bao, R. Cheng, J. Bai, Y. Liu, Y. Qu, K. L. Wang, Y. Huang, X. Duan, High-speed graphene transistors with a self-aligned nanowire gate, Nature 467(2010) 305 -308.

[18] I. Llatser, C. Kremers, A. Cabellos-Aparicio, J. M. Jornet, E. Alarco´n, D. N. Chigrin, Graphene-based nano-patch antenna for terahertz radiation, Photonics and Nanostructures- Fundamentals and Applications 10 (2012) 353-358.

[19] J. S. Gomez-Diaz, J. Perruisseau-Carrier, Microwave to THz properties of graphene and potential antenna applications, in Proc. International Symposium On Antennas and Propagation (Isap2012), Nagoya, Japan (2012) 239 -242.

[20] M. Dragoman, A. A. Muller, D. Dragoman, F. Coccetti, R. Plana, Terahertz antenna based on graphene, J. Appl. Phy. 107(2010) 104313.

[21] L. Pierantoni, D. Mencarelli, M. Bozzi, R. Moro, S. Moscato, and S. Bellucci, Graphene-based electronically tuneable microstrip attenuator, Nanomater. Nanotechnol. 4(18) (2014) 1-6.

[22] L. Pierantoni, D. Mencarelli, M. Bozzi, R. Moro, S. Moscato, L. Perregrini, F. Micciulla, A. Cataldo, S. Bellucci, IEEE Trans. Micro. Theo. Tech. 6 (2015) 2491 -2497.

[23] A. S. Mayorov, R. V. Gorbachev, S. V. Morozov, L. Britnell, R. Jalil, L. A. Ponomarenko, P. Blake, K. S. Novoselov, K. Watanabe, T. Taniguchi, A. K. Geim, Micrometer-scale ballistic transport in encapsulated graphene at room temperature, Nano Lett. 11 (2011) 2396-2399.

[24] I. Khrapach, F. Withers, T.H. Bointon, D.K. Polyushkin, W.L. Barnes, S. Russo, M.F. Craciun, Novel highly conductive and transparent graphene-based conductors, Adv.Mater. 24 (2012) 2844-2849.

[25] S. Bae, H. Kim, Y. Lee, X. Xu, J.S. Park, Y. Zheng, J. Balakrishnan, T. Lei, H.R. Kim, Y.I. Song, Y.J. Kim, K.S. Kim, B. Ozyilmaz, J.H. Ahn, B.H. Hong, S. Iijima, Roll-to-roll production of 30-inch graphene films for transparent electrodes, Nat. Nanotech 5 (2010) 574-578.

[26] Y. Lin, X. Li, D. Xie, T. Feng, Y. Chen, R. Song, H. Tian, T. Ren, M. Zhong, K. Wang, H. Zhu, Graphene/semiconductor heterojunction solar cells with modulatedantireflection and graphene work function, Energy Environ. Sci. 6 (2013) 108-115.

[27] Y. Lin, D. Xie, Y. Chen, T. Feng, Q. Shao, H. Tian, T. Ren, X. Li, X. Li, L. Fan, K. Wang, D. Wu, H. Zhu, Optimization of graphene/silicon heterojunction solar cells, in Proceedings of Photovoltaic Specialists Conference (PVSC), IEEE, 2012, pp. 002566-002570.

[28] X. Li, D. Xie, H. Park, M. Zhu, T.H. Zeng, K. Wang, J. Wei, D. Wu, J. Kong, H. Zhu, Ion doping of graphene for high-efficiency heterojunction solar cells, Nanoscale 5 (2013) 1945-1948.

[29] X. Meng, S. Tongay, J. Kang, Z. Chen, F. Wu, S.S. Li, J.B. Xia, J. Li, J. Wu, Stable p and n-type doping of few-layer graphene/graphite, Carbon 57 (2013) 507-514.

[30] X. Li, H. Zhu, K. Wang, J. Wei, G. Fan, X. Li, D. Wu, Chemical doping and enhanced solar energy conversion of graphene/silicon junctions, in Proceedings of the Conference on China Technological Development of Renewable Energy Source, 2010, pp. 387-390.

[31] X. Miao, S. Tongay, M.K. Petterson, K. Berke, A.G. Rinzler, B.R. Appleton, A. F. Hebard, High efficiency graphene solar cells by chemical doping, Nano Lett. 12 (2012) 2745-2750.

[32] T. Cui, R. Lv, Z.H. Huang, S. Chen, Z. Zhang, X. Gan, Y. Jia, X. Li, K. Wang, D. Wu, F. Kang, Enhanced efficiency of graphene/silicon heterojunction solar cells by molecular doping, J. Mater. Chem. A 1 (2013) 5736-5740.

[33] T. Feng, D. Xie, Y. Lin, H. Zhao, Y. Chen, H. Tian, T. Ren, X. Li, Z. Li, K. Wang, D. Wu, H. Zhu, Efficiency enhancement of graphene/silicon-pillar-array solar cells by HNO_3 and PEDOT-PSS, Nanoscale 4 (2012) 2130-2133.

[34] K. Ruan, K. Ding, Y. Wang, S. Diao, Z. Shao, X. Zhang, J. Jie, Flexible graphene/silicon heterojunction solar cells, J. Mater. Chem. A 3 (2015) 14370-14377.

[35] E. Shi, H. Li, L. Yang, L. Zhang, Z. Li, P. Li, Y. Shang, S. Wu, X. Li, J. Wei, K. Wang, H. Zhu, D. Wu, Y. Fang, A. Cao, Colloidal antireflection coating improves graphene-silicon solar cells, Nano Lett. 13 (2013) 1776-1781.

[36] K. Batra, S. Nayak, S. K. Behura, and O. Jani, Optimizing performance parameters of chemically-derived graphene/p-Si heterojunction solar cell, J. Nanoscience and Nanotechnology 14 (2014) 1–6.

[37] S. K. Behura, S. Nayak, I. Mukhopadhyay, O. Jani, Junction characteristics of chemically-derived graphene/p-Si heterojunction solar cell, Carbon 67 (2014) 766 –774.

[38] M. Mohammed, Z. Li, J. Cui, T. Chen, Junction investigation of graphene/silicon Schottky diodes, Nanoscale Res. Lett. 7 (2012) 302.

[39] S. Tongay, M. Lemaitre, X. Miao , B. Gila, B.R. Appleton, A.F. Hebard, Rectification at graphene-semiconductor interfaces zero- gap semiconductor-based diodes, Physical Review X, 2 (2012) 011002.

[40] P. Queffelec, P. Gelin, J. Gieraltowski, J. Loaec, A microstrip device for the broadband simultaneous measurement of complex permittivity and permeability, IEEE Trans. Magnetics 30 (1994) 224 - 231.

[41] Agilent De-embedding and Embedding S-parameter Networks Using a Vector Network Analyzer, Application Note 1364-1, Agilent Technologies, Inc., USA 2004, 5980-2784EN.

[42] J. Svaˇcina, Analysis of multilayer microstrip lines by a conformal mapping method, IEEE Trans. Microw. Theory Tech. 40 (4) (1992) 769-772.

[43] J. Svaˇcina, A simple quasistatic determination of basic parameters of multilayer microstrip and coplanar waveguide, IEEE Microw. Guid. Wave Lett. 2 (10) (1992) 385-387.

[44] C. Wan, A. Hoorfar, Improved design equations for multilayer microstrip lines, IEEE Microw. Guid. Wave Lett. 10 (6) (2000) 223-224.

Chapter 3

Experimental Techniques

3.1 Introduction

In this chapter, synthesis and characterization of graphene sample as well as used techniques are discussed in details. SLG transferred on glass and quartz was procured and BLG were grown on Cu foil using hot filament chemical vapor deposition system (HFCVD). The schematic HFCVD system and synthesis conditions are given. In order to confirm the layer number, samples have been first characterized by Raman spectroscopy and then reconfirmed with atomic force microscopy (AFM). Results of these measurements are discussed. For measurements in microwave range, the microstrip line based measurement fixture has been used and then conformal mapping was applied to obtain the intrinsic properties of graphene layers. AFORS-HET software is briefly described, which is used for simulation of graphene/silicon heterojunction solar cell.

3.2 Sample preparation

3.2.1 Single layer graphene (procured)

SLG transferred on glass and quartz substrates of the dimension $1''\times1''$ were procured from Graphene Supermarket manufactured by Graphene Industries, USA. For comparison purpose, blank glass (thickness ≈ 0.7 mm) and quartz (thickness ≈ 1.095 mm) of same dimensions have also been procured. Optical images of samples are shown in **Fig. 3.1**.

(a) Glass substrate   (b) Graphene transferred on glass substrate

(c) Quartz substrate   (d) Graphene transferred on quartz substrate

Fig. 3.1 Single layer graphene samples on glass and quartz substrates

3.2.2 Growth of bilayer graphene using HFCVD

BLG films on Cu foil were grown by using HFCVD System developed at the Nanofabrication laboratory, Department of Applied Physics, Delhi Technological University (DTU), Delhi. In this system, methane (CH_4) was used as a carbon precursor and dissociated into atomic carbon, CH_3 and C_2 radicals which in turn start their gas-

phase reactions. In order to dissociate CH_4, filament temperature   at ~ 2200 °C and substrates temperature at 900 °C was maintained by passing the current of 19 A to filament. Schematic of HFCVD system has been shown in **Fig. 3.2[1, 2, 3]**.
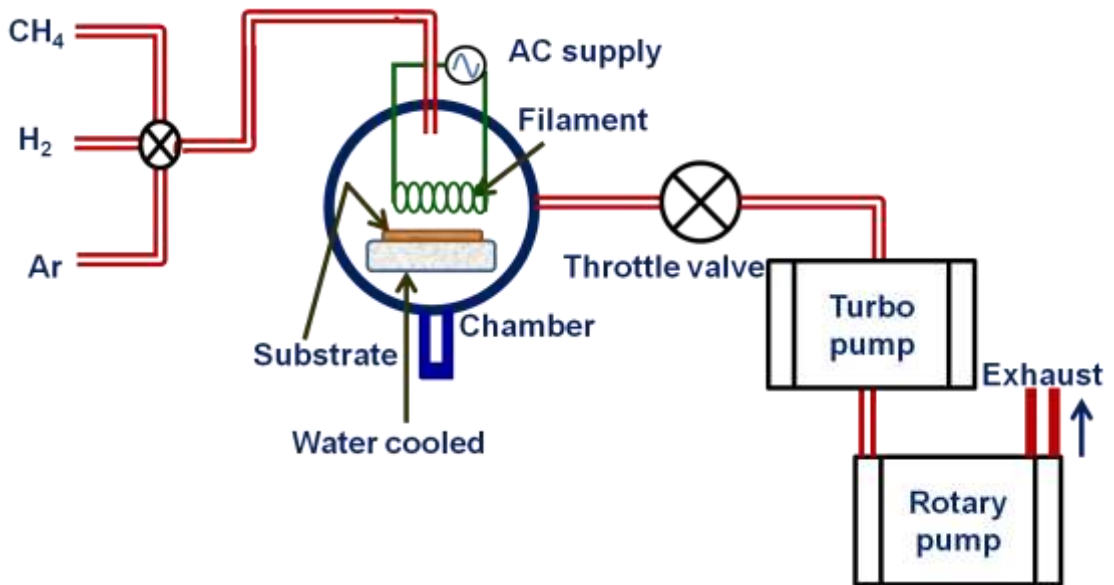
Fig. 3.2 Schematic of HFCVD system for synthesis of graphene.

The HFCVD system was indigenously designed and developed at DTU. This system is consisting a stainless steel chamber coupled with rotary pump to create pressure upto 5×10^{-2} torr. The stainless steel chamber has an inner diameter of 200 mm and has various electrical and gas feed throughs with view ports too. To monitor and control the deposition pressure, computerised throttle valve and gate with Baratron pressure sensor is coupled on the vacuum line. A tungsten wire of 0.1 mm diameter was used as the filament. The filament to substrate distance was kept at 5mm.
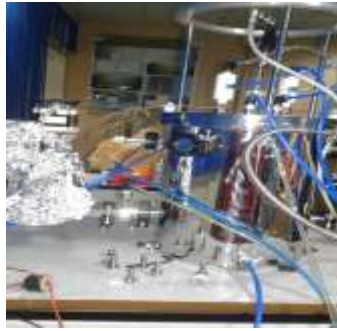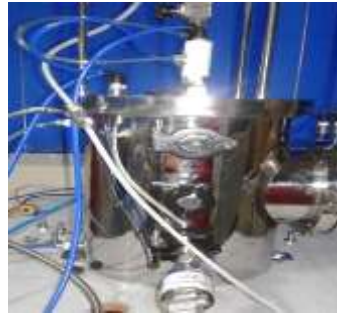
(a) Gate valve   (b) Chamber

(c) Throttle Valve   (d) Rheostat

(e) Chiller unit   (f) Electrodes

(g) Tungsten filament   (h) Filament during synthesis

Fig.3.3 Parts of HFCVD system.

To monitor the substrate temperature and keep it constant, a thermocouple and a temperature controller were placed. Methane (CH_4) and hydrogen (H_2) were used as the source gases to make graphene film on Cu. Optical images of the used HFCVD system are shown in **Fig. 3.3**.

In this CVD process, Cu sheet of thickness 25 μm was cut into size of 1/2″×1/4″ and then used as substrate. Initially, Cu foil was ultrasonicated in acetone for 10 min initially, followed by dipping in acetic acid for 10 min, and then washed with DI water. After drying, Cu foil was loaded into chamber. Schematic representing the process parameters of HFCVD in detail has been shown in **Fig. 3.4**.
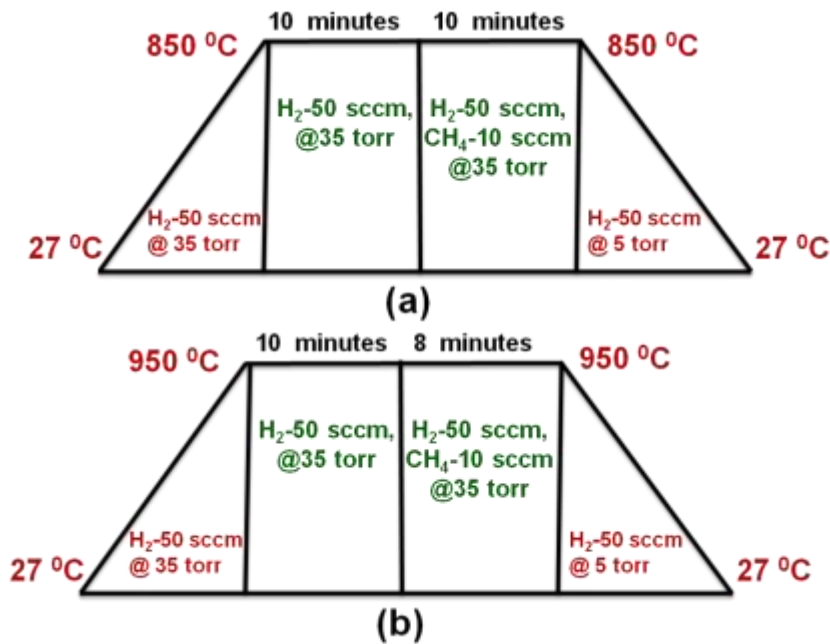
Fig. 3.4 Schematic of the process parameters for (a) BLG/Cu$_1$ and (b) BLG/Cu$_2$.

In this work, we have used graphene films deposited on Cu sheets on two synthesis parameters, bilayer graphene/Cu @ 850° C and bilayer graphene/Cu @ 950° C, these samples are designated as BLG/Cu$_1$ and BLG/Cu$_2$ and illustrated in **Fig.3.5.**

<center>(a)   (b)</center>
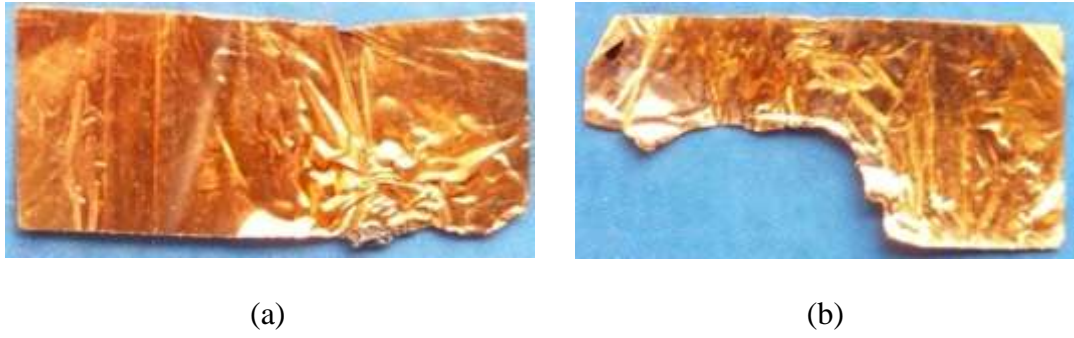
Fig. 3.5 Optical images of as-grown S graphene (a) BLG/Cu$_1$ and (b) BLG/Cu$_2$ of size (1/2" x 1/4").

3.3 Characterization techniques

3.3.1 Raman spectroscopy

Raman analysis is mainly used to confirm the graphene layers as well as to estimate number of graphene layers. In this technique, a monochromatic light source (i.e. laser) is incident on the sample and the scattered light is detected. The scattered light is of same frequency as the frequency of light source, this type of scattering is known as Rayleigh or elastic scattering, in which photon retains its energy [4]. A very small amount of scattered light is shifted from the laser frequency, which happens due to interactions between the incident electromagnetic waves and vibrational energy levels of molecules in the sample. This scattering is called Raman scattering, in which photons lose part of their energy. In Raman spectroscopy, a frequency shift of inelastic scattered light from the sample is measured when a photon from an incident light produces a photon by striking on a molecule of sample. If the outcoming scattered light can be a photon with a lower frequency than the original photon, it is called stokes Raman scattering, whereas if a photon has higher frequency, such scattered light is known as anti-stokes Raman scattering [5]. Typically, the intensity of Raman scattering is 10^6-

<center>45</center>

10^9 times less than the Rayleigh scattered signal **[4]**. A typical set of Raman scattering experimental setup is shown in **Fig. 3.6.**
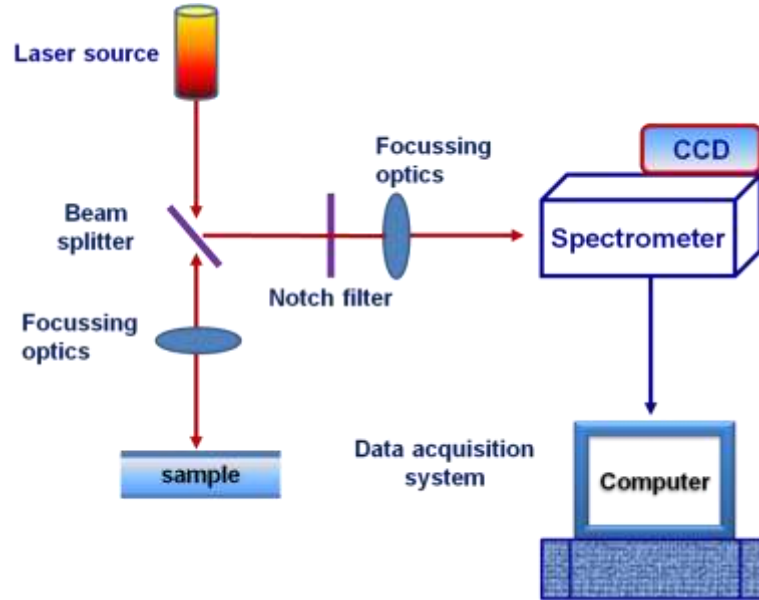
Fig. 3.6 Typical set up of Raman spectroscopy [**6**].

Usually, Raman scattering signal shifted symmetrically in frequency with respect to the frequency (ω_I) of excitation source. The magnitude of this Raman shift (ω) is therefore directly equal to the vibration frequency of the crystal and is given by **[4]**:

$$\omega(\mathrm{cm}^{-1}) = \frac{1}{\lambda_{\mathrm{scatterred}}(\mathrm{cm})} - \frac{1}{\lambda_I(\mathrm{cm})} \tag{3.1}$$

where $\lambda_{\mathrm{scatterred}}$ is the wavelength received from the sample in cm and λ_I is the wavelength of incident light signal in cm.

We have used a high resolution Renishaw inVia Reflex Raman spectrometer, UK (with an excitation source of green laser 514.5 nm and 2.5 mW power) to characterize the graphene samples. Raman spectra of graphene on glass and quartz substrates are shown in **Fig. 3.7** after curve fitting.
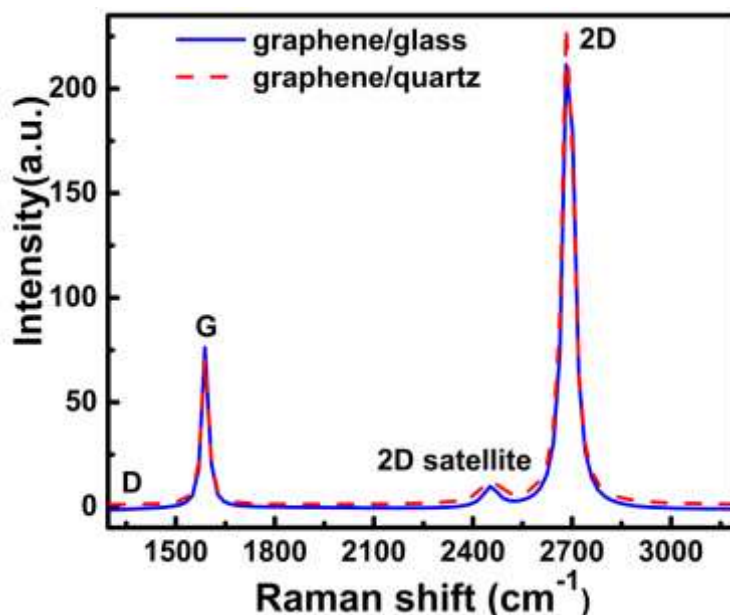
Fig. 3.7 Raman spectra of graphene transferred on glass and quartz substrates.

As shown in **Fig. 3.7**, three sharp peaks were observed and identified as G, 2D satellite and 2D bands. The peak position of these bands are found to be at $\omega_D \sim 1341.83$ cm^{-1}, $\omega_G \sim 1587.12$ cm^{-1}, $\omega_{2Dsatelite} \sim 2452.092$ cm^{-1}, and $\omega_{2D} \sim 2688.67$ cm^{-1} for graphene on glass substrate and for graphene on quartz substrate, we obtained $\omega_D \sim 1341.83$ cm^{-1}, $\omega_G \sim 1587.16$ cm^{-1}, $\omega_{2Dsatelite} \sim 2452.73$ cm^{-1}, and $\omega_{2D} \sim 2688.82$ cm^{-1}. The barely visible D-band is indicating that graphene layers are defect free. The 2D to G-band (I_{2D}/I_G) ratio is found to be ~ 3.69 (on glass) and ~ 4.1 (on quartz), which confirms that a single layer graphene was on both the substrates. The full width half maxima (FWHM) of 2D

band was found to be ~36 cm^{-1}. The thickness of the graphene layer (t) can be obtained by the relation $t = n\Delta d$, where n represents the number of layers and Δd the thickness of single layer graphene ($\Delta d = 0.335$ nm) [6].

Previously, Wang *et al.* (2009) [7]have investigated the phonon dispersions of graphene and graphene layers adopting force-constants model. They found that the phonon dispersions of different number of layers are similiar except for the low wavenumber region due to the very weak interlayer interactions of the graphene layers. They found that layer –number dependant softening of ω_G can used to determine the layer number by using the relation:$\omega_G = 1581.6 + 11/(1 + n^{1.6})$, where n is the number of graphene layer. Their calculated results are reported to provide comprehensive information about vibrational properties of graphene and graphene layers and helps on the interpretation of Raman scattering and infrared spectra. Gupta *et al.*(2006) [8]have studiedultra thin graphitic films (or nGls) obtained by mechanical transfer from an HOPG slab to a SiO$_2$:Si substrate and measured the film thickness of various nGL flakes by averaging AFM z-scans. They found the value $t = 0.355$ nm for the thickness of a graphene layer by fitting the effective film thickness data h vs assigned layer number n as a straight line. They have reported that Raman spectra of nGLs is very sensitive to layer number (n), for n as large as $n=10$ and a simple $1/n$ behavior of the G-band position studied. As the nGL D-band scattering intensity (~1350 cm^{-1}) is observed to strongly decrease as nincreases.

The value of n in the procured graphene samples has been obtained using the following expressions [7-8], respectively,

$$n_1^{1.6} = \frac{11}{(\omega_G - 1581.6)} - 1 \qquad (3.2)$$

and,

$$n_2 = \frac{5.5}{(\omega_G - 1581.6)} \qquad (3.3)$$

Table 3.1 represents the thickness of graphene layer obtained by using Eqs. (3.2) and

(3.3).

Table 3.1 Determined layer thickness of graphene

Substrate	ω_G	t_1(nm) (Eq. (3.2))	t_2(nm) (Eq. (3.3))
Glass	1587.117	0.334	0.334
Quartz	1587.160	0.330	0.331

Similarly, Raman spectra for BLG/Cu$_1$ and BLG/Cu$_2$ are plotted and shown in **Fig. 3.8**.
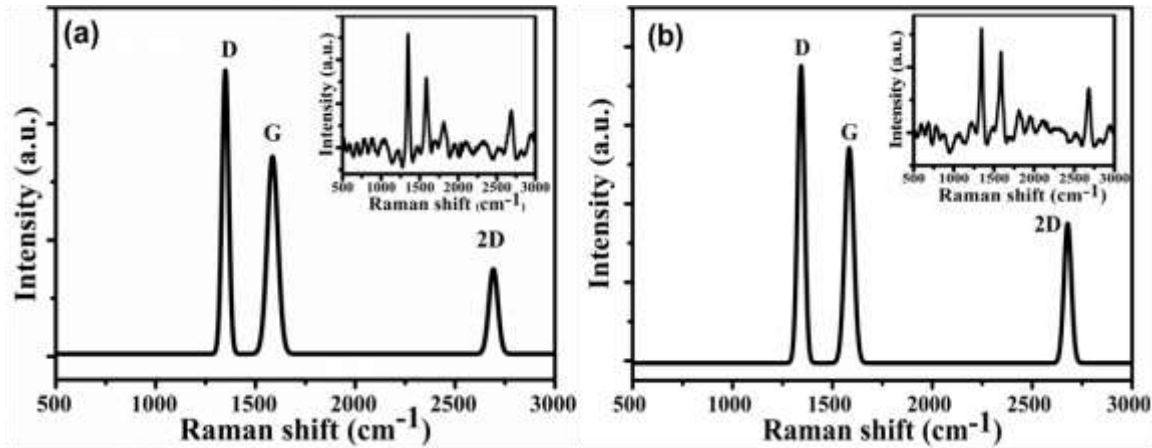
Fig. 3.8 Raman Spectra of as- grown graphene films on Cu sheet for (a) BLG/Cu$_1$ and

(b) BLG/Cu$_2$.

In these spectra, three sharp peaks were indexed as D, G and 2D bands for as-

grown graphene samples after curve fitting. Raw data has been shown in insets. For

BLG/Cu$_1$,the peak positions are found at ω_D ~1342 cm^{-1}, ω_G ~1588 cm^{-1}, and ω_{2D} ~

2713 cm^{-1}, and for BLG/Cu$_2$, these values are at ω_D ~1341cm^{-1}, ω_G ~1586 cm^{-1} and ω_{2D}

~2680 cm^{-1}. The ratio I_{2D}/I_G is calculated as ~0.55 and ~0.64, respectively for BLG/Cu$_1$ and BLG/Cu$_2$, which confirms that a bilayer graphene was on both Cu sheets.

3.3.2 AFM characterization of graphene samples

To characterize the surface property of electrically non-conducting thin film at the micron and submicron scale, AFM is used, in which a sharp tip supported by a cantilever beam is utilized as the measuring probe. In addition, it contains a light source like a laser, a four quadrant photodiode and a scanner unit as shown in **Fig. 3.9**.
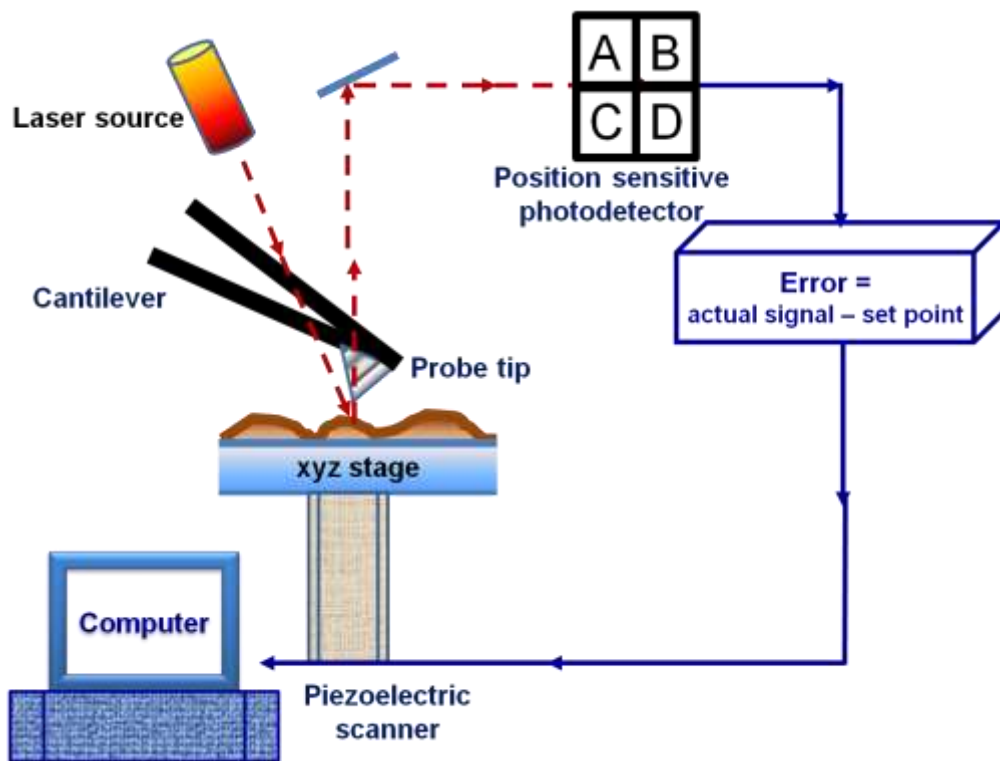
Fig. 3.9 General components of AFM [**10**].

It operates by measuring force between the probe and the surface of the sample like insulators [**9**]. The tip is generally in contact with the surface and any deflection of

the cantilever is monitored by position sensitive photodetector. In a non-contact mode, the cantilever is vibrated close to its resonance frequency. The vibration amplitude or frequency changes according to the tip-sample interaction and this change acts as a feedback in order to maintain a constant distance for tip to the sample surface. This mode is suitable for soft samples like biological or polymer samples.

We have used AFM system of Park System, model XE-100 to study the surface morphology of graphene samples. The AFM topography of graphene/glass and graphene/quartz is shown in **Fig. 3.10(a-b)** and **Fig. 3.10(c-d)**, respectively.
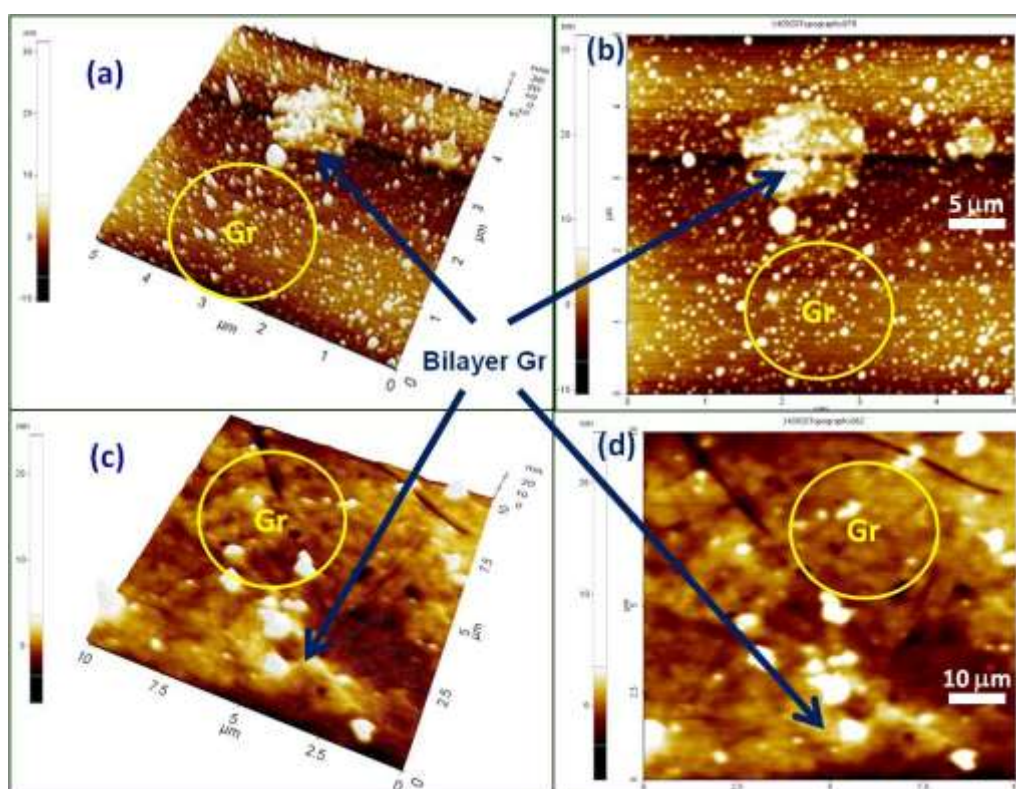
Fig. 3.10 AFM topography (a) 3D view of graphene/glass (5 μm) and (b) graphene/glass (5 μm) (c) 3D view of graphene/quartz (10 μm) and (d) graphene/quartz (10 μm).

Some thicker places represent the presence of bilayer graphene occurred due to covalently bonded oxygen and the displacement of sp^3 hybridized carbon atoms slightly

above the single layer graphene. The graphene crystals are not found to be perfectly flat on glass and quartz, more ripples have been observed on glass than on quartz. These ripples may be due to roughness of the substrates or might be caused during the transfer of the graphene.

3.4 Microwave characterization of graphene samples

3.4.1 Vector network analyzer system

A *vector network analyzer* (VNA) is used to measure the scattering parameters of passive and active networks. It is a two-channel (or four-channel) microwave receiver and designed to process the magnitude and phase of the transmitted and reflected waves from the network. **Fig. 3.11** shows the simplified block diagram of a VNA[11]. In operation, the RF source is usually swept over a specified bandwidth using a switch, which allows the system to be driven from either port 1 or port 2. The incident, reflected, and transmitted RF waves are sampled using a four-port reflectometer. Four dual-conversion channels down convert these RF signals to IF frequencies at 100-kHz, which are detected and then converted to digital form. An internal computer calculates and displays the magnitude and phase of the scattering parameters or other related quantities, like SWR, return loss, group delay, impedance, etc. The network analyzer consists of error-correcting software to improve the accuracy in the measurement. A calibration procedure is used to remove the errors caused by directional coupler mismatch, imperfect directivity, loss, and variations in the frequency response of the analyzer system.
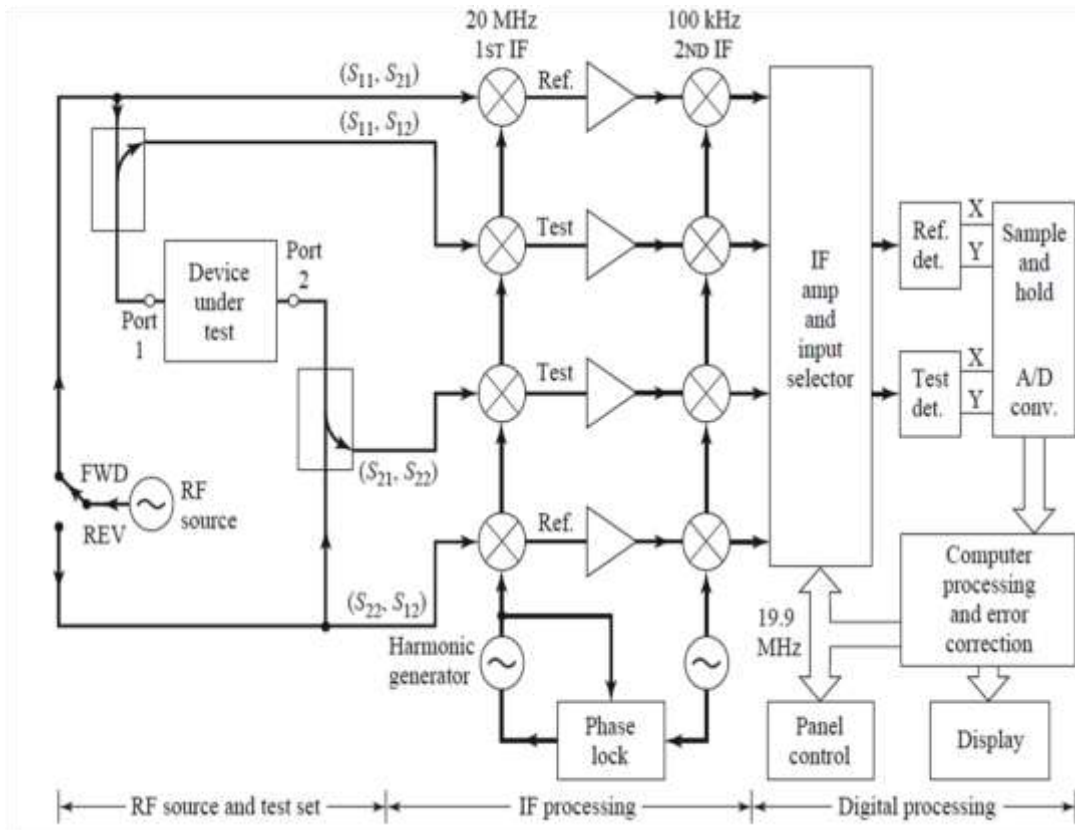
Fig. 3.11 Block diagram of a vector network analyzer **[11]**.

3.4.2 Microstrip line based measurement fixture

To extract the properties of a single layer graphene, we have used the microstrip line based measurement fixture as shown in **Fig. 3.12(a)**, and the top and front view of the fixture are shown in **Figs.3.12(b-c) [10]**. The microstrip line has quasi-transverse electromagnetic (TEM) mode of propagation **[11]**, which is slightly perturbed after loading. As shown in **Fig.3.12(b)**, the fixture is cascaded by three parts in such a way that the central part was loaded (Part 2) whereas other remained parts were unloaded (Part 1 & 3). Part 1 and Part 3 have same physical dimensions. The characteristic impedance and propagation constant of these parts are assigned by Z_n and γ_n, where n is Part number i.e. 1, 2, 3.
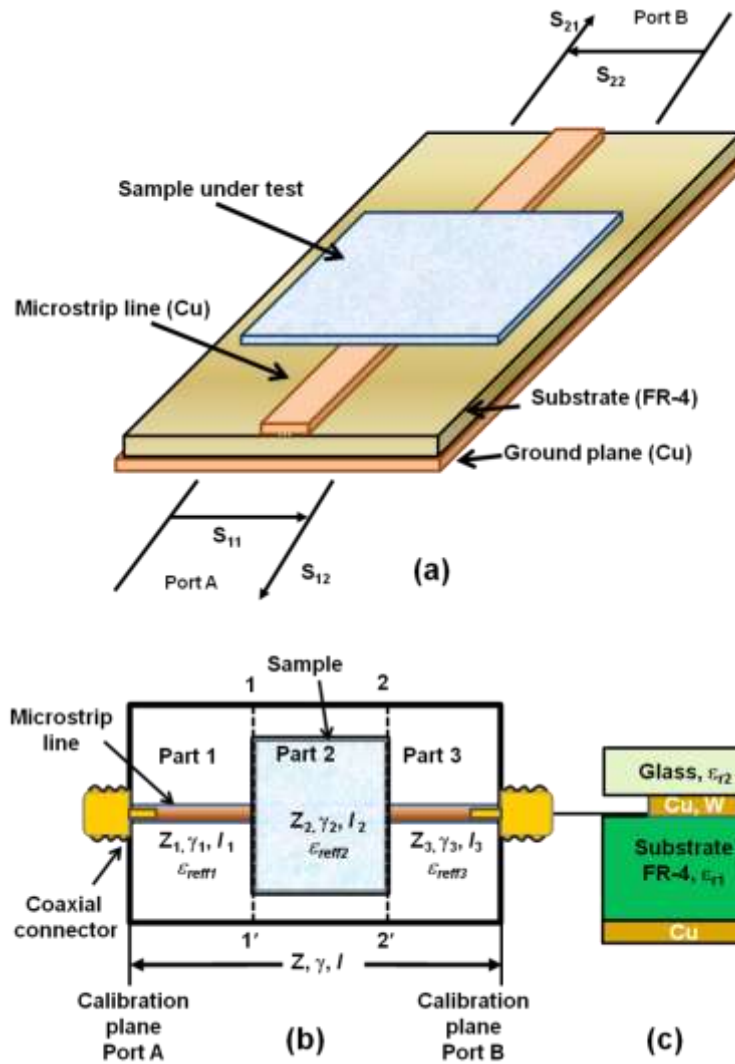
Fig. 3.12(a) Microstrip line loaded with sample, (b) schematic representation of test fixture and (c) front view.

In the measurement fixture, the characteristic impedance and propagation constant in vacuum are denoted by Z_0 (50 Ω) and $\gamma_0 = j2\pi f/c$, respectively, where f is operating frequency in Hz and c is the velocity of light in m/s. Sincethe calibration planes of the vector network analyzer (VNA) are port A and port B, whereas the measurement planes for the sample are 1-1′and 2-2′ as marked. Using de-embedding method, the measurement plane can be shifted from Port A to 1-1′ plane and from Port B to 2-2′ plane, which is detailed in the next sub-section. The microstrip line of width

(*w*) 3.024 mm and length (*l*) 50.8 mm on flame epoxy resin (FR-4) substrate with relative permittivity (ε$_r$) 4.4 and height (*h*) 1.5 mm was fabricated and shown along with text fixture in **Fig. 3.13**.
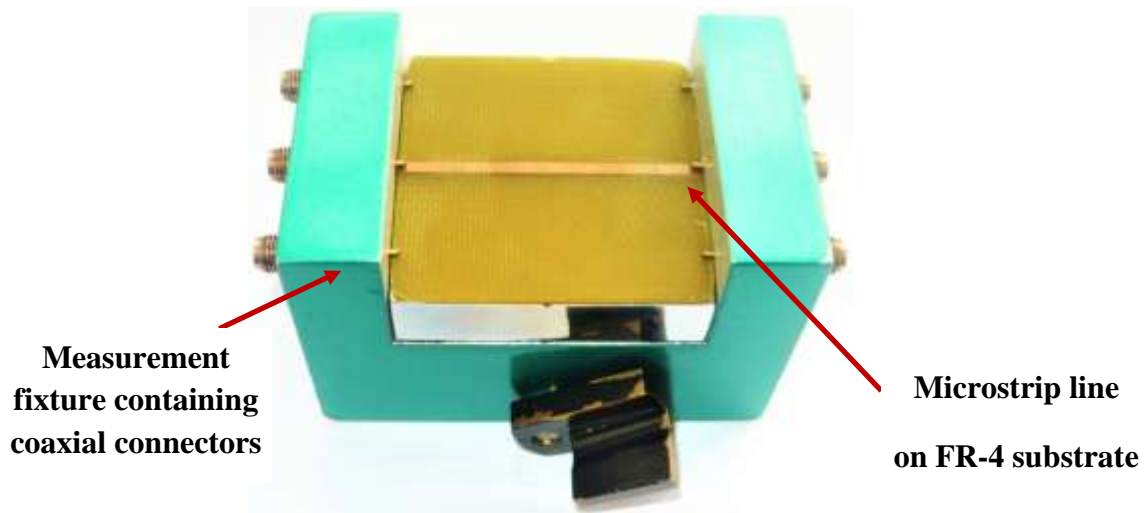
Fig. 3.13 A microstrip line with measurement fixture.

3.4.3 De-embedding method

3.4.3.1 ABCD based method

The transmission (ABCD) parameters are defined in terms of the total voltages (V_i, V_j) and total currents (I_i, I_j)as shown in **Fig. 3.11** and given as in matrix form below[11]:

$$\begin{bmatrix} V_i \\ I_i \end{bmatrix} = \begin{bmatrix} A & B \\ C & D \end{bmatrix} \begin{bmatrix} V_j \\ -I_j \end{bmatrix} \tag{3.4}$$

As [ABCD] parameters relate the parameters of port *i* with voltage and current at other port *j*, such parameters used to obtain response of a cascade of two or more two-port networks. Since the [ABCD] matrix of the cascade connection of two networks is equal

to the product of the two [ABCD] matrices representing individual networks, such feature is used to de-embed the network parameter.

In transmission parameters (ABCD) based de-embedding method **[12-13]**, first S-parameters of microstrip line unloaded and partly loaded over a length (l) were measured individually and then, S-parameters of loaded microstrip line, known as multilayer line (Part 2) can be deduced from the respective ABCD matrix. The first step in this de-embedding is to convert scattering (S)-parameters into transmission line [ABCD] parameters using the following conversion formulas **[11]**:

$$A = \frac{(1+S_{11})(1-S_{22})+S_{12}S_{21}}{2S_{21}} \tag{3.5}$$

$$B = Z_C \frac{(1+S_{11})(1+S_{22})-S_{12}S_{21}}{2S_{21}} \tag{3.6}$$

$$C = \frac{1}{Z_C} \frac{(1-S_{11})(1-S_{22})-S_{12}S_{21}}{2S_{21}} \tag{3.7}$$

$$D = \frac{(1-S_{11})(1+S_{22})+S_{12}S_{21}}{2S_{21}} \tag{3.8}$$

Here, Z_C is the characteristic impedance obtained from the measured S-parameters for unloaded and partly loaded microstrip line and Z_0 is standard 50 Ω.

$$Z_c = \pm Z_o \sqrt{\frac{(1+S_{11})(1+S_{22})-S_{12}S_{21}}{(1-S_{11})(1-S_{22})-S_{12}S_{21}}} \tag{3.9}$$

For cascaded microstrip line, which consists of unloaded and loaded parts as shown in **Fig.3.21(b),** the [ABCD]$_{cascaded}$ matrix is obtained from the S-parameters for unloaded and loaded cases, which can be arranged in following manner:

$$[ABCD]_{cascaded} = [ABCD]_{unloaded} \times [ABCD]_{loaded} \times [ABCD]_{unloaded} \qquad (3.10)$$

For Eq. (3.10), [ABCD] matrix for unloaded case has been modified with the length corresponding to unloaded microstrip line length, by removing the length of sample (i.e. 25.4 mm). This modified [ABCD] matrix is then placed in the following Eq. (3.11) to obtain [ABCD] matrix of loaded microstrip line only.

$$[ABCD]_{loaded} = [ABCD]_{unloaded}^{-1} \times [ABCD]_{Cascaded} \times [ABCD]_{unloaded}^{-1} \qquad (3.11)$$

Then the S-parameters of microstrip line with loading only can be calculated back using the conversion Eqs. (3.12-3.157) from obtained [ABCD]$_{loaded}$ **[11]**.

$$S_{11} = \frac{A + B/Z_0 - CZ_o - D}{A + B/Z_o + CZ_o + D} \qquad (3.12)$$

$$S_{12} = \frac{2(AD - BC)}{A + B/Z_o + CZ_o + D} \qquad (3.13)$$

$$S_{21} = \frac{2}{A + B/Z_o + CZ_o + D} \qquad (3.14)$$

$$S_{22} = \frac{-A + B/Z_o - CZ_o + D}{A + B/Z_o + CZ_o + D} \qquad (3.15)$$

A MATLAB program for this de-embedding is given in **Appendix A**. In this process, since the edges of sample kept on the microstrip line denoted by 1-1′and 2-2′ planes and these planes have been presumed to be symmetrical. Instead, this symmetry assumption leads to an error in the accurate extraction of S-parameters of the multilayer microstrip line i.e. Part 2 **[14]**. To minimize this asymmetry, first the impedances Z_1 and Z_3 are required to deduce and then included with impedance Z_2 to get the modified ABCD matrix as per Eq. (3.11).

3.4.3.2 Propagation constant based method

The drawback of [ABCD] based de-embedding method is the consideration of symmetry which requires further calculation of frequency dependent impedance values to remove asymmetry at the edges, 1-1′and 2-2′ planes. To simplify the process and obtain the S-parameters of loaded microstrip line i.e. Part 2 only, we have proposed a simple de-embedding method, where the propagation constants are directly obtained from the S-parameter measurements taken in both cases, when microstrip line is loaded and unloaded. The complex transmission coefficient as a scattering (S) parameter in terms of propagation constant (γ) and length of microstrip line (l), can be expressed as,

$$S_{21} = |S_{21}|e^{-\gamma l} \tag{3.16}$$

Since, the microstrip line is divided into three parts of length l_1, l_2 and l_3 and propagation constants γ_1, γ_2 and γ_3, respectively. Hence, we can write Eq. (3.16) as **[15]**,

$$S_{21} = |S_{21}|e^{-(\gamma_1 l_1 + \gamma_2 l_2 + \gamma_3 l_3)} \tag{3.17}$$

Thus,

$$\gamma l = \gamma_1 l_1 + \gamma_2 l_2 + \gamma_3 l_3 \tag{3.18}$$

Also in terms of measured S-parameters, γ can be written as:

$$\gamma = \frac{1}{l} \, ln \left[\frac{1+S_{11}-S_{22}-S_{22}S_{11}+S_{21}S_{12}}{2S_{21}} \right] \tag{3.19}$$

To obtain γ_2 of the second part, we simply use the relation

$$\gamma_2 = \frac{(\gamma l - \gamma_1 l_1 - \gamma_3 l_3)}{l_2} \tag{3.20}$$

In the cascaded microstrip line, discontinuity is formed at 1-1′ and 2-2′ planes as shown in **Fig. 3.12(b)**. By considering this as an open discontinuity, it can be modelled as an extra length of line loaded without sample. This extra length of the line 'Δl ' can be estimated by following relation **[16]**,

$$\Delta l = h_S \times 0.412 \frac{\left(\varepsilon_{reff(0)}+0.3\right)\left(\frac{w}{h}+0.262\right)}{\left(\varepsilon_{reff(0)}-0.258\right)\left(\frac{w}{h}+0.813\right)} \tag{3.21}$$

where $\varepsilon_{reff(0)}$ is the static value of effective relative permittivity, h_S is thickness of the sample under test, w and h are the width of microstrip line and height of the substrate, respectively. This length (Δl) is extended in both sides of multilayer microstrip line. To represent this length extension, effective length of Part 1 and Part 3 were further increased by 'Δl' whereas effective length of Part 2 i.e. multilayer microstrip line was decreased by twice of 'Δl'. Therefore, Eq. (3.20) can be re-written as,

$$\gamma_2 = \frac{\gamma l - \gamma_1 (l_1 + \Delta l) - \gamma_3 (l_3 + \Delta l)}{l_2 - 2\Delta l} \tag{3.22}$$

Then, the effective relative permittivity of loaded microstrip line can be obtained from this propagation constant as $\varepsilon_{reff} = (\gamma_2/\gamma_0)^2$ **[17]**. The phase velocity of the waves in a microstrip line is expressed as, $v_p = c/\sqrt{\varepsilon_{reff}}$ in a non-magnetic material ($\mu_r = 1$) and

the group velocity of waves can be obtained from $v_g = c^2/v_p$, where $c = 2.99 \times 10^8$ m/s, the velocity of the light. For the S-parameter measurement of microstrip line in the frequency range 100 MHz to 10 GHz, Anritsu VNA master model MS2083C/2 was used along with an SMA calibration kit.

3.4.4 Conformal mapping technique for multilayer microstrip line

We have studied six samples i.e. glass, quartz, SLG on glass and quartz, two sample of as-grown BLG on Cu foil with different synthesis parameters. The arrangement for keeping these samples is shown in **Fig.3.14**. Loading by SLG/glass or SLG/quartz makes microstrip line structure as a three layer line (**Fig.3.14b**) having three dielectrics, FR-4, glass or quartz and SLG, whereas it becomes a two layer line, when loaded by BLG/Cu (**Fig.3.14c**). To analyze such complex structure, a conformal mapping technique is used to determine accurately frequency dependent parameters such as effective relative permittivity, characteristic impedance and complex propagation constant from DC to high frequency **[18]**. This technique is based on quasi-TEM approximation.
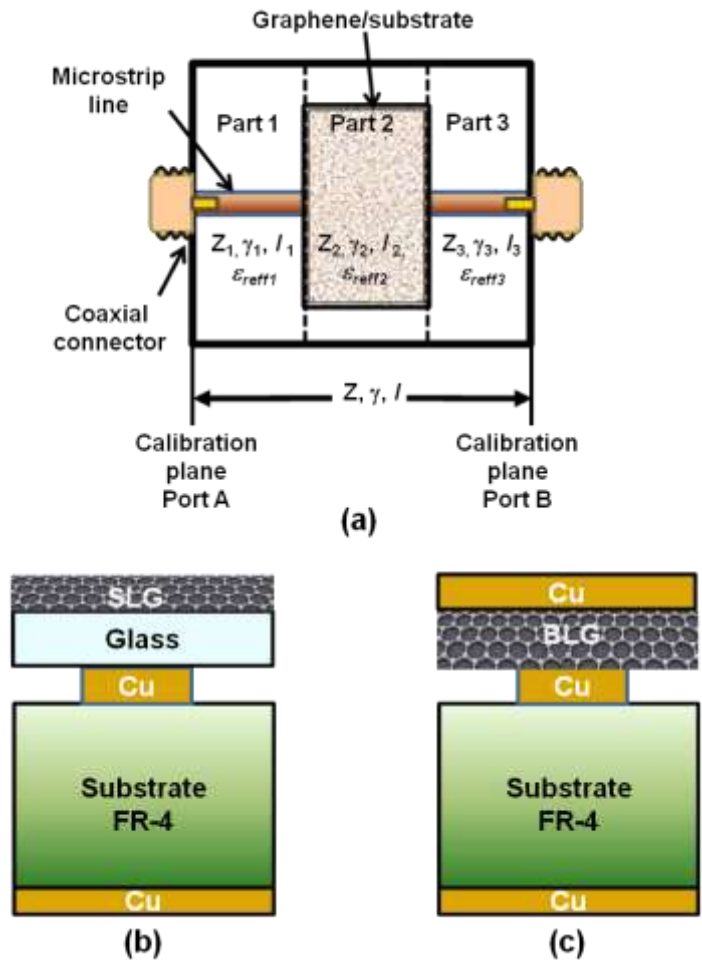
Fig. 3.14 Loading ofmicrostrip line by sample, (a) schematic representation of center part loaded with (b) SLG/glass, and (c) BLG/Cu.

A point in the w-plane can be related to a given point in the z-plane with a function as shown in **Fig. 3.15**. Any point (x, y) in the z–plane provides some point (u,v) in the w-plane, and the function that accomplishes this transformation is called a coordinate transformation from the z-plane to w-plane. If the function consists of complex variables and is analytic, then a complex plane of $z = x + jy$ is transformed into another complex plane of $w = u + jv$, and the infinitesimal shape is preserved during this transformation. This is called a conformal map **[18]**. The use of such conformal

map is to transform a complicated domain into a simple domain through the given function, $w = f(z)$[19].
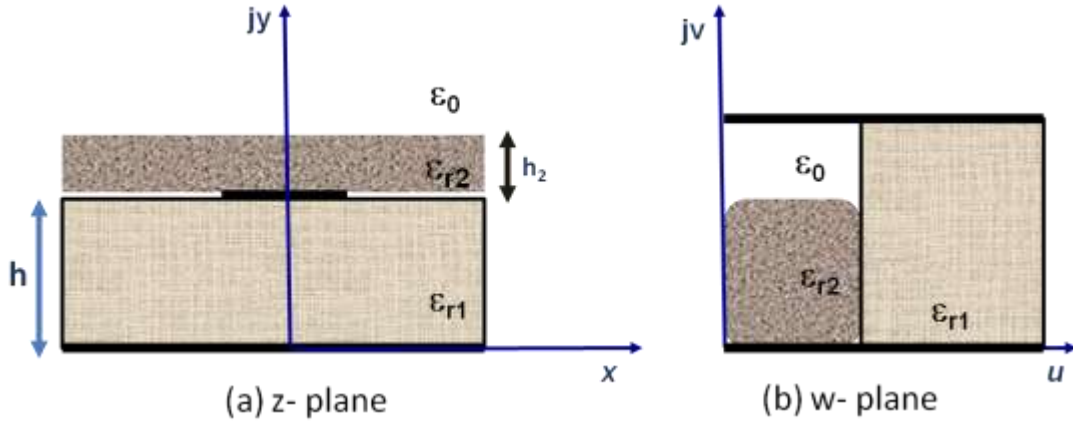
Fig. 3.15 Conformal mapping of loaded microstrip line.

After loaded with BLG/Cu microstrip line will become as a two-layer line and complex relative permittivity (ε_{r2}^*) of the second layer i.e. BLG only can be calculated by using relation [19-21]:

$$\varepsilon_{r2}^* = \frac{\varepsilon_{reff2}^*}{q_2} - \frac{q_1 \varepsilon_{r1}^*}{q_2} \tag{3.23}$$

where ε_{reff2}^* is complex effective relative permittivity, ε_{r1}^* and ε_{r2}^* are complex relative permittivity of the first layer (i.e. FR-4 substrate) and second layer (i.e. BLG), respectively. The filling factors q_1 and q_2 are given by

$$q_1 = 1 - \frac{h}{2w_{ef}} log\left(\frac{\pi w_{ef}}{h} - 1\right) \tag{3.24}$$

$$q_2 = 1 - q_2 \tag{3.25}$$

The effective line width (w_{ef}) is

$$w_{ef} = w + \frac{2h}{\pi} log \left[17.08 \left(\frac{w}{2h} + 0.92 \right) \right] \qquad (3.26)$$

where w is the width of microstrip line.

Loading with SLG/glass makes microstrip line as a three-layer line and complex relative permittivity (ε_{r3}^*) of the third layer (i.e. SLG) is given by [19-21] as illustrated in **Fig. 3.14(b)**:

$$\varepsilon_{r3}^* = \frac{\left(\varepsilon_{reff3}^* - q_1 \varepsilon_{r1}^* \right) q_3 \varepsilon_{r2}^*}{(1-q_1)^2 \varepsilon_{r2}^* - [q_2 + (1-q_1-q_2-q_3)\varepsilon_{r2}^*]\left(\varepsilon_{reff3}^* - q_1 \varepsilon_{r1}^* \right)} \qquad (3.27)$$

In Eq. (3.27), ε_{reff3}^* is complex effective relative permittivity and ε_{r1}^*, ε_{r2}^* and ε_{r3}^* are complex relative permittivity of FR-4 substrate, second layer (i.e. glass or quartz substrate) and third layer (i.e. SLG). In this case, the fillng factors q_2 and q_3 are calculated as follows:

$$q_2 = 1 - q_1 - \frac{(h-v_2)}{2w_{ef}} log \left[\frac{2w_{ef} \, cos(v_2\pi/2h)}{(2H_2h-h+v_2)} + sin(v_2\pi/2h) \right] \qquad (3.28)$$

where, $H_2 = (h + h_2)/h$, h isthickness of FR-4 and h_2 is thickness of glass or quartz, q_1 is given by Eq. (3.24). The constant v_2 is given by,

$$v_2 = \frac{2h}{\pi} tan^{-1} \left[\frac{2\pi(H_2h-h)}{(\pi w_{ef}-4h)} \right] \qquad (3.29)$$

$$q_3 = 1 - q_1 - q_2 - \frac{(h-v_3)}{2w_{ef}} log \left[\frac{2w_{ef} \, cos(v_3\pi/2h)}{(2H_3h-h+v_3)} + sin(v_3\pi/2h) \right] \qquad (3.30)$$

where, $H_3 = (h + h_2 + h_3)/h$, h_3 is thickness of SLG, and v_3 is given by

$$v_3 = \frac{2h}{\pi} tan^{-1} \left[\frac{2\pi(H_3 h - h)}{(\pi w_{ef} - 4h)} \right] \tag{3.31}$$

3.4.5 Complex refractive index

In order to study dispersion behaviour, we have obtained the refractive index (n) and extinction coefficient (κ) by using the following Eqs.[22]:

$$n = \left(\frac{\sqrt{\varepsilon_r'^2 + \varepsilon_r''^2} + \varepsilon_r'}{2} \right)^{\frac{1}{2}} \tag{3.32}$$

$$\kappa = \left(\frac{\sqrt{\varepsilon_r'^2 + \varepsilon_r''^2} - \varepsilon_r'}{2} \right)^{\frac{1}{2}} \tag{3.33}$$

where ε_r' and ε_r'' are real and imaginary parts of complex relative permittivity, respectively.

To obtain the behaviour of waves inside any material of refractive index (n), the phase velocity (v_p) is expressed as, $v_p = c/n$ where $c = 2.99 \times 10^8$ m/s, the velocity of the light in a vacuum. The group velocity (v_g) can then be deduced by using relation, $v_g = v_p - \lambda.dv_p/d\lambda$ where the wavelength is given by $\lambda = \frac{\lambda_0}{\sqrt{\varepsilon_r}}$. This group velocity will then relate with the optical effective mass of photons as, $m_{op}^* = \hbar k / v_g$ [23] where $\hbar = 1.054 \times 10^{-34}$ J.s, and k is the wave vector ($k = n\omega/c$), ω is the angular frequency. These Eqs.(3.23- 3.33) were written in MATLAB program for two-layer and three-layer lines and intrinsic complex relative permittivity of the SLG and BLG were extracted. This MATLAB program is given in **Appendix B**.

As shown in **Fig. 3.14(a),** the microstrip line with test fixture was connected between ports (A and B) of calibrated VNA model N5227A, Keysight Technologies Inc. and S-parameters were measured for unloaded and loaded microstrip line with all samples from 10 MHz to 26.5 GHz.

3.5 Simulation software- AFORS-HET

In order to optimize cell parameters of graphene as well as silicon layer heterojunction solar cells, we used a numerical simulation tool AFORS-HET (Automat FORSimulation of HETero-structures) **[24]**. AFORS-HET provides the results of basic characterization techniques like current-voltage or quantum efficiency as well as advanced characterization techniques for example photo- and electroluminescence, photoconductance decay, surface photovoltage, impedance, capacitance/conductance, intensity modulated photocurrent spectroscopy or electrically detected magnetic resonance. Its graphical interface allows the visualization, storage and comparison of all simulation data as shown in **Fig. 3.16**. In addition an arbitrary parameter variation, multi-dimensional parameter-fitting and optimization can also be performed. An arbitrary sequence of semiconducting layers can be modelled by specifying the properties for corresponding layer and interfaces. AFORS-HET uses the Shockley-Read-Hall recombination statistics to solve the one-dimensional semiconductor equations for various conditions like thermodynamic equilibrium, steady-state conditions under an external applied voltage or current and/or illumination, small additional sinusoidal modulations of the external applied voltage/illumination and transient conditions etc **[24]**.
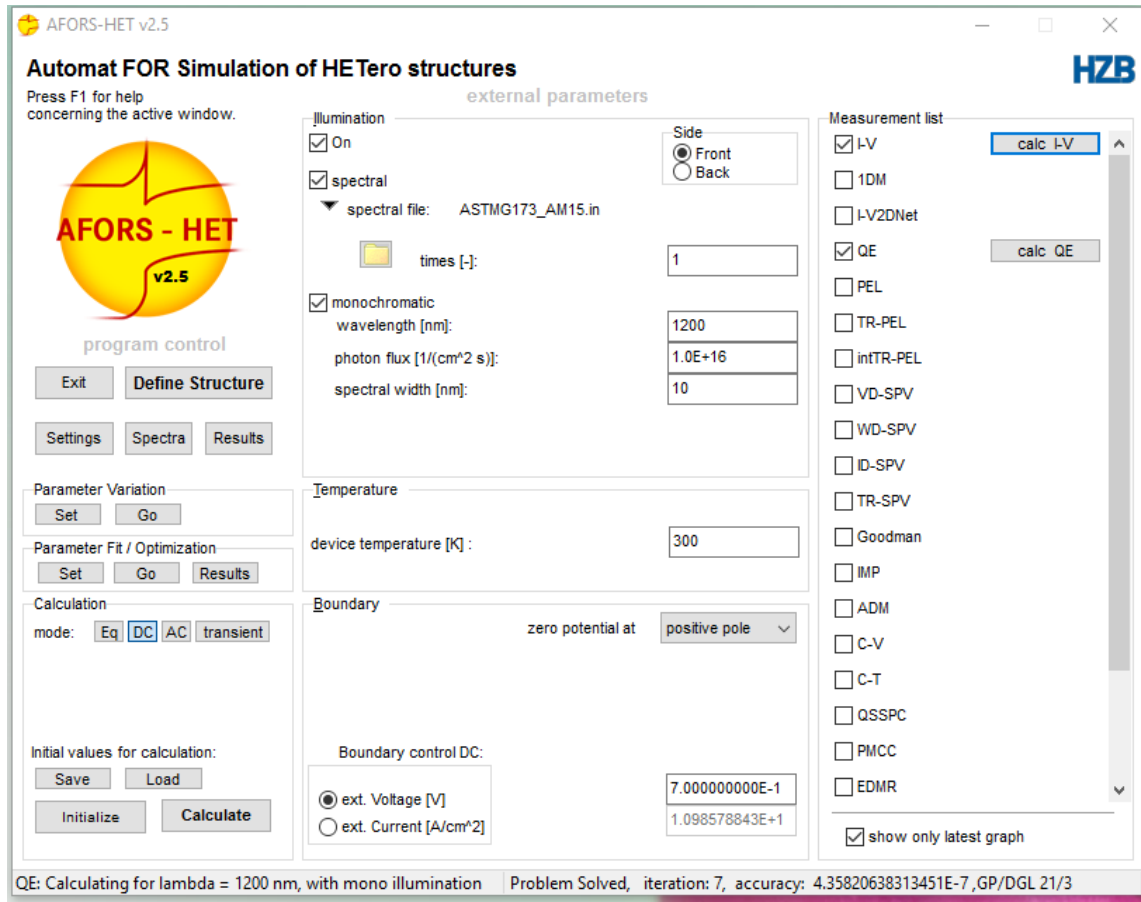
Fig. 3.16 Graphical interface of AFORS-HET software

References

[1] S. R. Jadkar, J. V. Sali, M. G. Takwale, D. V. Musale, S. T. Kshirsagar, Synthesis of highly conductive boron-doped p-type hydrogenated microcrystalline silicon (μc-Si:H) by a hot-wire chemical vapour deposition (HFCVD) technique, Solar Energy Materials & Solar Cells 64 (2000) 333-346.

[2] Z. Yu, U. Karlsson, A. Flodstrom, Influence of oxygen and nitrogen on the growth of hot-filament chemical vapor deposited diamond films, Thin Solid Films 342 (1999) 74-82.

[3] T. Itoh, Synthesis of carbon nanowalls by hot-wire chemical vapor deposition, Thin Solid Films 519 (2011) 4589–4593.

[4] J. Alvarez-Garcia, V. Izquierdo-Roca, and A. Perez-Rodriguez, Raman Spectroscopy of Thin Films for Solar cells, 14 in: Abou-Ras D, Kirchartz T, Rau U (Eds.) *Advanced Characterization Techniques for Thin Film Solar Cells* (Weinheim:Wiley-VCH) 2011, pp. 365-368.

[5] P. Rostron, S. Gaber, D. Gaber, Raman Spectroscopy, Review, International Journal of Engineering and Technical Research (IJETR) 6(1) (2016) 50-64.

[6] Z. H. Ni, H. M. Wang, J. Kasim, H. M. Fan, T. Yu, Y. H. Wu, Y. P. Feng and Z. X. Shen, Graphene thickness determination using reflection and contrast spectroscopy, Nano Lett. 7 (9) (2007) 2758-2763.

[7] H. Wang, Y. Wang, X. Cao, M. Fenga, G. Lan, Vibrational properties of graphene and graphene layers, J. Raman Spectrosc. 40 (2009) 1791-1796.

[8] A. Gupta, G. Chen, P. Joshi, S. Tadigadapa, P. C. Eklund, Raman Scattering from high-frequency phonons in supported n-graphene layer films, Nano. Lett. 6 (2006) 2667 - 2673.

[9] S. Sadewasser and I. Visoly-Fisher, Scanning Probe Microscopy on Inorganic Thin Films for Solar Cells, 11 in: D Abou-Ras, T Kirchartz, U Rau (Eds.) *Advanced Characterization Techniques for Thin Film Solar Cells* (Weinheim:Wiley-VCH) 2011, pp. 275-277.

[10] P. Queffelec, P. Gelin, J. Gieraltowski, J. Loaec, A microstrip device for the broadband simultaneous measurement of complex permittivity and permeability, IEEE Trans. Magnetics 30 (1994) 224 - 231.

[11] D. M. Pozar, *Microwave Engineering*, John Wiley & Sons, Inc. 2012, pp.8-10, 147-148, 192.

[12] J. C. Rautio, A de-embedding algorithm for electromagnetics, Int. J. Microwave Millimeter Wave Compter-Aided Engg. 1(3) (1991) 282-287.

[13] Agilent De-embedding and Embedding S-parameter Networks Using a Vector Network Analyzer, Application Note 1364-1, Agilent Technologies, Inc., USA 2004, 5980-2784EN.

[14] A. Koul, P. K. R. Anmula, M. Y. Koledintseva, J. L. Drewniak, S. Hinaga, Improved Technique for Extracting Parameters of Low-Loss Dielectrics on Printed Circuit Boards, in Proceedings of IEEE EMC Symposium, Austin, USA, 2009, p.191-196.

[15] U. A. Bakshi, A. V. Bakshi, *Network Analysis and Synthesis*, 1st ed., Technical Publications Pune, India 2008, pp. 9-3 – 9-4.

[16] E. Hammerstad, Computer-aided design of Microstrip couplers with accurate discontinuity models in Proc. of IEEE MTT-S Intl. Microwave Symp. Digest 1981, 54-56.

[17] Y. Wu, Y. Xu, Z. Wang, C. Xu, Z. Tang, Y. Chen, R. Xu, Microwave transmission properties of chemical vapor deposition graphene, Appl. Phys. Lett. 101 (2012) 053110.

[18] Cam Nguyen, *Analysis Methods for RF, Microwave, and Millimeter-Wave Planar Transmission Line Structures*, John Wiley & Sons, Inc, 2000 pp. 85-87.

[19] J. Svačina, Analysis of multilayer microstrip lines by a conformal mapping method, IEEE Trans. Microwave Theory Tech. 40 (4) (1992) 769-772.

[20] J. Svačina, A simple quasistatic determination of basic parameters of multilayer microstrip and coplanar waveguide, IEEE Microwave Guided Wave Lett. 2(10) (1992) 385-387.

[21] C. Wan and A. Hoorfar, Improved design equations for multilayer microstrip lines, IEEE Microwave Guided Wave Lett. 10 (6) (2000) 223-224.

[22] Mira Naftaly, *Terahertz Metrology*, Artech House Publishers, New York, USA, 2015, pp. 35.

[23] V. Ariel, A. Natan, Electron Effective Mass in Graphene, 2012 e-print arXiv:1206.6100v2 [physics.gen-ph].

[24] R. Stangl, M. Kriegel, M. Schmidt, AFORS-HET, Version 2.2, a numerical computer program for simulation of heterojunction solar cells and measurements, in Proceedings of the WCPEC-4, Fourth World Conference on Photovoltaic Energy Conversion, Hawaii, USA, 2006, p. 1350-1353.

Chapter 4

Anomalous dispersion with exotic microwave transmission and dielectric properties in single layer graphene

4.1 Introduction

In this chapter, the results of microwave characterization using microstrip line based measurement fixture are discussed in details. The measured reflection and transmission parameters of both unloaded and loaded microstrip line in frequency range of 100 MHz to 10 GHz studied and then attenuation and phase constant parameters of loaded microstrip line were determined. The performance of adopted method for de-embedding is also studied in terms of effective relative permittivity, phase velocity and group velocity with those obtained from standard de-embedding method based on [ABCD] parameters. The percent error obtained for each parameter is also estimated and found to be < 4 %.The results presented in this chapter have been published in **Kamlesh Patel and Pawan K Tyagi, Journal of Alloys and Compounds 706 (2017) 250-259**,http://dx.doi.org/10.1016/j.jallcom.2017.02.184.

4.2 Microwave reflection and transmission characterization

4.2.1 Reflection and transmission properties of single layer graphene/substrate

The measured reflection (S_{11}, S_{22}) and transmission (S_{12}, S_{21}) parameters of unloaded microstrip line, loaded with glass and graphene/glass substrate have been illustrated in **Figs. 4.1(a-h)**. The parameters such as S_{11} and S_{22} represent the reflection

at input port 1 and output port 2, respectively and the lower value in dB for S_{11} or S_{22} indicates that reflection from line is less or line is matched. In the S_{11} and S_{22} magnitude response, multiple peaks are noticed at a regular interval of frequency (Δf). Since we have taken a microstrip line of length 50.8 mm, the frequency interval for multiple peaks can be estimated from $n\Delta f = nc/(2l\sqrt{\varepsilon_{reff}(f)})$, where $\varepsilon_{reff}(f)$ is the effective relative permittivity for the microstrip line used. For n=1 to 7, we have estimated the frequency intervals as 1.61 GHz, 3.19 GHz, 4.77 GHz, 6.30 GHz, 7.80 GHz, 9.33 GHz and 10.78 GHz in 100 MHz to 10 GHz range. The lower peaks in S_{11} (or S_{22}) response also represent the cancellation of reflections and re-reflections i.e. multiple reflections from the coaxial connectors connected at the input port 1 and output port 2 of the microstrip line under measurement **[1]**. It is also possible for some re-reflected waves to cancel out each other at frequencies other than estimated, which may be indicated by the presence of additional peaks. So peaks are observed at 1.6 GHz, 2.37 GHz,3.00 GHz,3.46 GHz, 4.36 GHz, 5.38 GHz, 6.63 GHz, 7.70 GHz, 8.47 GHz and 9.16 GHzin measured S_{11} (or S_{22}) responses shown in **Fig.4.1(a &g)**. Shift in frequency intervals from the estimated ones might be occurred due to non-consideration of imperfect coaxial connectors and microstrip line dispersion with frequency. The phase response of S_{11} (or S_{22}) in **Fig.4.1(b &h)** contains peaks of values ±180°, where the average reflected wave changes phase against the incident signal.As shown in **Figs. 4.1(a-b)**, input reflection coefficient (S_{11}) magnitudes are observed to be high for glass and graphene/glass loadings on the microstrip line except upper peak at 697 MHz. It is also noticed that after loading the microstrip line with glass or graphene/glass, lower peaks observed at frequencies, 1.6 GHz, 5.38 GHz and 7.7 GHz shift towards low frequency. Similar results were obtained for S_{11} phase.

The S_{21}(or S_{12}) magnitude response as shown in **Fig. 4.1 (c & e)** represent transmission over the microstrip line. Lower the value in dB for S_{21}(or S_{12}) indicates transmission loss due to signal reflection and/or absorption in transmission line used. Smaller peaks are observed at 637 MHz, 837 MHz, 2.35 GHz, 5.65 GHz (upper), 6.03 GHz, 6.22 GHz and 8.57 GHz. As multiple reflections in S_{11} and S_{22} responses are noticed, re-reflections from both connectors caused peaks at these frequencies in S_{21} (and S_{12}) magnitude responses **[1]**. The S_{21} (and S_{12}) phase response shows the transmission phase, which is the phase difference between the transmitted and incident waves. It is measured between ±180° by the VNA, the peak positionsoccur at the frequency where the phase is 180° or - 180°. In the measured response of S_{21}(and S_{12}) phase as shown in **Fig.4.1(d & f)**, peak positions are found be at nearly 1.01 GHz, 2.95 GHz, 4.86 GHz, 6.79 GHz and 8.62 GHz. As shown in **Figs. 4.1(c-f)**, forward (S_{21}) and reverse (S_{12}) transmission magnitudes decreased as frequency increased. This might be happened due to the lossy behaviour of microstrip line on FR-4 substrate with frequency. On comparison with data of unloaded microstrip line, lower values of S_{21} and S_{12} were found. This observation confirmed that the transmission loss is increased after loading microstrip line with glass and graphene/glass and exhibited similar properties upto 5 GHz. Also, the shift in phase values was found to become prominent with an increase in frequency. **Figs. 4.1(g–h)** shows that the values of S_{22} parameters in all the three cases have similar pattern like S_{11}. Additional fluctuations observed above 4 GHz represent more signals reflected in different amounts and magnitude (<-15 dB) was found upto 8 GHz. The microstrip line has shown more reflections above 9 GHz, which reduced transmission significantly and can also seen as low values of S_{12} and S_{21}.

The measured S-parameters for the unloaded microstrip line and loaded with quartz and graphene/quartz have been shown in **Figs. 4.2(a-h)**.
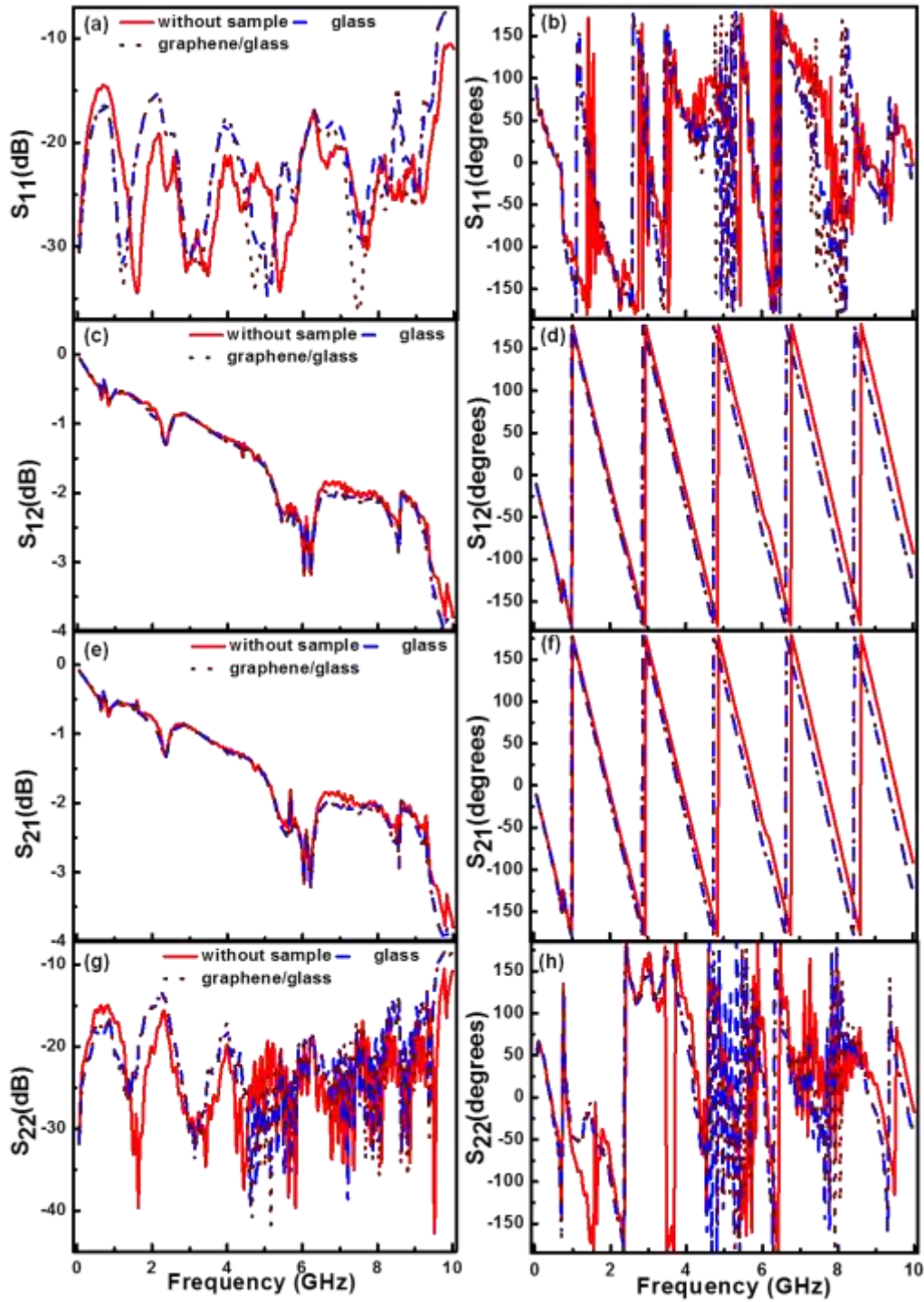
Fig. 4.1 Complex S-parameters of different measurement configurations for without sample, with glass and graphene/glass, (a) magnitude of S_{11}, (b) phase of S_{11}, (c) magnitude of S_{12}, (d) phase of S_{12}, (e) magnitude of S_{21}, (f) phase of S_{21}, (g) magnitude of S_{22} and (h) phase of S_{22}.
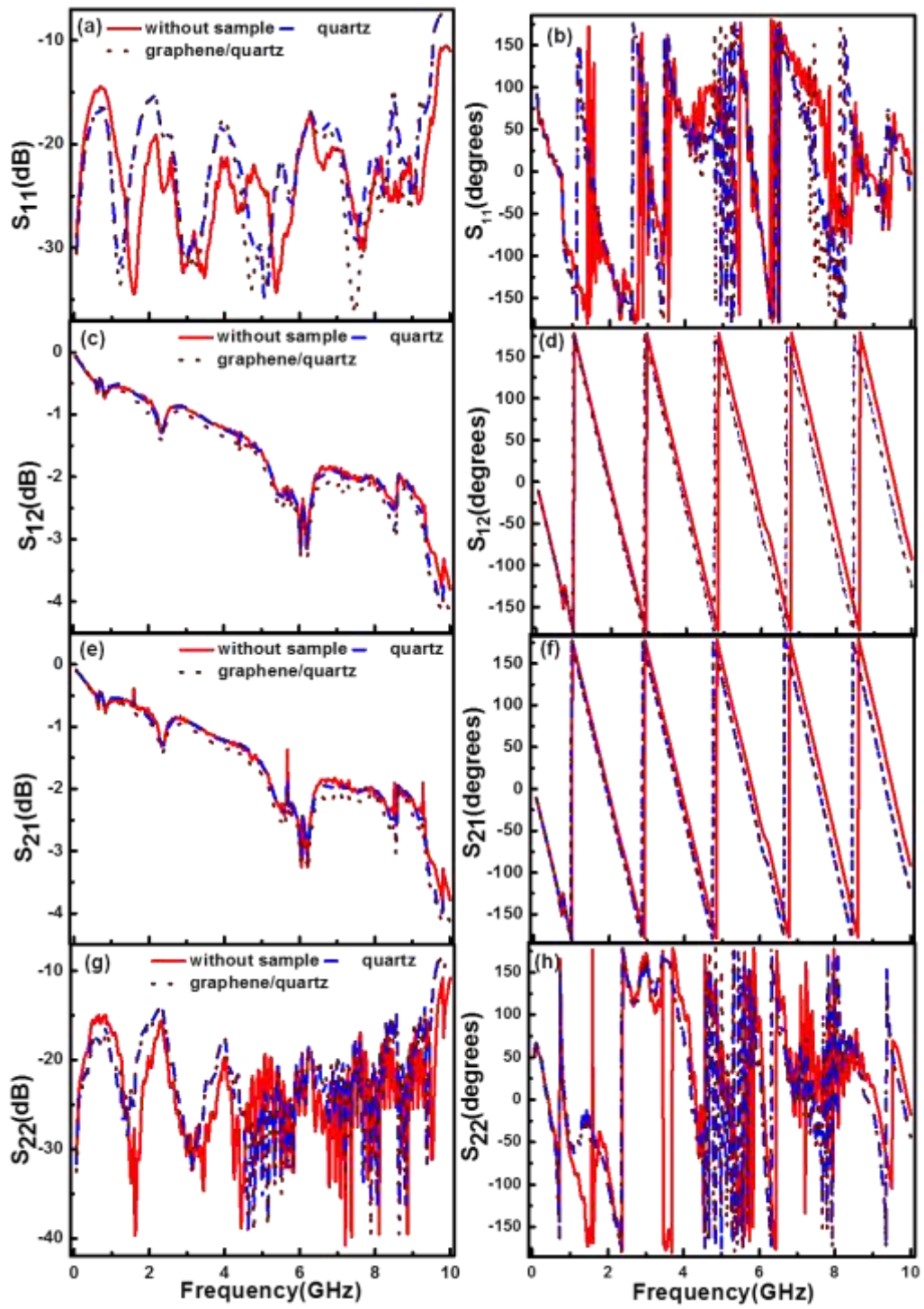
Fig. 4.2 Complex S-parameters of different measurement configurations for without sample, with quartz and graphene/quartz , (a) magnitude of S_{11}, (b) phase of S_{11}, (c) magnitude of S_{12}, (d) phase of S_{12}, (e) magnitude of S_{21}, (f) phase of S_{21}, (g) magnitude of S_{22} and (h) phase of S_{22}.

The behaviour of reflection parameters (S_{11} and S_{22}) is found similar to previous case and only magnitude was slightly changed only at the peaks. The transmission coefficient (S_{21}& S_{12}) observations as shown in **Figs. 4.2(c-f)** suggest that graphene/quartz have additional losses as compared to quartz, which is a low loss material. In present case, when we compared the S_{21} and S_{12} parameters of unloaded and loaded microstrip line, both exhibited similar behaviour. However, the changes in the S_{21} and S_{12} phases are found to be identical for quartz and graphene/quartz, which are found to be increased with the frequency. We have also noticed a little variation in S_{11} and S_{22} parameters for both graphene/glass and graphene/quartz which reveals that well-matched characteristic impedance can be obtained with graphene. Identical S_{21} and S_{12} parameters further confirmed that graphene is passive and isotropic material. Such properties of graphene can be utilized in a reciprocal microwave component if few layer graphene with well-matched characteristic impedance can be made.

4.2.2 Attenuation and phase constant of single layer graphene/substrate

By employing ABCD de-embedding method, de-embedded S-parameters of Part 2 were obtained and then complex propagation constant ($\gamma = \alpha + j\beta$) was determined for each loadings i.e. glass, graphene/glass, quartz, and graphene/quartz **[2]**, where α is the attenuation constant and β is the phase constant. The results are plotted in**Fig. 4.3**. Few peaks in **Fig. 4.5(a)** were observed at 737 MHz, 2.65 GHz, and 3.98 GHz (lower), 5.54 GHz, 6.61 GHz (lower), 7.96 GHz, 8.43 GHz, 9.02 GHz and 9.18 GHz (lower), which correspond to the peaks observed in S-parameters (**Fig. 4.1** and **Fig. 4.2**) and their values were found to depend more on the reflection not on the transmission. The attenuation constant was found to be high in both cases graphene/glass and graphene/quartz compared to unloaded case. This reveals that more microwave

75

absorption takes place as reported in previous studies **[3]**. Loses are found to be more in graphene/glass than the graphene/quartz. Also, as shown in **Figs. 4.3(b & d)**, the phase constant (β) were found to be overlapping at most frequencies. However, infinitesimal changes were also observed at the peaks. So, it can be concluded that βof graphene/glass and graphene/quartz are lagging in comparison to the glass and quartz. Although for the graphene/glass, β was found to be larger than that of graphene/quartz, their phase constant difference too varies with frequencies.
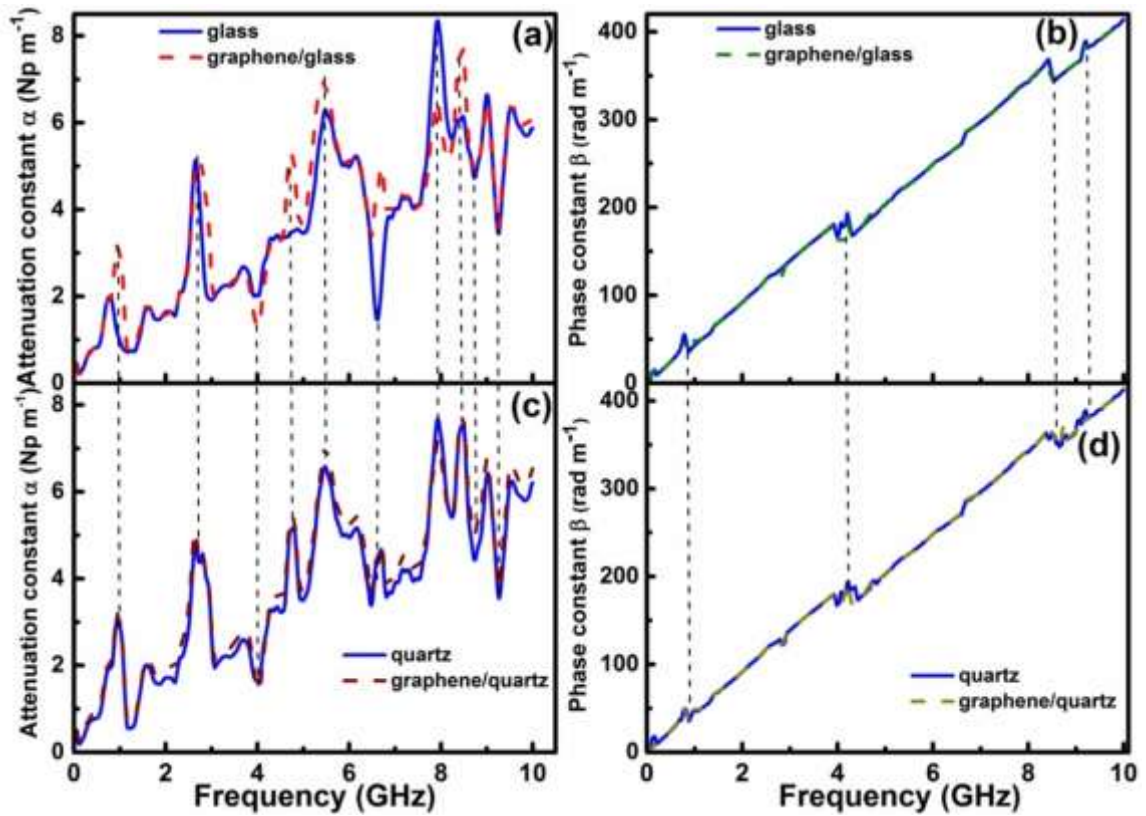
Fig. 4.3(a) Attenuation constant, (b) phase constant for glass and graphene/glass, (c) attenuation constant, and (d) phase constant for quartz and graphene/quartz.

4.3 Comparison of both de-embedding methods for single layer graphene/substrate

4.3.1 Effective relative permittivity

The complex propagation constants were obtained for Part 2 of the microstrip line, which is the multilayer loaded microstrip lineusing the ABCD and adopted de-embedding method. The effective relative permittivity(ε_{reff}) was then obtained from the frequency dependent complex propagation constant for these materials as $\varepsilon_{reff} = (\gamma_2/\gamma_0)^2$ [4]. The real and imaginary parts of ε_{reff} obtained by two de-embedded methods were plotted as shown in **Fig. 4.4** and **Fig. 4.5**.
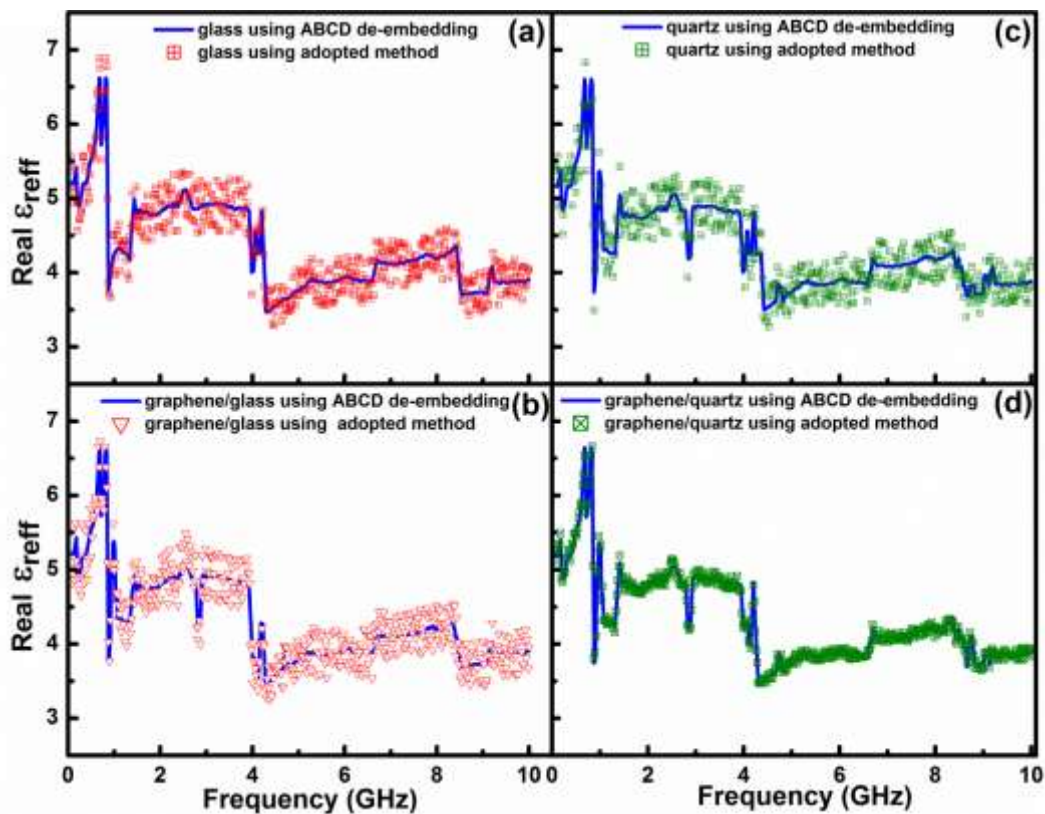
Fig. 4.4 Real ε_{reff} using ABCD and adopted method (a) glass, (b)graphene/glass, (c) quartz and (d) graphene/quartz.

The real ε_{reff} of glass and graphene/glass are found to be in range of 4.80 to 3.89 while for quartz and graphene/quartz, these values are in range of 4.76 to 3.87 in 2 - 10 GHz frequency range. Similar values of real ε_{reff} from 5.5 to 3 in 500 MHz to 6 GHz have been evaluated for graphene/glass earlier [4]. Slightly high real ε_{reff} for graphene/glassmight be due to higher thickness of graphene layer on glass (0.334 nm) than on the quartz(0.331 nm). Steep peaks and falls in real ε_{reff} values were observed in frequency below 1 GHz as ε_{reff} of the microstrip line is highly frequency dependent in lower range.The percent error is below 4% in the real ε_{reff} values obtained from standard ABCD and adopted de-embedding methods.
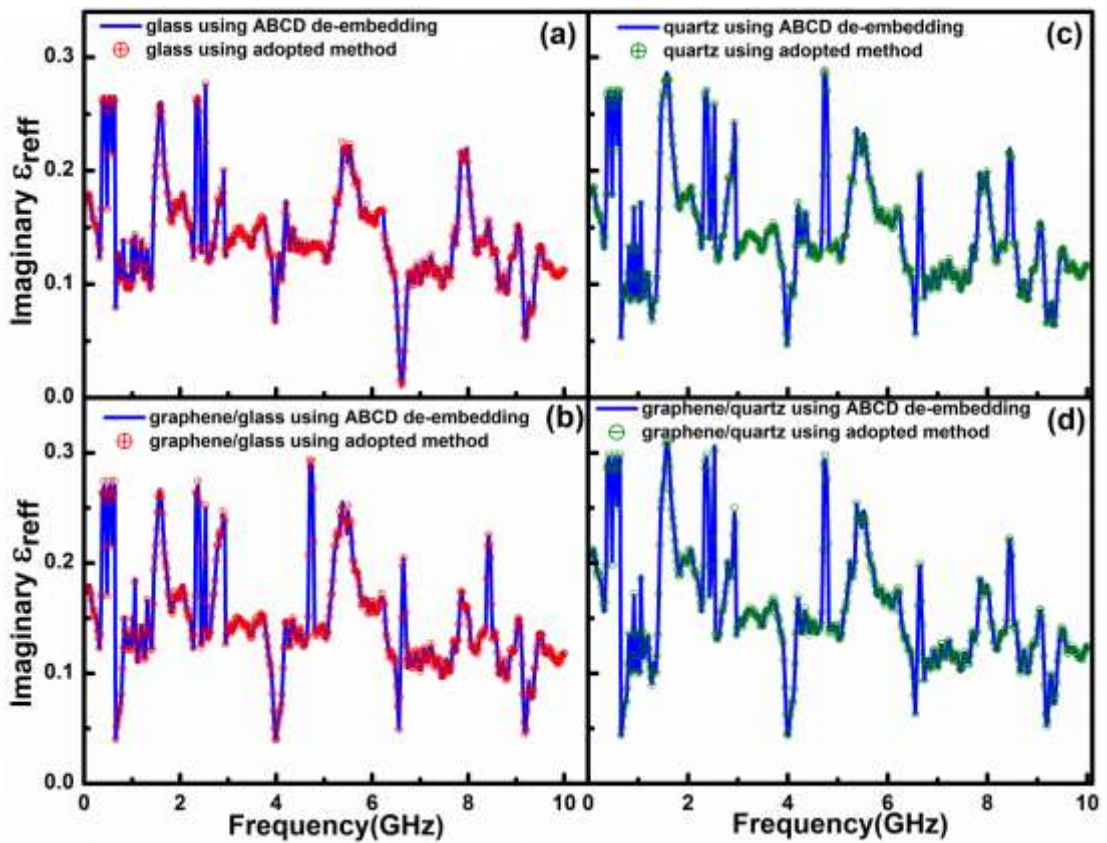
Fig. 4.5 Imaginary ε_{reff} using ABCD and adopted method (a) glass, (b) graphene/glass, (c) quartz and (d) graphene/quartz.

As shown in **Fig. 4.5** the imaginary part of ε_{reff} for glass, graphene/glass, quartz and graphene/quartz were found to be ~ 0.15 in major frequency range from 100 MHz to 10 GHz. In addition, certain peak values between 0.05 to 0.5 in imaginary ε_{reff} were observed at 1 GHz (lower), 3 GHz (lower), 4 GHz (upper) and 5 GHz (lower). The imaginary ε_{reff} forgraphene/glass and graphene/quartz were found to be high than for glass and quartz loadings and at frequency ~ 6.61 GHz, sharp upper and lower peaks were seen, whereas lower magnitude of peaks in case of glass substrate was observed. The percent error in the imaginary $\varepsilon_{reff}$is obtained below 1% on comparing the results obtained from the standard ABCD and the adopted de-embedding methods. This again confirms that adopted method is accurate de-embedding method and can be applied for faster and simpler calculation to obtain the microwave properties like the effective relative permittivity etc.

4.3.2 Phase velocity

On further analysis, phase velocities (v_p) in presence of graphene layers have been obtained from both de-embedding methods and compared in **Fig. 4.6(a-d)**. With frequency, the phase velocities for all studied materials were increased from 5.74×10^7 m/s @ 100 MHz to 7.67×10^7 m/s @ 10 GHz. **Fig. 4.6** shows that v_p also has some peaks or falls at frequencies 817 MHz (lower), 877 MHz (upper), 2.82 GHz (upper, not observed in case of glass), 4.38 GHz (upper), 6.6 GHz (lower) and 8.53 GHz (upper). It is observed that in the case of microstrip line loadings with graphene/glass and graphene/quartz, v_p was found to be lower than that of microstrip line loaded with bare glass and quartz. This confirms that the waves propagation becomes slower in graphene. As the peaks of v_p shifted slightly towards high frequency for quartz and

graphene/quartz, the waves propagate faster in quartz and graphene/quartz than in the glass and graphene/glass.
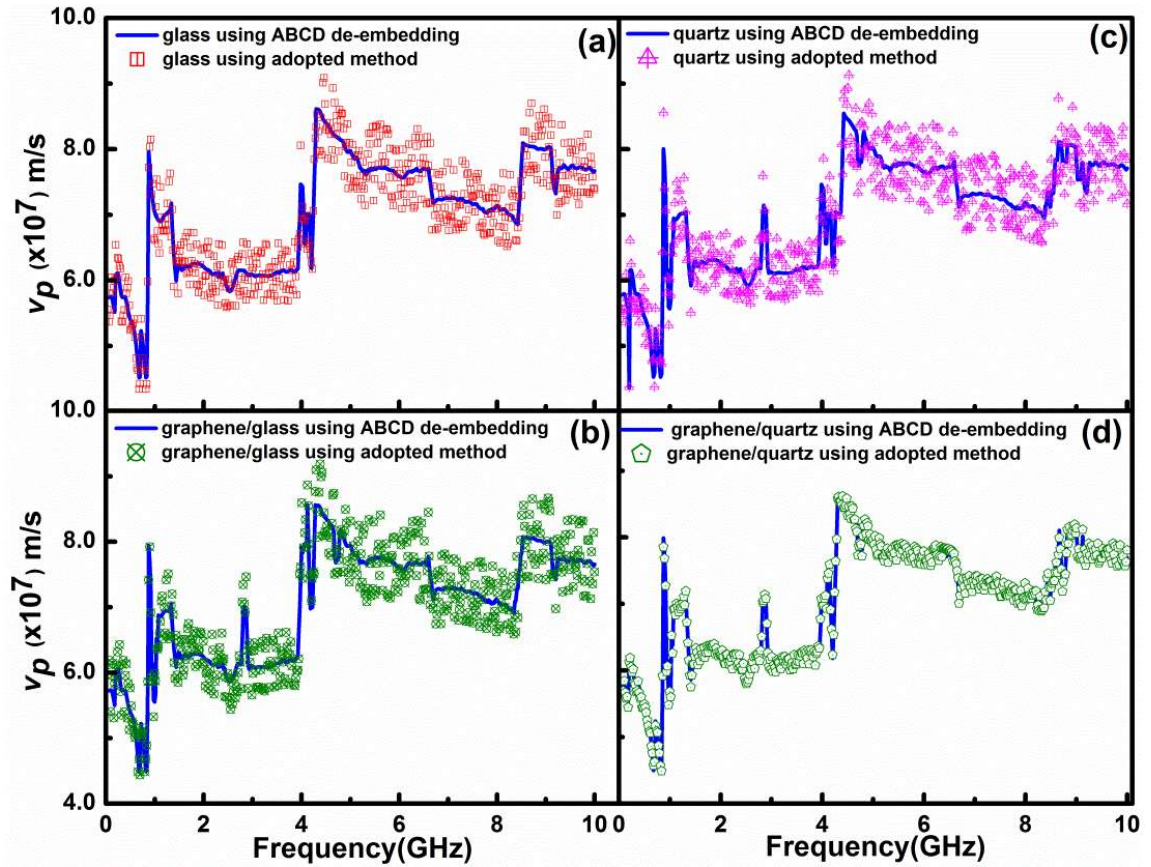
Fig. 4.6 Phase velocity v_p(m/s) using ABCD and adopted method (a) glass, (b)graphene/glass, (c) quartz and (d) graphene/quartz.

4.3.3 Group velocity

The phase velocities from both de-embedding methods were used to obtain the group velocities for the respective loadings and shown in **Fig. 4.7(a-d)**. The group velocity (v_g) has been decreased from 1.6×10^9 m/s @ 100 MHz to 1.1×10^9 m/s @ 10 GHz. A peak of ~2.0×10^9 m/s at 817 MHz and falls at certain frequencies were observed in v_g as shown in **Fig. 4.7(a – d)**, which correspond to sharp fall or rise in the

phase velocity (v_p). In graphene/glass and graphene/quartz, higher v_g signals that the wave packets are moving faster than those formed in glass and quartz in the measured frequency range. Largerv_g than the velocity of light (c) and v_p as well, confirms that the studied materials are anomalous dispersive and absorb more microwaves in the presence of graphene.
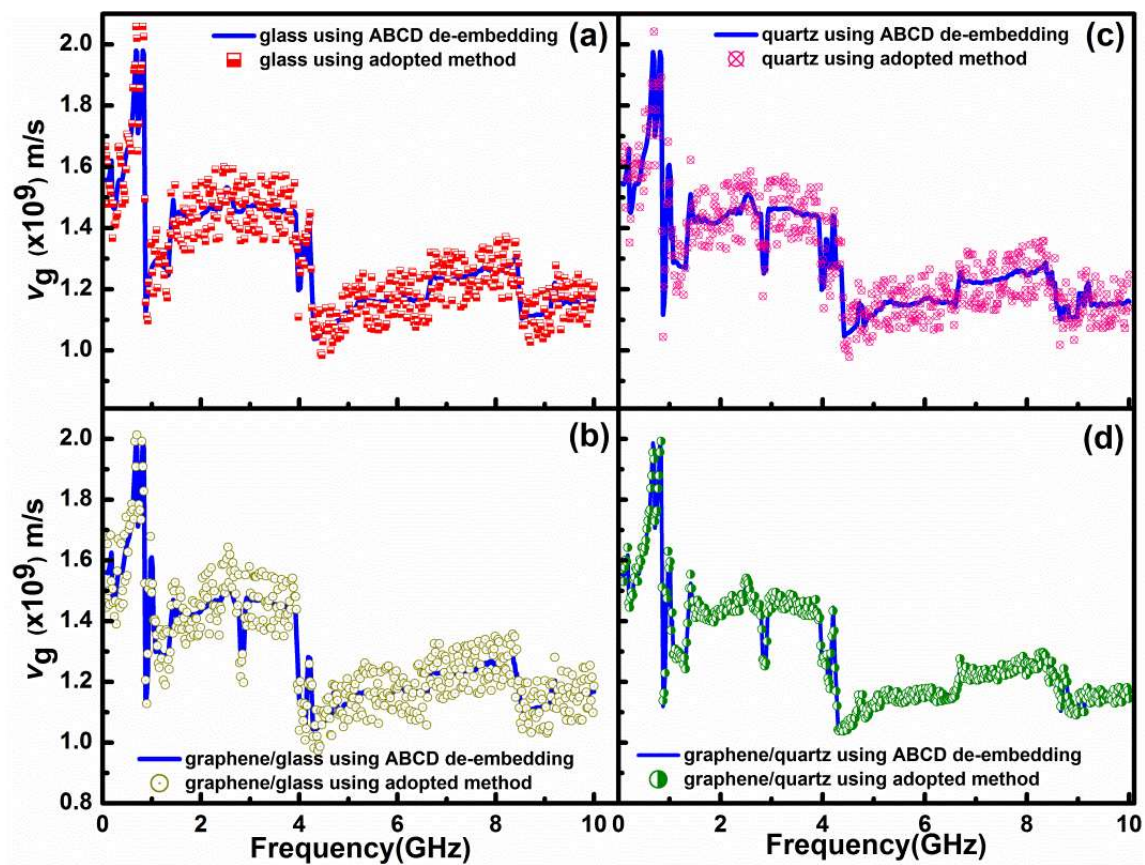
Fig. 4.7 Group velocity v_g (m/s) using ABCD and adopted method (a) glass, (b)graphene/glass, (c) quartz and (d) graphene/quartz.

Transparent substrates like glass and quartz have selective absorption bands in the infrared and ultraviolet regions and posses anomalous dispersion, lower in the microwave region **[5-6]**. For our graphene/substrate, higher ε_{reff} andv_g indicates that the

amount of anomalous dispersion has been increased as compared to bare substrate. Thus, the single graphene layer on glass and quartz is found to have anomalous dispersion. This may happened due to lower charge carrier concentration and interelectron interaction in the measured frequency range [7]. As group velocity represents the velocity at which the microwave energy is propagated, and found to be larger than v_p, confirms thathigh frequency waves propagate faster than those having lower frequencies in the single layer graphene/substrate. The values of v_g and v_p from both de-embedding methods were compared and the percent error is found to be below 3%.

4.4 Summary

In this chapter, we have reported the microwave transmission and dielectric properties of CVD-grown single layer graphene on glass and quartz substrates which have been studied in frequency range of 100 MHz to 10 GHz.De-embedding method based on the propagation constants is adopted to determine the effective relative permittivity of graphene layer. Graphene layer deposited on the substrate is found to exhibit higher absorption than the bare glass as well as quartz substrate in range of 2 - 10 GHz. We compared all parameters obtained by using standard ABCD de-embedding method and adopted method and found to be similar. This confirmed that the adopted method can be used to estimate the effective relative permittivity accurate and also the phase and group velocities. In both cases, graphene on glass and quartz, the maximum values of phase velocity are found to be $\sim 8.57 \times 10^7$ m/s at 4.12 GHz and $\sim 9.13 \times 10^7$ m/s at 4.52 GHz, respectively whereas the respective maximum group velocities for these materials are found to be $\sim 2.0 \times 10^9$ m/s and $\sim 1.9 \times 10^9$ m/s at 817 MHz. The

experimental results show that in graphene, phase velocity of waves decreased whereas the group velocity increased. The observed anomalous dispersion in the single layer graphene/substrate causes the absorption of microwaves in the frequency range of 100 MHz - 10 GHz as $v_g > v_p$.

The work presented in this chapter has two contributions, first validation of our adopted de-embedding method based on the propagation constants against the existing [ABCD] based method **[8-9]** which also requires impedance determination taking account for asymmetry at the edges of graphene/substrate **[2]**. Our adopted method is comparatively easierto deduce the complex effective relative permittivity on loading with graphene/glass, which are found similar to reported earlier **[4]**. Since the occurrence of strong optical anomalous dispersion has been reported in single layer graphene (SLG) and bilayer graphene (BLG) at 633 nm using Picometrology **[10]**. So the second contribution is the confirmation of anomalous dispersion in the single layer graphene at the microwave frequency range by utilizing simple method, where we compared the phase velocity and group velocity relationship in presence of graphene.

References

[1] D. M. Pozar, *Microwave Engineering*, 4th ed, John Wiley & Sons, Inc., USA, 2012, pp.147.

[2] A. Koul, P. K. R. Anmula, M. Y. Koledintseva, J. L. Drewniak, S. Hinaga, Improved Technique for Extracting Parameters of Low-Loss Dielectrics on Printed Circuit Boards, in Proceedings of IEEE EMC Symposium, Austin, USA, 2009, p.191-196.

[3] B. Wu, H. M. Tuncer, A. Katsounaros, W. Wu, M. T. Cole, K. Ying, L. Zhang, W. I. Milne, Y. Hao, Microwave absorption and radiation from large-area multilayer CVD graphene, Carbon 77 (2014) 814 -822.

[4] Y. Wu, Y. Xu, Z. Wang, C. Xu, Z. Tang, Y. Chen, R. Xu, Microwave transmission properties of chemical vapor deposition graphene, Appl. Phys. Lett. 101 (2012) 053110.

[5] J. P. Glusker, M. Lenis, M. Rossi, *Crystal Structure Analysis for Chemists and Biologists*, Wiley-VCH Inc., Canada 1994, pp. 592.

[6] P. Yadav, Engineering Physics, Discovery Publishing House, New Delhi 2006, pp.109-110.

[7] Z. Z. Alisultanova and R. P. Meilanov, On the theory describing graphene in an anomalous-dispersion region, Journal of Surface Investigation. X-ray, Synchrotron and Neutron Techniques 7(1) (2013) 46–50.

[8] J. C. Rautio, A de-embedding algorithm for electromagnetics, Int. J. Microwave Millimeter Wave Compter-Aided Engg. 1(3) (1991) 282-287.

[9] Agilent De-embedding and Embedding S-parameter Networks Using a Vector Network Analyzer, Application Note 1364-1, Agilent Technologies, Inc., USA 2004, 5980-2784EN.

[10] X. Wang, Y. P. Chen and D. D Nolte, Strong anomalous optical dispersion of graphene: complex refractive index measured by Picometrology, Optics Express 16(26) (2008) 22105.

Chapter 5

Optical effective mass of photon in single layer and

bilayer graphene

5.1 Introduction

In this chapter, the results of microwave measurements performed in microstrip line based fixture for unloaded microstrip line and loaded with single layer graphene transferred on glass/quartz, and with bilayer graphene/Cu sampled are discussed in details. The complex relative permittivity and complex refractive index of studied material are extracted using conformal mapping technique and are discussed in detail for frequency range of 10 MHz to 26.5 GHz which is found to be little dispersive in the lower frequency range below 2 GHz.Afterwards, the phase velocity and group velocity are presented to describe the behavior of waves inside the single layer and bilayer graphene. Finally, by applying by the wave-particle duality by associating a photon with a wave-packet, and particle velocity (v_p) with group velocity (v_g) of wave-packet, the results for optical mass of photons in single layer and bilayer graphene are discussed. The results presented in this chapter have been published in **Kamlesh Patel and Pawan K. Tyagi**, **Carbon 121 (2017) 56-62**, http://dx.doi.org/10.1016/j.carbon.2017.05.057.

5.2 Microwave characterization of bilayer graphene/Cu

5.2.1 Reflection and transmission properties of bilayer graphene/Cu

The measured reflection (S_{11}, S_{22}) and transmission (S_{12}, S_{21}) parameters of both unloaded microstrip line and the ones loaded with BLG/Cu$_1$ and BLG/Cu$_2$, have been

compared and plotted in**Fig. 5.1(a-h)**. Similar to S-parameter responses in **Fig. 4.1** and **Fig. 4.2,** multiple peaks are noticed in the magnitude and phase responses for these measurements.Since S-parameter measurements are performed by connecting coaxial connectors at both end of the microstrip line, discontinuity occurs at the coaxial connector/microstrip line interface and multiple reflections are generated in broad frequency range **[1]**. These reflections cause the peaks in S-parameter responses. In measurement results shown for S_{11} (or S_{22}) responses in **Fig.5.1(a &g)**, peaks are observed at 859 MHz, 1.44 GHz, 3.03 GHz, 4.34 GHz, 5.63 GHz, 7.86 GHz, 9.24 GHz, 12 GHz, 13.44 GHz, 14.71 GHz, 16.68 GHz, 18.11 GHz, 19.49 GHz, 20.98 GHz, 22.46 GHz and 23.85 GHz. The shift in the frequency interval from estimated values is also noticed in these measurements. The phase change in average reflected wave is shown in the S_{11} (and S_{22}) phase responses.

Input reflection coefficient (S_{11}) is found to be high for BLG/Cu$_1$ and BLG/Cu$_2$ in the frequency range up to 11 GHz. As electromagnetic fields confined into FR-4 substrate and bilayer graphene covered by Cu, which eventually observed the change in effective impedance of microstrip line **[1]**. In **Fig. 5.1(a)**, BLG/Cu$_2$ is found to be more reflective than BLG/Cu$_1$ in lower frequency range <10 GHz. At further higher frequency, more field lines are in FR-4 substrate, so S_{11} for both loadings is almost unchanged and has similar values as for the unloaded microstrip line from about 11 GHz to 26.5 GHz. The phase of S_{11} also has frequent shifts at lower frequencies below 10 GHz and only one lower shift near 20 GHz in the range 15 to 26.5 GHz is seen in **Fig. 5.1(b)**. As the phase change of S_{11} is similar for BLG/Cu$_1$ andBLG/Cu$_2$, it indicates both may have same material reflection properties.

In **Fig. 5.1(c & e)**, S_{12} and S_{21} magnitudes present the transmission of microwave signal with some smaller peaks. These peaks are obtained at 806 MHz, 2.82

GHz, 5.95 GHz, 10.15 GHz, 14.07 GHz, 21.88 GHz, 23.20 GHz and 24.42 GHz due to multiple reflections. The frequencies corresponds to 180°or -180° phase change are found as 1.018 GHz, 3.09 GHz, 5.16 GHz, 7.17 GHz, 9.19 GHz, 11.16 GHz, 13.12 GHz, 15.08 GHz, 16.99 GHz, 18.96 GHz, 20.82 GHz, 22.57 GHz and 24.91 GHz and has a frequency interval 2 ± 0.14 GHz. Most of these frequencies are near to frequency interval values obtained in S_{11} (or S_{22}) magnitude responses (**Fig. 5.1**).In **Fig. 5.1(c & e)**, the magnitudes of forward (S_{21}) and reverse (S_{12}) transmission parameters are found to be decreased as frequency increased and this might be due to the lossy nature of microstrip line. Lower values of S_{21} and S_{12} for BLG/Cu$_1$ and BLG/Cu$_2$ pointed towards transmission loss on loading of microstrip line. Up to 13 GHz, BLG/Cu$_2$ has shownhigher transmission loss than BLG/Cu$_1$ except near 9 GHz, and then both S_{21} and S_{12} parameters decreased in same order with frequency. In addition, high values greater than -15 dB of S_{11} and S_{22} suggested that unloaded microstrip line became higher reflecting at frequencies above 9 GHz. For BLG/Cu$_1$ and BLG/Cu$_2$ loading, a minor shift of transmission phase is observed in comparison to microstrip line as shown in **Fig. 5.1(d & f)**. In **Fig. 5.1(g & h)**, S_{22} has shown high values for both loadings on unloaded microstrip line and the reflection (S_{22}) phase changes values analogous to that of S_{11}. For both BLG samples, little variations in S_{11} (and S_{22}) and identical S_{21} (and S_{12}) suggested that BLG can offer a reciprocal and moderate dielectric loss of 2 to 5 dB.
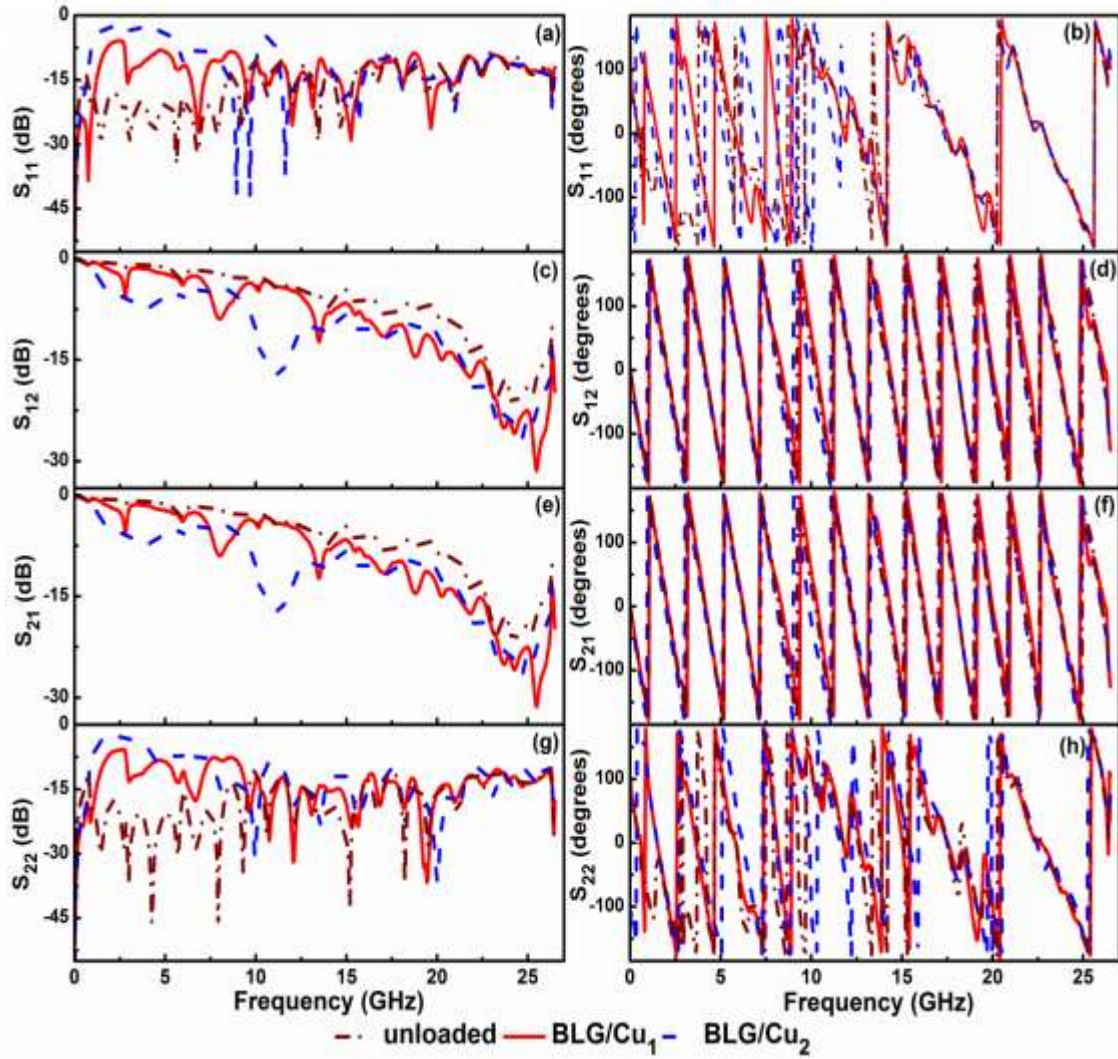
Fig. 5.1 Complex S-parameters of microstrip line unloaded, loaded with BLG/Cu$_1$ and BLG/Cu$_2$, (a) magnitude of S$_{11}$, (b) phase of S$_{11}$, (c) magnitude of S$_{12}$, (d) phase of S$_{12}$, (e) magnitude of S$_{21}$, (f) phase of S$_{21}$, (g) magnitude of S$_{22}$ and (h) phase of S$_{22}$.

Similarly, the microwave reflection and transmission properties of single layer graphene transferred on glass and quartz were obtained and found to be same as discussed in Section 4.2 of chapter 4. Multiple measurements for both loaded and unloaded microstrip line have been taken to minimize the measurement error. We have compared the three measurement results to estimate the measurements errors and the maximum measurement errors were found to be ~ 6.8 % and 11 % in magnitude and

phase values of S-parameters, respectively. The details of multiple measurements (see Fig. C1-7 in **Appendix C**) and maximum standard deviation associated with each S-parameter are given in Table C1 in **Appendix C**.

5.3 Graphene properties in the microwave frequencies

To distinguish graphene films on various substrates, single layer graphene films transferred on glass and quartz respectively are continued to be designated as SLG/glass and SLG/quartz, and two bilayer graphene films deposited on Cu sheets at different synthesis conditions are designated as BLG/Cu_1 and BLG/Cu_2. After de-embedded S-parameters for loaded microstrip line with SLG/glass, SLG/quartz, BLG/Cu_1 and BLG/Cu_2, the complex propagation constant ($\gamma = \alpha + j\beta$) was determined **[2]**, where α is the attenuation constant and β is the phase constant. The effective relative permittivity ε_{reff2} of multilayer microstrip line (Part 2) was calculated using $(\gamma_2/\gamma_0)^2$ **[3]**, where $\gamma_0 = j2\pi f/c$, f is operating frequency in Hz and c is the velocity of light in m/s. By applying the conformal mapping technique **[4-6]**, we obtained the complex relative permittivity (ε_r^*) of both SLG and BLG using formulas which have given in Section 3.4 of chapter 3. Based on these formulas, the intrinsic properties of these graphene layers extracted using the MATLAB program are given in **Appendix B**.

5.3.1 Complex relative permittivity

Fig. 5.2 shows the complex relative permittivity (ε_r) consisting of real part ($\varepsilon_r^{'}$) and imaginary part ($\varepsilon_r^{''}$) for all graphene films and the results are compared with those of the bare glass properties to validate the evaluation process.
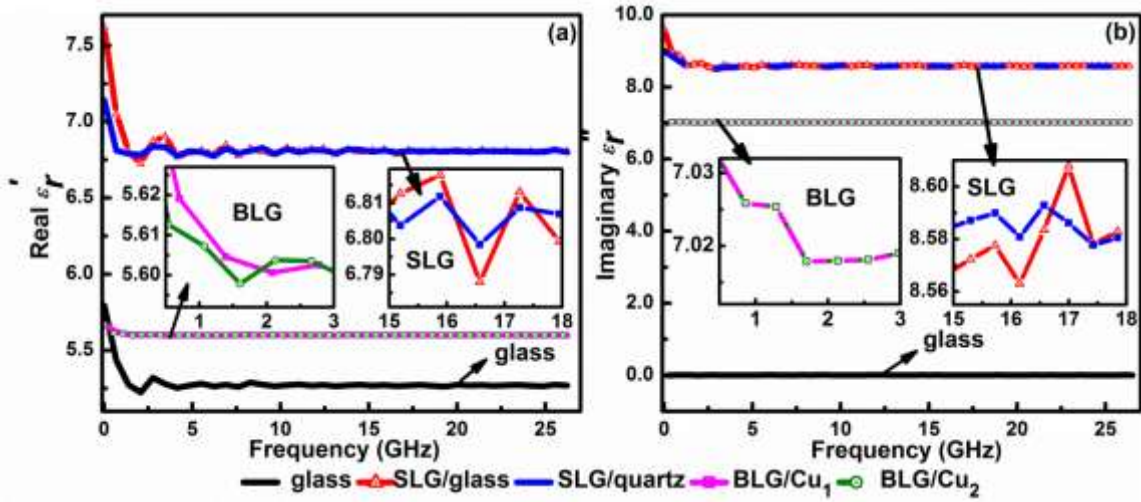
Fig. 5.2 (a) Real (ε_r')and (b) imaginary (ε_r'')parts of complex relative permittivity (ε_r) for SLG and BLG on various substrates.

The real part (ε_r') for bare glass has been found in 5.17 – 5.30 range and imaginary part was in the range of 0.0001- 0.01. These values are in good agreement with the Corning glass substrate of $\varepsilon_r = 5.27 - 0.009\hat{\imath}$, which is provided in manufacturer's specifications. This agreement validates our adopted evaluation process to obtain the complex relative permittivity. **Fig. 5.2(a)** shows that the real part (ε_r') of SLG/glass and SLG/quartz decreases from 7.62 @ 10 MHz to ~ 6.71 @ 1.92 GHz and remains stable at ~ 6.80 for frequencies above 5 GHz, whereas the imaginary part (ε_r'') decreases from ~ 9.58 @ 10 MHz to 8.47 @ 1.92 GHz. In both the parts of ε_r,slightly higher variation for SLG/glass than SLG/quartz were observed over most of the frequencies as in the insets of **Fig. 5.2(a-b)**, which may be due to strong van der Waals forces between SLG/quartz than that in SLG/glass.For both BLG/Cu$_1$ and BLG/Cu$_2$, same values of ε_r' and ε_r'' are obtained in the range of 5.58 – 5.67 and 6.97 – 7.025, respectively. These both parts become constant to values ~5.60 and ~7.02, respectively for the frequency greater than 2 GHz. Insignificant variations in ε_r' and ε_r'' with

frequency have been observed for BLG/Cu$_1$ and BLG/Cu$_2$as illustrated in the insets of **Fig. 5.2(a-b)**. Our results pointed out that BLG synthesized by HFCVD can have nearly constant ε_r' and it can absorb almost same amount of microwave energy as by SLG, whereas difference in ε_r'', suggests that BLG will have less dissipation in the form of heat than SLG in addition to frequency independent behaviour. This nature of BLG can be used as a high power microwave absorber and also for broadband substrate material for planar microwave passive components with constant properties with frequency. We fabricated microstrip line on FR-4 substrate, which is DURAVER®-E-Cu quality 104 and has very low profile Cu foil with a surface roughness of about 0.6 μm. We estimated that this roughness may affect the relative permittivity of studied materials only up to 3% in 10 MHz to 26.5 GHz [7].

5.3.2 Complex refractive index

The obtained optical properties of graphene films (n,κ) with frequency are shown in **Fig. 5.3.**
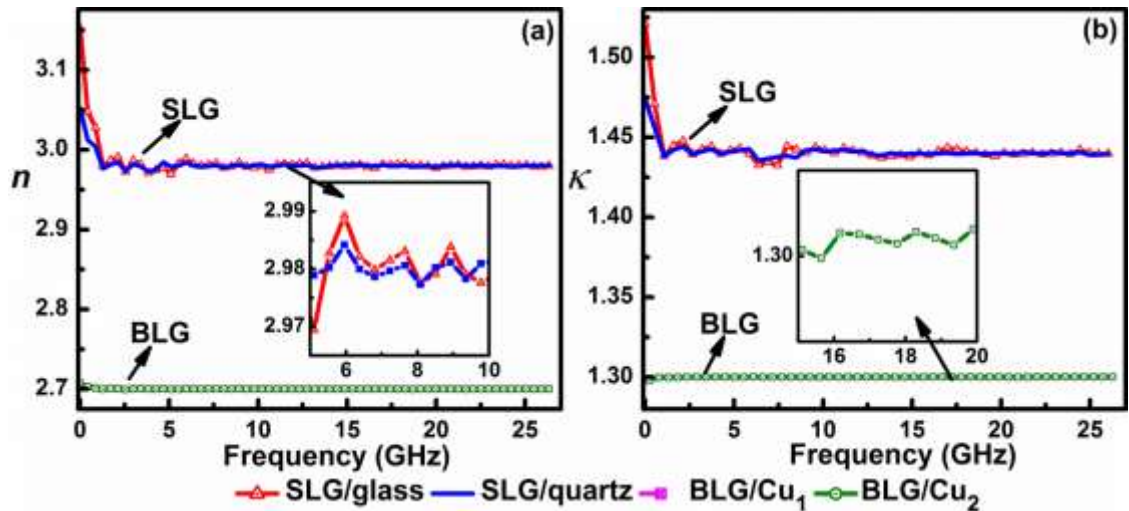
Fig. 5.3 (a) Refraction coefficient (n) and (b) extinction coefficient (κ) of SLG and BLG on various substrates.

With frequency, the refractive index (n) of SLG decreased from 3.15 @ 10 MHz to 2.95 @ 6.5 GHz and remains near this value with minor variations as shown in **Fig. 5.3(a)**, whereas in **Fig. 5.3(b)**, value of extinction coefficient (κ) for SLG is slightly decreased from 1.52 to 1.43. Compared to SLG/glass, these values are slightly lower in SLG/quartz, which is similar to differences in their surface interactions. Instead, in both samples BLG/Cu$_1$ and BLG/Cu$_2$, same values of n and κ were obtained and these are ~2.69 and ~ 1.28, respectively. Thus, SLG is found to be more dispersive than BLG at frequency below 1 GHz.

5.4 Behaviour of waves in single layer and bilayer graphene

5.4.1 Phase velocity and group velocity

The phase velocity and group velocity are obtained for each graphene film in the frequency range from 10 MHz to 26.5 GHz and the results are shown in **Fig. 5.4**.
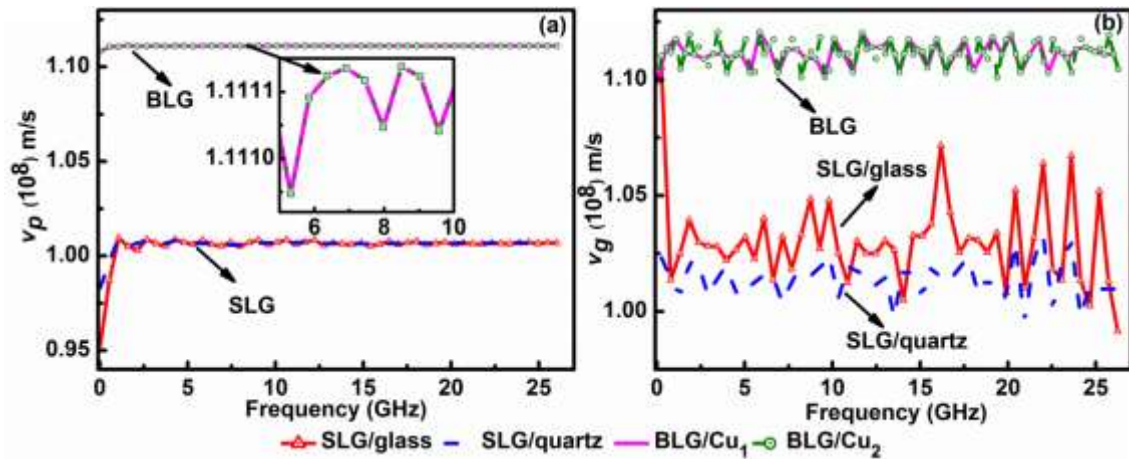
Fig. 5.4 (a)Phase velocity v_p(m/s)and (b)groupvelocity v_g (m/s) in SLG and BLG on various substrates.

As the frequency increased, the phase velocities in SLG also slightly increases from 0.95×10^8 m/s @ 10 MHz to 1.04×10^8 m/s @ 1.2 GHz and then remains at

$\approx 10^8$ m/sat highfrequency with insignificant variations. As shown in the inset of **Fig. 5.4(a)**, the phase velocity in BLG, is found to be almost constant with frequency and it is near $\sim 1.11 \times 10^8$ m/s. High v_p in BLG than in SLG/glass or SLG/quartzindicates somewhat faster propagation of waves. In addition, it is also suggesting that the waves propagate faster with increasing number of graphene layers and with almost constant velocity at higher frequencies. **Fig. 5.5(b)** shows that group velocity (v_g) has been reduced from $\sim 1.11 \times 10^8$ m/s @ 10 MHz to 1.02×10^8 m/s @ 1.1 GHz for SLG/glass, and then it varies significantly within 4% till 26.5 GHz, whereas for SLG/quartz, v_g has nominal variations with frequency. At certain frequencies, peaks and falls were observed in v_g for SLG. In BLG, higher v_g is found to be around 1.11×10^8 m/s, which represents faster propagation of microwave energy in BLG. In addition, v_g has been foundto be slightly higher than v_p at most of frequencies for SLG, it indicates that SLG may have little anomalous dispersive behaviour than BLG. In BLG, a linear dispersion is possible as v_p and v_g have similar range of values. We estimated that this may be due to lower inter-electron and electron-photon interactions in the measured frequency range in BLG **[8]**.

5.4.2 Optical effective mass of photons

We have presumed that in 2D graphene $v_g \approx v_f \approx v_p$ exhibits and photons can propagate with the velocity same as v_g in graphene and have effective mass m_{op}^***[9,10]**.Here, optical effective mass m_{op}^* for SLG and BLG are obtained from the group velocity and is normalized with the free electron mass,$m_0 = 9.107 \times 10^{-31}$ kg and shown in **Fig. 5.5(a-d)**.
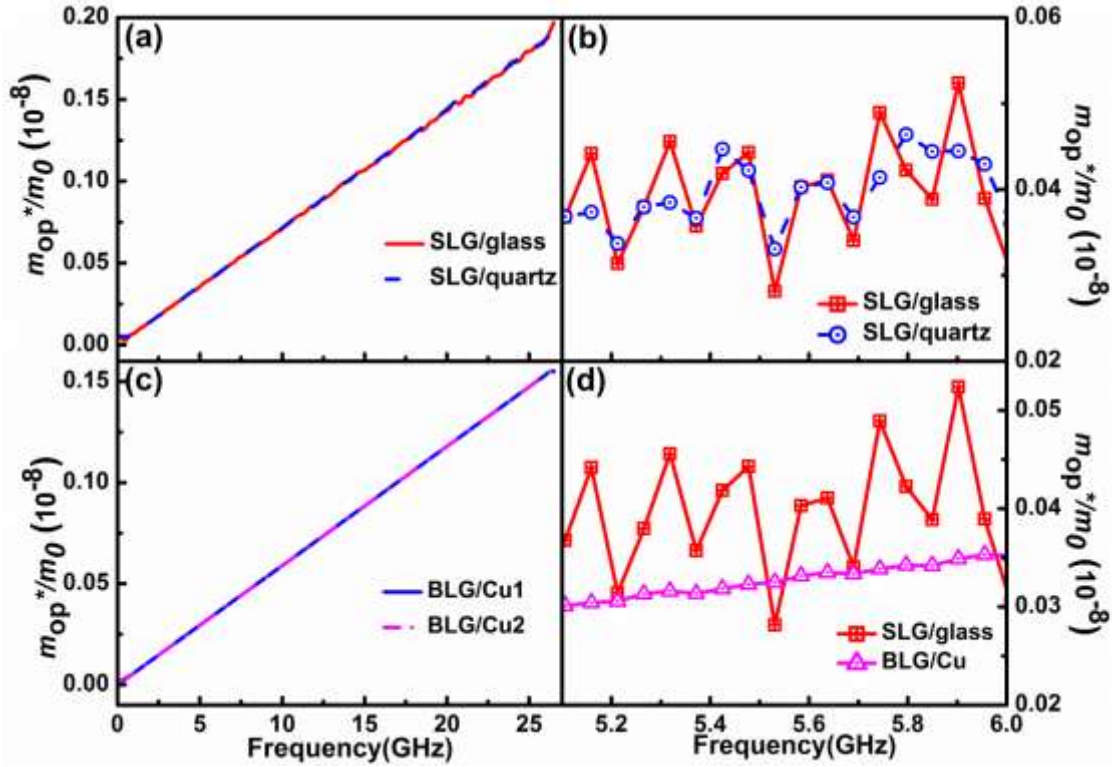
Fig.5.5 Variation of optical effective mass m_{op}^*/m_0 in SLG and BLG on various substrates.

The mass ratio $\left(m_{op}^*/m_0\right)$ is started from a value around $\sim 10^{-10}$ @ 10 MHz and increases linearly to $\sim 0.2 \times 10^{-8}$ @ 26.5 GHz and $\sim 0.16 \times 10^{-8}$ @ 26.5 GHz, respectively for SLG and BLG. With frequency, the behaviour of m_{op}^* depends the wave vector (k), as k is directly proportional to frequency, even group velocity (v_g) has little frequency dependence behaviour as shown in **Fig. 5.5(b)**. In **Fig. 5.5(a & c)**, the obtained m_{op}^* appears to have same values irrespective of the substrate (glass or quartz) for SLG or synthesis parameters for BLG. To further verify it, we plotted the mass ratio in limited frequency band, 5 to 6 GHz and it was observed in **Fig. 5.5(b)** that m_{op}^* in SLG/glass has significant variations than that in SLG/quartz as well as in BLG/Cu (**Fig. 5.5d**). Thus, it can be said that insignificant variations in m_{op}^* would make BLG as a

good candidate for the substrate material in the microwave components. As the properties discussed here for BLG are frequency independent in large frequency range, it can be utilized in broadband frequency applications. Such information on BLG provided by our investigation will help in the future study for effective utilization of graphene in microwave passive components.

5.5 Summary

Transmission, dielectric and optical properties of SLG transferred on glass and quartz substrates, and bilayer graphene as-grown on Cu foil have been analyzed and compared in frequency range of 10 MHz to 26.5 GHz. S-parameter measurements have been performed in microstrip line based measurement fixture and real and imaginary parts of complex relative permittivity have been obtained, which confirmed that BLG is a better dielectric material than the SLG as it dissipates less microwave energy. Furthermore, the refractive index in single layer and bilayer graphene were found to be higher at lower frequency below 1.5 GHz, which is used to estimate the phase velocity in the graphene samples. The phase velocities are found to be $\sim 1.04 \times 10^8$ m/s and $\sim 1.11 \times 10^8$ m/s in single and bilayer graphene, respectively, whereas little high group velocities are found in range of 2 to 26.5 GHz. In BLG, high phase velocity and group velocity represent faster propagation of energy and their relation suggests the linear dispersion. We experimentally determined the optical effective mass of photon in these graphene samples. In single and bilayer graphene, the optical effective mass has been found to vary from $\sim 0.72 \times 10^{-10} \; m_0$ to $\sim 0.2 \times 10^{-8} m_0$ in a frequency range between 1 GHz and 26.5 GHz. Lower effective mass of photons in BLG resulted owing to smaller refractive index, which in turn suggests minor interaction between photon-charge

carriers. The present study would help to utilize the graphene in the microwave passive and reciprocal components as a substrate material in broad frequency range.

On context to graphene properties reported earlier **[3]**, this chapter has presented the dielectric and optical properties of SLG and BLG in a broad frequency range of 10 MHz to 26.5 GHz. As BLG has shown encouraging dielectric properties due to less dispersion, the microwave passive devices reported in section 2.3 of chapter 2 will perform better if developed by utilizing bilayer graphene. Earlier, the complex refractive index was reported for CVD graphene using non-destructive method such as broadband spectrophotometery **[11]** and spectroscopic ellipsometry **[12]** in $300 - 1000$ nm wavelengths. In the work presented here, we have determined n and κ in the microwave frequency range in order to understand dispersion more specifically. The methods described to accomplish these properties are practical, simple and scalable since sample holder (microstrip line) involves simple planar geometries. Since only effective electron mass (m_e^*) was reported to be $0.012 m_0$**[13]** and $0.041 m_0$**[14]** in SLG and BLG, respectively, optical effective mass of photons was required to understand the behaviour of microwaves inside the SLG and BLG. By utilizing the energy dispersion relationship proposed for graphene **[9-10]**, we considered, $v_g \approx v_f \approx v_p$ is exhibited in 2D graphene and photons can have effective mass m_{op}^*. This effective mass was found to change insignificantly with the frequency.

References

[1] D. M. Pozar, *Microwave Engineering*, 4th ed, John Wiley & Sons, Inc., USA, 2012, pp.147.

[2] A. Koul, P. K. R. Anmula, M. Y. Koledintseva, J. L. Drewniak, S. Hinaga, Improved technique for extracting parameters of low-loss dielectrics on printed

circuit boards, in Proceedings of IEEE EMC Symposium, Austin, USA, 2009, p.191-196.

[3] Y. Wu, Y. Xu, Z. Wang, C. Xu, Z. Tang, Y. Chen, R. Xu, Microwave transmission properties of chemical vapor deposition graphene, Appl Phys Lett 101(5) (2012) 053110.

[4] J. Svačina, Analysis of multilayer microstrip lines by a conformal mapping method, IEEE Trans. Microwave Theory Tech. 40 (4) (1992) 769-772.

[5] J. Svačina, A simple quasistatic determination of basic parameters of multilayer microstrip and coplanar waveguide, IEEE Microwave Guided Wave Lett. 2(10) (1992) 385-387.

[6] C. Wan and A. Hoorfar, Improved Design Equations for Multilayer Microstrip Lines, IEEE Microwave Guided Wave Lett. 10 (6) (2000) 223-224.

[7] A. F. Horn, J. W. Reynolds and J. C. Rautio, Conductor profile effects on the propagation constant of microstrip transmission lines, in Proceedings of IEEE MTT-S International Microwave Symposium, Anaheim, CA, 2010, p. 868-871.

[8] Z. Z. Alisultanova and R. P. Meilanov, On the theory describing graphene in an anomalous-dispersion region, J. Surface Investigation. X-ray, Synchrotron and Neutron Techniques 7(1) (2013) 46–50.

[9] V. Ariel, Effective mass and energy-mass relationship, 2012, e-print arXiv:1205.3995.

[10] V. Ariel and A. Natan, Electron Effective Mass in Graphene, e-print arXiv:1206.6100v2 [physics.gen-ph], (2012)].

[11] A. Gray, M. Balooch, S. Allegret, S. D. Gendt, and W. E. Wang, Optical detection and characterization of graphene by broadband spectrophotometry, J. Appl. Phys. 104 (2008) 053109.

[12] F. J. Nelson, V. K. Kamineni, T. Zhang, E. S. Comfort, J. U. Lee and A. C. Diebold, Optical properties of large-area polycrystalline chemical vapor deposited graphene by spectroscopic ellipsometry, Appl. Phys. Lett. 97 (2010) 253110.

[13] E. Tiras, S. Ardali, T. Tiras, E. Arslan, S. Cakmakyapan, O. Kazar, *et al.* Effective mass of electron in monolayer graphene: Electron-phonon interaction, J. Appl. Phys. 113 (2013) 43708.

[14] K. Zou, X. Hong, and J. Zhu, Effective mass of electrons and holes in bilayer graphene: electron-hole asymmetry and electron-electron interaction, Phys. Rev. B 84 (2011) 085408.

Chapter 6

Application of p-type graphene as a transparent conducting electrode

6.1. Introduction

In this chapter, simulation of p-graphene/n-crystalline silicon heterojunction solar cell configured as TCO (ITO)/p-Gr/n-cSi/Ag structure using AFORS-HET software under the illumination conditions of AM1.5G had been carried out. Details of simulation parameters for graphene and silicon layers as well as front and back contacts are given. The effects of parameter changes on cell parameters are discussed for each layer. After optimizing first the graphene layer, the parameters of silicon layer has been varied and effects are discussed. For best cell, spectral response and quantum efficiency are also described in addition to the analysis of temperature dependence of such high efficiency cell. The presented results in this chapter have been published in **Kamlesh Patel and Pawan K. Tyagi, Carbon 116 (2017) 744-752**, http://dx.doi.org/10.1016/ j.carbon.2017.02.042.

6.2.   p-graphene/nc-Si solar cell structure

In graphene, Fermi Level in graphene is always either remained in the conduction or in the valence band due to gapless or small bandgap. This makes graphene to behave differently than others 2D semiconducting materials and it becomes insulating if Fermi level enters the bandgap.Giannazzo *et al.* 2011 reported that2D semiconductor systems exhibit bandgap of > 1 eV and such bandgap results in

completely different electron-doped or hole-doped structures [1]. In graphene, the nature of carrier changed at the Dirac point from electrons to holes (or vice versa) [1]. For understanding the carrier transport in single and multilayer graphene, a diffusion-drift theory has been developed [2]. A semiconductor system is known as ideal 2D system only if that system has one physical dimension in order of Fermi wavelength. Fermi wavelength is reported as $\lambda_F = \left(2 \times 10^7 \sqrt{\pi/n}\right)$ nm for graphene, where n is the sheet carrier density in cm^{-2} [1, 3]. It is also reported that if n approaches to $\sim 10^{15} \, cm^{-2}$, λ_F would be order of 1 nm [4]. Therefore, doped graphene as well as bilayer graphene cannot satisfy the condition $<t> \leq \lambda_F$, where $<t>$ is the average thickness for a 2D electron system. Furthermore, it was reported that if multilayer or single layer graphene is integrated with silicon wafer then 2D transport equation can be coupled with 3D equations [2]. Since in graphene/crystalline silicon heterojunction solar cell, sheet carrier density (n_{2D}) is in cm^{-2} and can be obtained in terms of doping concentration using relation $\sim 3.3 \times 10^{-8} \times N_A$, where N_A is doping concentration in cm^{-3}. Since, carrier density can be controlled by chemical doping, which can further influenced the work function as well as cell resistance. In addition, the work function changes with effective valence band density. So in gapless graphene, 2D carrier density and effective valance band density can be obtained by multiplying the film thickness with the bulk values.

In the present work, basic structure of p-graphene/n- crystalline silicon heterojunction solar cell was taken as TCO (ITO)/p-Gr/n-cSi/Ag and shown in **Fig. 6.1 (a)**. Here, transport of carrier has been made along c-axis of graphene. Hence, graphene is presumed as quasi 3D in nature in the simulated work. In this structure, a layer of SiO_2 is introduced to insulate the direct carrier transport through TCO (contact) to n-cSi layer so that transport will only be made through the graphene layer [5-6]. Here, ITO is

taken as TCO material and deposited on the top of graphene. Experimentally, ITO can be deposited by using electron beam and pulsed layer deposition (PLD) techniques directly on graphene transferred on SiO_2/Si pattern substrate [7-9] as these deposition techniques do not harm the graphene.
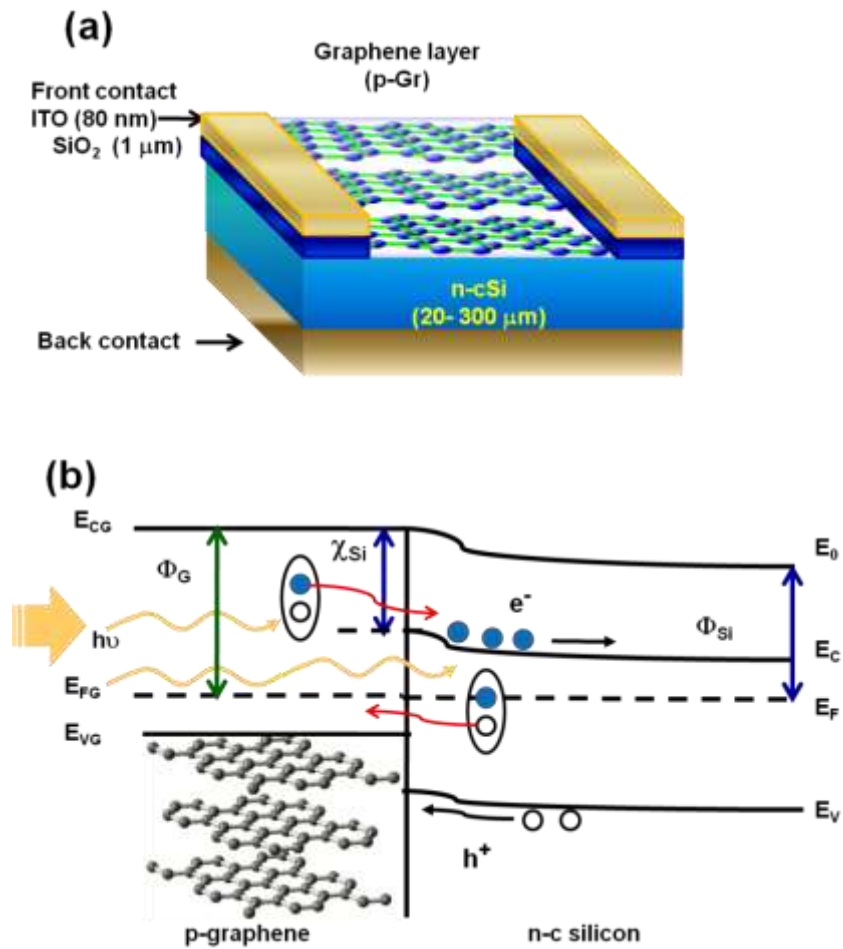
Fig. 6.1 Graphene/silicon heterojunction solar cell. (a) Schematic diagram of simulated structure, where ITO is on the top of graphene (b) Schematic diagram of p-type graphene/ n-c silicon interface, where Φ_G ,Φ_{Si} and χ_{Si} are the graphene work function, silicon work function, and the silicon electron affinity, respectively.

The illumination conditions were kept as the monochromatic intensity (photon flux) of 1×10^{16} cm^{-2}s^{-1} with 10 nm spectral width in the range of 300 – 1200 nm to simulate the quantum efficiency (QE).For the initial simulation study, thickness, refractive index (n) and extinction coefficient (k) of single layer graphene were taken as 0.334 nm, 2.7 and 1.45, respectively [10-11]. Then, six parameters of graphene were changed in the feasible ranges and these parameters were the acceptor concentration (N_A), bandgap (E_g), effective conduction and valance band densities (N_C/N_V), electron affinity (χ), relative permittivity (ε_r) and electron mobility (μ_n). Later, the simulation was performed for different layer numbers of graphene, where thickness was taken as a seventh parameter.

On achieving an efficiency around 6.75 % after optimizing the p-Gr layer, we switched to optimize the parameters of n-type crystalline silicon (n-cSi) like the donor concentration (N_D), effective conduction and valance band densities (N_C/N_V), the electron affinity (χ) and thickness for n-cSi layer. The parameters such as relative permittivity (ε_r), electron mobility (μ_n) and bandgap (E_g) of n-cSi were kept at their standard values as per the previous available reports [12-14]. The highest efficiency is achieved in single layer p-Gr/n-cSi heterojunction cell after the full optimization of the layer parameters of graphene as well as silicon layers.

As shown in **Fig. 6.1**(a), the graphene and semiconductor interface barrier is ideally Schottky in nature. In the p-Gr/n-cSi solar cell, a built-in voltage developed at the graphene/silicon (Gr/Si) interface due to recombination of the majority charge carriers. However, minority charge carriers, i.e. holes in the n-cSi layer, tend to move towards the p-type graphene layer and the energy levels bend upward near the Gr/Si interface [15].

This voltage (V_{BI}) is equal to the difference of the barrier height (Φ_{BI}) and energy gap (E_g) in the silicon. Also, the barrier height (Φ_{BI}) is defined as per the following equations [5],

$$\Phi_{BI} = \Phi_G - \Phi_{Si} \qquad (6.1)$$

$$\Phi_{Si,n} = \chi_{Si} + k_B T \ln \left({N_D}/{N_C} \right)_{Si} \qquad (6.2)$$

$$\Phi_{G,p} = \chi_G + k_B T \ln \left({N_A}/{N_V} \right)_G \qquad (6.3)$$

where Φ_G, χ_G, Φ_{Si}, and χ_{Si} are the graphene work function and affinity, the silicon work function and the silicon affinity, respectively, k_B ($= 1.38 \times 10^{-16}$ cm^2 kgs^{-1}) is the Boltzmann constant, T is a room temperature (300 K). Here N_D and N_C are the donor concentration and the effective conduction band density of the n-cSi in Eq. (6.2), respectively. In Eq. (6.3), N_A and N_V are the acceptor concentration and effective valence band density of the graphene layer, respectively.

As device was illuminated,first, electron and hole (e-h) pairs generated in the cell and then separated at the interface due to the built-in voltage. These newly generated minority carriers move towards the p-Gr and n-cSi regions, respectively, as shown in **Fig. 6.1(b)** [15]. These newly generated charge carriers enhance the carrier density in the respective regions and develop an open circuit voltage (V_{OC})when the cell is open circuited. At the time of short-circuiting, the excess charge carriers are collected at the contact electrodes, which resulted a short- circuit current (I_{SC}) flowing in the external circuit. The details of contacts including front as well as back have been

tabulated in Table 6.1. The values and ranges of various parameters are tabulated in Table 6.2.

Table 6.1: Details of the front and back contact parameters of the cell used for simulation.

Contact Parameters	Front contact	Back contact
Width (cm)	8×10^{-6}	0.001
File	ITO.nk	Ag.nk
Metal work function	Yes (flatband)	Yes (flatband)
Absorption loss	ITO.abs	0
External reflection constant	aSicSi_ITO.ref	0
Surface condition	Plane	Plane
Internal reflection constant	0	0

Table 6.2: The values and ranges of layerparameters taken for the simulation of the cell structure.

Input Parameters	p-Gr	n-cSi
Relative permittivity, ε_r	4 – 11	11.9
Electron mobility, μ_n (cm^2/V.s)	$1 - 1 \times 10^6$	1350
Hole mobility, μ_p (cm^2/V.s)	10	450
Electron Affinity, χ (eV)	4.7 – 5.0	3.6 – 4.4
Band gap, E_g (eV)	0 – 0.25	1.12
Acceptor concentration N_A(cm^{-3})	$1 \times 10^{14} - 1 \times 10^{18}$	0
Donor concentration N_D (cm^{-3})	0	$1 \times 10^{14} - 5 \times 10^{18}$
Effective conduction band density, N_C (cm^{-3})	3×10^{18} - 3×10^{21}	3×10^{19} - 6×10^{21}
Effective valance band density, N_V (cm^{-3})	3×10^{18} - 3×10^{21}	3×10^{19} - 6×10^{21}
Thermal velocity of electrons (cm/s)	1×10^7	1×10^7
Thermal velocity of holes (cm/s)	1×10^7	1×10^7
Layer density (g/cm)	2.328	2.328
Thickness (cm)	3.34×10^{-8} - 6.68×10^{-7}	$2 \times 10^{-3} - 3 \times 10^{-2}$
Mid bandgap density of states (cm^{-3}/eV)	-	Single acceptor
Switch-over energy (eV)	-	0.56
Auger recombination coefficient for electron (cm^6/s)	0	0
Auger recombination coefficient for hole (cm^6/s)	0	0
Direct band-to-band recombination coefficient (cm^3/s)	0	0
Optical properties	n = 2.7, k = 1.45	cSi.nk

6.3 Optimization of p-graphene layer

We started our simulation with the optimization of accepter concentration (N_A) of graphene layer while some significant values were assigned to other parameters [4-5, 16-17].The effective conduction and valance band densities (N_C and N_V) were kept to 3×10^{18} cm^{-3} for single layer graphene, which has been estimated from the effective electron mass, $m_e^* = 0.012\, m_0$ [18] and the effective hole mass $m_h^* = 0.0105\, m_0$[19], where free electron mass is $m_0 = 9.1 \times 10^{-31}$Kg. These densities are calculated on taking the account of doping influenced by quantum confinement effect, $N_C^{3D} = N_C^{2D} . t$, where t is thickness of graphene layer and $N_C^{2D} = 4\pi\, m_e^* k_B\, T/h$, here h (= 6.62×10^{-27} cm^2 kg/s) is a Planck's constant. Dependence of cell performance on $N_A$has been shown in **Fig. 6.2 (a-b)**. After doping with AuCl$_3$, Φ_G was increasedfrom 4.7 eV to 5.1 eV and this shift was significantly found to decrease the sheet resistance (R_{sh}) [5].Consequently, as N_A increases, the short-circuit current density (J_{SC}) reduced infinitesimally from 18.19 mA/cm^2 to 18.01 mA/cm^2 until $N_A$reach to 10^{18} cm^{-3}. After $N_A \approx 10^{17}$ cm^{-3} in p-Gr, the photo-generated electrons moved easily from the graphene layer to n-cSi with high mobility, and increased V_{OC} up to 124.2 mV. Above $N_A > 10^{16}$ cm^{-3}, a little decrement in FF was observed that might be due to the increase of R_{sh} caused by heavy doping. We noticed that FF was improved after $N_A > 10^{17}$ cm^{-3}, efficiency (η) increased up to 0.95%. This might have happened due to increase in Φ_G, which enhances effective Φ_{BI} andreducesR_{sh}. During this process, V_{OC} was seen to remain constant and increased only after $N_A > 10^{17}$ cm^{-3}. At $N_A > 10^{18}$ cm^{-3},efficiency (η) and fill factor (FF) reached to highest values.
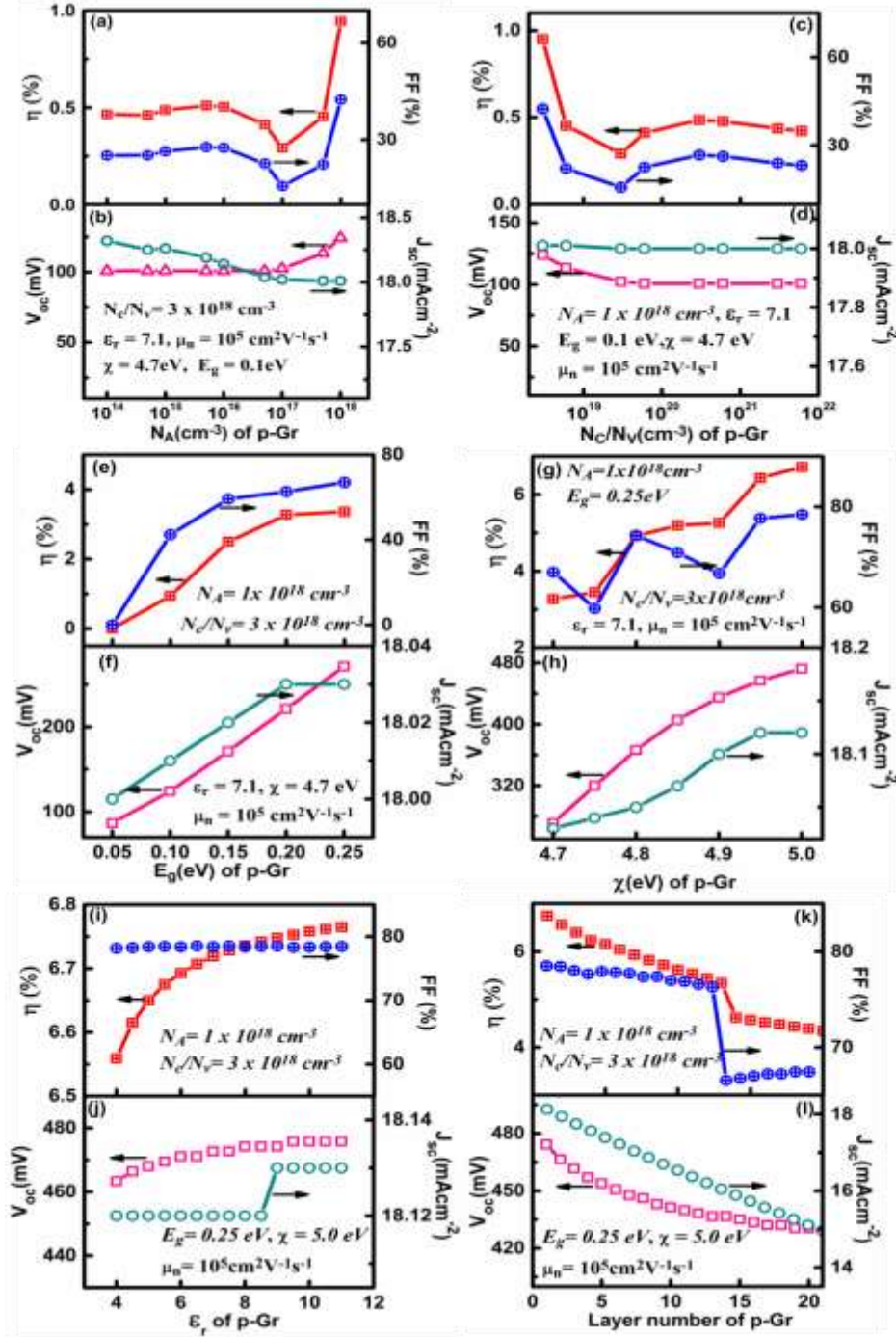
Fig. 6.2. Schematic representation of cell performance with the optimization of the parameters of p-graphene layer, (a-b) the acceptor concentration N_A (cm^{-3}), (c-d) the effective band density N_C/N_V (cm^{-3}), (e-f) the bandgap energy E_g (eV), (g-h) the electron affinity χ (eV), (i-j) the relative permittivity ε_r, and (k-l) layer number. The parameters of n-cSi were kept as, the donor concentration $N_D = 1 \times 10^{16}$ cm^{-3}, the effective band density $N_C/N_V = 3 \times 10^{19}$ cm^{-3}, the electron affinity $\chi = 4.05$ eV and thickness 100 μm. The other parameters of silicon as well as p-type graphene are given in Table 6.2.

After optimizing N_A to 10^{18} cm^{-3}, parameter N_C/N_V was varied in 3×10^{18} cm^{-3} to 6×10^{21} cm^{-3} range for single layer graphene. As N_C/N_V is increased from 3×10^{18} cm^{-3}, minority carrier concentrations were found to be reduced, which may have happened probably due to the lower lifetime of photo-generated carriers and trapping of charge carriers. Consequently, J_{SC} was constant to 18 mA/cm^2 at 3×10^{19} cm^{-3} to 6×10^{21} cm^{-3}. In **Fig. 6.2 (c-d)**, V_{OC} is found to reduce sharply with increase of N_C/N_V. As N_C/N_V increases, significant reduction in barrier height (Φ_{BI}) was observed accordingto Eq. (6.4) and Eq. (6.5). Thisresulted in shortage of charge carriers near the junction and the minor built-in voltage lowered V_{OC}. Effectively, η dropped to a minimum of $\sim 0.3\%$ at 3×10^{19} cm^{-3} of N_C/N_V. Reducing N_C/N_V to 3×10^{18} cm^{-3} results transport of free charge carriers to contacts through the respective regions and to maintain higher charge carrier separation near the junction. These all processes helped to keep V_{OC} and J_{SC} to maximum value on lowering N_C/N_V down to 3×10^{18} cm^{-3}.

After optimizing N_A and N_C/N_V to 10^{18} cm^{-3} and 3×10^{18} cm^{-3}, respectively, the bandgap energy (E_g) of the p-Gr has been varied from 0 eV to 0.25 eV. As E_g increases, V_{OC} was enhanced as built-in voltage is increased and J_{SC} linearly was improved as high barrier voltage separates more photo-generated carriers to cross the p-Gr/n-cSi junction, which is shown in **Fig. 6.2(e-f)**. As the fill factor inversely depends on the effective resistance to the charge carriers in p-Gr layer, higher J_{SC} and FF increased η from 0.95 % (@ E_g = 0.1 eV) to 3.28 % (@E_g = 0.25 eV). Simulation response of the electron affinity (χ) is shown in **Fig. 6.2(g-h)**. After the initial value of χ = 4.7 eV, η decreased slightly while J_{SC} and FF increased significantly, and V_{OC} was further improved to the maximum value at χ = 5.0 eV. This may have happened on increasing χ above 4.7 eV, the barrier height increases and probably enhances the transfer of minority charge

carriers, which results in raising J_{SC}. Thus, η almost linearly increased with higher values of χ in a p-Gr layer and for χ = 5.0 eV, we obtained $\eta \sim$ 6.75 %. The relative permittivity (ε_r) for a single layer graphene was reported to be 7.1 $\pm$ 3.2 at 540 nm [20], so we have varied this parameter from 4 to 11 and the cell performances are shown in **Fig. 6.2(i-j)**. The open-circuit voltage (V_{OC}) is found to be increased for low ε_r values from 4 to 6, and then become almost constant with further increase in ε_r. Also FF is found to have infinitesimally increased to 78.45 % at $\varepsilon_r \approx$ 11, whereas J_{SC} remained constant, $\eta \sim$ 6.765 % was achieved. On simulation by varying the electron mobility (μ_n) of the p-Gr layer, the cell responses remained constant due to very thin layer.

To observe the effect of p-Gr thickness on the carrier generation due to the photon absorption, the cell with optimized single layer graphene was simulated up to 20 layers of graphene. The layer numbers was reported to control the transmittance as well as the sheet resistance of the graphene [5]. On increasing the layer number, sheet resistance decreased and η was enhanced, however, this enhancement has been compensated by equal and opposite reduction in the transmittance of p-Gr, which reduces η. Single layer graphene is reported to absorb the incident light by amount of 2.3 % [20]. In our simulated work, the cell parameters were found to reduce linearly up to 13 layers of p-Gr and then FF sudden dropped on its 14th layer, so η also sharply dipped and reached to 4.57 % as shown in **Fig. 6.2(k-l)**. This sudden fall in FF may be indicating that the sheet resistance becomes constant for this thickness of graphene layer and as the layer number becomes larger, FF increased only infinitesimally [5]. The efficiency of 4.34 % was achieved for 20 layers of p-graphene. Therefore, the thickness of p-Gr degrades the cell parameters. We found that the p-graphene layer with

optimized parameters provides a Schottky junction for the current movement as well as plays a role of transparent conducting electrode (TCE).

6.4   Optimization of n-cSi layer

In order to enhance efficiency of the p-Gr/n-cSi heterojunction cell further, we focused on the simulation of the parameters of n-cSi layer. When the donor concentration (N_D) in n-cSi layer was increased from 10^{14} cm^{-3}, the silicon work function (Φ_{SI}) is increased in accordance to Eq. (6.2) which leads to an increase in the open circuit voltage (V_{OC}) as shown in **Fig. 6.3(a-b)**. This suggests that the built-in voltage (V_{BI}) has been increased due to the high barrier height (Φ_{BI}) after doping and the reduction in the depletion region led to higher J_{SC} with initial constant value. For $N_D > 10^{17}$ cm^{-3}, V_{OC} starts reducing while J_{SC} is continued to be increasing, probably due to additional minority carrier generation as total carrier density has been enhanced with doping. However, as a consequence of higher defect density proportional to heavy doping, FF is found to be reduced after $N_D \approx 10^{18}$ cm^{-3} **[12]**. The maximum η of ~ 8.61 % is achieved at $N_D \approx 5 \times 10^{18}$ cm^{-3}.

The second parameter N_C/N_V has been varied in the range of 3×10^{19} to 6×10^{21} cm^{-3} in n-cSi layer and subsequent effects on cell parameters are presented in **Fig. 6.3 (c-d)**. V_{OC} is found to be decreased, while J_{SC} increased only infinitesimally with the variation in N_C/N_V. A variation in V_{OC} kept FF to be changed accordingly with N_C/N_V upto 1×10^{21} cm^{-3}. Further increase in N_C/N_V values of n-cSi layer increased the short-interval states for charge carriers, so V_{OC} dropped significantly in the cell.
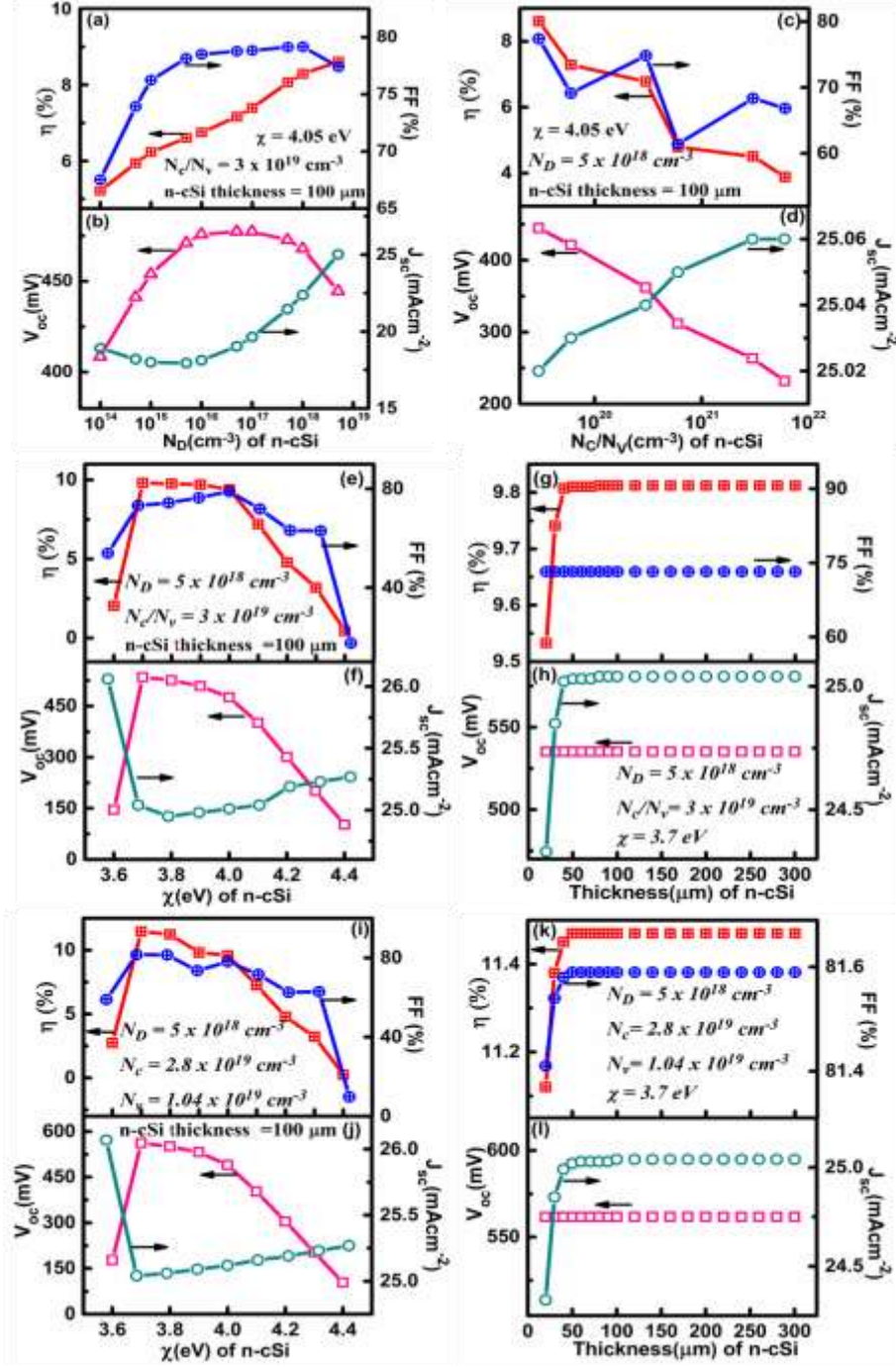
Fig. 6.3 Schematic representation of cell performance with the optimization of the parameters of n-cSi layer, (a-b) the donor concentration N_D (cm^{-3}), (c-d) the effective band density Nc/Nv (cm^{-3}), (e-f) the electron affinity χ (eV), (g-h) thickness (μm). At $N_D = 5 \times 10^{18}$ cm^{-3}, Nc = 2.8×10^{19} cm^{-3} and Nv = 1.04×10^{19} cm^{-3} for n-cSi, (i-j) the electron affinity χ (eV) and (k-l) thickness (μm). The optimized parameters of p-Gr were $N_A = 1 \times 10^{18}$ cm^{-3}, $N_C/N_V = 3 \times 10^{18}$ cm^{-3}, $E_g = 0.25$ eV, $\chi = 5.0$ eV, $\varepsilon_r = 9$, $\mu_n = 10^5$ cm^{2}V^{-1}s^{-1}.

The efficiency (η) reduced to 3.89 % at Nc/Nv ≈ 6×10^{21} cm^{-3} in proportion to V_{OC} drop. Thus, the higher band density in thick n-cSi layer intends to decrease the silicon work function (Φ_{SI}) with constant χ as per Eq. (6.2) and eventually lowers Φ_{BI}. Thus a drop in built-in voltage V_{BI} and V_{OC} was observed with high Nc/Nv. After optimizing the n-cSi layer for $N_D \approx 5 \times 10^{18}$ cm^{-3} and $N_C/N_V \approx 3 \times 10^{19}$ cm^{-3}, the electron affinity χ in eV was varied in the range from 3.6 to 4.4. In this range, initially V_{OC} was found to be increased and then reduced from 535.2 to 102.3 mV, whereas J_{SC} was increased to 25.27 mA/cm^2 from 25.01 mA/cm^2 at χ = 4.4 eV as shown in **Fig. 6.3(e-f)**. At χ = 3.7 eV, the maximum efficiency of 9.812 %. was attained. For χ> 3.8 eV, V_{OC} was found to be decreased and J_{SC} was increased slightly till χ = 4.4 eV. These variations in two parameters indicated the significant modification in the work function of n-cSi layer, which leads to reduction in the rate of carrier transport through n-cSi layer. Consequently, this reduction increases the series resistance of n-cSi layer as well as of cell and so, the fill factor (FF) also significantly reduces and η falls to zero after χ> 4.4 eV.

In order to explore the possibility of solar cell with minimum cost, we have studied cell performance with the thickness of n-cSi as the next parameter to vary from 20 μm to 300 μm. **Fig. 6.3(g-h)** shows that for 20 μm thick n-cSi layer, η was achieved to be 9.533 %. Highest efficiency 9.812 % was found for 80 μm thickness. The larger thickness significantly increases the number of charge carriers and so J_{SC} becomes higher. In thicker n-cSi layer, the lifetimes of minority charge carriers i.e. holes reduced due to less drift length. In addition, the recombination rate must have been in proportion with excess photo-generated charge carriers in the thick silicon layer > 100 μm, these

two processes compensated each other and led to constant V_{OC} and J_{SC}. So η of 9.812 % was achieved due to saturated V_{OC} and J_{SC} even for the thickness up to 300 μm.

A maximum efficiency of 9.812 % does not seem tobe practically feasible for a single layer p-Gr/n-cSi solar cell made on 100 μm silicon substrate, as in the present simulation the optical and electrical losses at the interface and contacts were not considered. In order to have a better practical possibility, we have simulated the electron affinity (χ) and thickness of n-cSi layer with the reported experimental values for Si such as $N_D \approx 5 \times 10^{18}$ cm^{-3}, $N_C \approx 2.8 \times 10^{19}$ cm^{-3}, $N_V \approx 1.04 \times 10^{19}$ cm^{-3}[21]. With these values, **Fig. 6.3(i-j)** shows the simulated responses of cell parameters with χ (eV), which are found to be almost similar to those reported in **Fig. 6.3(e-f)**. A maximum efficiency of 11.47 % has only been found at $\chi = 3.7$ eV of Si. The short-circuit current density J_{SC} has shown only a little increase with large variation in χ, whereas V_{OC} was decreased for large χ from 3.9 to 4.5 eV. However, a reduction in FF noticed at higher χ values, compels η to be drop to 0.256 % at $\chi = 4.4$ eV. The thickness of n-cSi has been varied with the new values of N_D, N_C/N_V and $\chi = 3.7$ eV as similar to **Fig. 6.3(g-h)**. The patterns of cell parameters have revealed significant changes in lower thickness range as shown in **Fig. 6.3(k-l)**. For thickness greater than 50 μm, the high rate of carrier recombination kept V_{OC} and J_{SC} to constant value inside the thick n-cSi layer. With thickness, the effective series resistance of the cell seems to be constant as the total cell area is increased, and fill factor remained independent of silicon layer thickness. These constant cell parameters led to the efficiency of 11.47 % irrespective of increase in the layer thickness.

In order to validate the feasibility of results, we have compared the simulated results with experimentally reported and found that our results are much convincing.

Recently, it was reported that with varying the doping concentration in multilayer graphene (MLG)of 4-7 layers, efficiency in MLG/Si heterojunction cell was found between 5.52 to 9.27% [22].In our case, this simulated value was nearly 6 %. Our simulated efficiency 6.75 % with optimized single layer graphene was found near to match with the experimentally reported efficiency of 8.6 % [6] and 7.7 % [5]. In their reports, they have used the commercial n-type silicon with doping concentration in the range of 8×10^{14} to 1×10^{15} cm^{-3}. Experimentally also the maximum efficiency of 6 % was reported for optimized p-type graphene [5], which matches with our simulated results 5.22 % and 6.43 % for doped n-type Si of $N_D\approx1\times10^{14}$ cm^{-3} and 1×10^{15} cm^{-3}, respectively as shown in **Fig. 6.3(a-b)**. Later, we have also simulated the cell performance with the different front contact like Au (n=0.27049, k=2.7789), Ti (n=1.96, k=3.06), Ag (the related file is present in AFORS-HET); however, no significant change in cell performance was noticed. Earlier, other metal as front contact have been used in practically made graphene/silicon cells like Ti/Au, Au, Ag, Au/Cr [5-6, 22-26]. In our simulation work, we preferred TCO as front contact to improve the effective illumination area, which has high optical absorption than providing reflection whereas other metal contact may provide reflection too.

6.5 Spectral response, quantum efficiency and temperature dependence

The spectral response (SR) is a ratio of current produced by the solar cell to the optical power incident on the solar cell [27] and shown for the optimized cell efficiencies of 6.75 %, 9.81%, 9.812 % and 11.47 % in **Fig. 6.4(a)**. The graphene layer exhibits more absorption in the wavelength range below 600 nm and allows less

numbers of photon reach to n-cSi layer and subsequently low photocurrent generation. As with optimized parameters, most photons in the range from 600 to 1000 nm have reached to Si layer, their energy is matched with silicon bandgap energy and effectively converted into electrical energy inside Si. So, only efficiency of 6.75 % was achieved by tuning the properties of graphene layer properly. As doping concentrations in the layers increase, the SR enhances with higher J_{SC} due to high carrier generation.
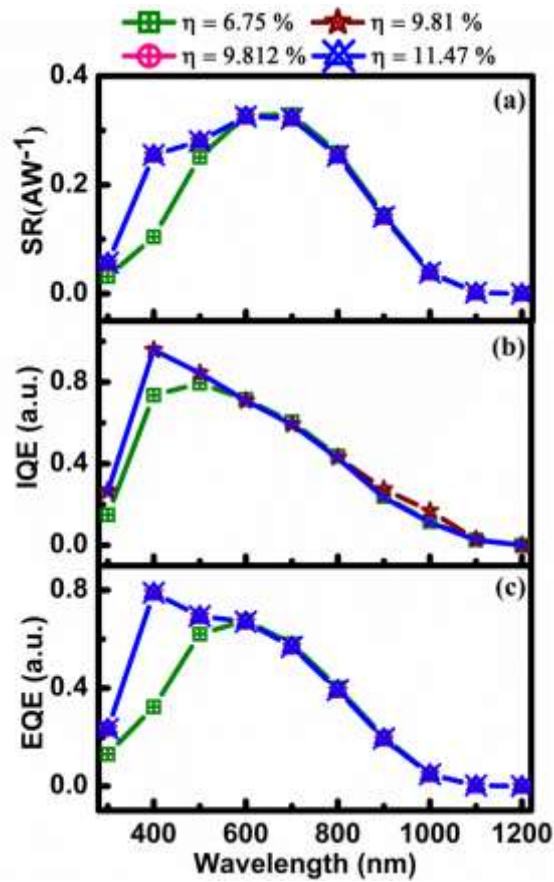
Fig. 6.4(a) Spectral response (SR), (b) Internal quantum efficiency (IQE), and (c) External quantum efficiency (EQE) of best optimized single layer p-Gr/n-cSi cells (η = 6.75 %, η = 9.81 % and η = 9.812 % with $N_D = 5 \times 10^{18}$ cm^{-3} and $N_C/N_V = 3 \times 10^{19}$ cm^{-3} for 50 μm and 100 μm n-cSi, respectively, η = 11.47 % with $N_D = 5 \times 10^{18}$ cm^{-3}, N_C = 2.8×10^{19} cm^{-3} and $N_C = 1.04 \times 10^{19}$ cm^{-3} for 100 μm n-cSi).

With the optimization of silicon layer, the absorption of the photons is increased in the shorter wavelengths (300 nm to 600 nm) and the efficiency is reached to 9.812 % and 11.47 %, respectively for different values of N_D and N_C/N_V in 100 μm Si. As the silicon is an indirect bandgap semiconductor, the SR is approaching to zero with the longer wavelength where photons have less energy than its bandgap ($E_g = 1.12$ eV). For silicon layer > 50 μm ($\eta \approx 9.81$ %), the effective carrier generation rate is same and therefore, the SR remains constant even on increasing the thickness upto 300 μm.

The internal quantum efficiency (IQE) of cell has enhanced at the shorter wavelengths (< 500 nm) after optimizing the parameters of silicon layer as shown in **Fig. 6.4 (b)**. The optical losses may be dominant at the shorter wavelengths for graphene optimized cell as suggested by the external quantum efficiency (EQE) response in **Fig. 6.4(c)**. With the optimization of graphene and silicon layers, both reflection and transmission losses of the cells are reduced. Therefore, higher EQE is obtained for the wavelengths in the range from 400 nm to 600 nm. Higher EQE also revealed that optimization of doping concentration and effective band density significantly increases the electron-hole pair generation and subsequent collections of excess charge carriers in the cell, and so high efficiency has been achieved **[6]**. The IQE and EQE responses of all three cells with efficiencies ~ 9.81 %, 9.812 % and 11.47 % are found to be almost same, indicating that same number of charge carriers have been collected against the photons absorbed into the cells except IQE in the range 800 to 1100 nm. For longer wavelengths, less collections of photogenerated charge carriers led reduction of IQE and EQE to zero.
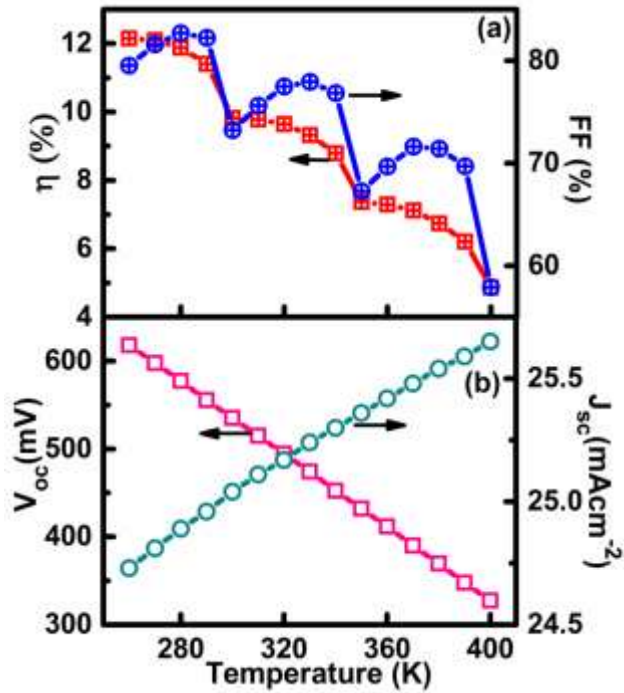
Fig. 6.5 Dependence of cell response for the cell with η = 9.812 % (a) efficiency and fill factor, and (b) V_{OC} and J_{SC} with temperature variation.

We have then studied the cell response against temperature variation and the results are shown in **Fig. 6.5 (a-b)**. As temperature is raised from 300 K (RT), band bending is found to be reduced at graphene/Si interface. The optical scattering by phonons in graphene layerhelps the electrons to move in the conduction band through the photoemission from the valance band[28]. Hence, the photo-generated electrons which are dense in the conduction band at the higher temperatures have enhanced J_{SC}. In a reverse way, when temperature decreases from RT, carrier generation rate reduced at the interface, which has resulted in lower J_{SC}. As high V_{OC} and FF were found, a higher efficiency of ∼ 12.15 % was achieved at 260 K. For silicon cells, it is reported that the reverse saturation current density (J_0) controls the effect of temperature on V_{OC}, FF and η. Also J_0 depends on the material and its bandgap (E_g), where exponential increase in

J_o with temperature decreases V_{OC} with a high rate, and so FF and η are reduced[29].

Fig. 6.5 represents the rate of change in V_{OC}, J_{SC}, FF and η with temperature and with linear fitting of data, these rates were found as, $dV_{OC}/dT \approx$ -2.07 mV K^{-1}, $dJ_{SC}/dT \approx$ 0.0065 $mAcm^{-2}$ K^{-1}, $dFF/dT \approx$ -0.124 % K^{-1} and $d\eta/dT \approx$ -0.051 % K^{-1}. The correlation of these cell parameters with temperature for our cell was found in good agreement with experimentally reported silicon based cells **[29]**. Optimized cell parameters have been presented in Table 6.3.

Table 6.3: Summary of the parameters of the best optimized graphene/silicon cells.

Cell parameters	p-Graphene layer optimized cell	p-Graphene layer and n-cSi layer optimized cell	
V_{OC} (mV)	476.4	535.2	561.7
J_{SC} ($mAcm^{-2}$)	18.13	25.04	25.04
FF (%)	78.51	73.23	81.54
Efficiency (%)	6.75	9.812	11.47
	(On a n-cSi layer having N_D = 1× 10^{16} cm-3, N_C = 3 × 10^{19} cm-3, N_V = 3 × 10^{19} cm-3, χ = 4.05 eV, thickness = 100 μm)	(On a n-cSi layer having N_D = 5 × 10^{18} cm-3, N_C = 3 × 10^{19} cm-3, N_V = 3 × 10^{19} cm-3, χ = 3.7 eV, thickness = 100 μm)	(On a n-cSi layer having N_D = 5 × 10^{18} cm^{-3}, N_C = 2.8 × 10^{19} cm^{-3}, N_V = 1.04 × 10^{19} cm^{-3}, χ = 3.7 eV, thickness = 100 μm)

6.6   Summary

We reported the simulation of TCO (ITO)/p-Gr/n-cSi/Ag structure of a p-graphene/n-crystalline silicon solar cell by using AFORS-HET software under the illumination conditions of AM1.5G. Here, graphene has been considered as 3D in

nature and to ensure the formation of Schottky junction, electrical contacts were made along c-axis in order to collect the minority carriers, which are generated upon illumination. Independent effects of seven parameters of graphene layer were analyzed and only one parameter i.e. electron mobility (μ_n) was not found as influencing while others parameters were found to directly have an effect on the cell performance. Power conversion efficiency of 6.75 % has been achieved with best-simulated cell's parameters of p-type single layer graphene. It has been observed that as layer number increases up to 20, efficiency decreases linearly upto 4.34 % due to lower transmittance to silicon layer. Through the optimization of n-crystalline silicon layer parameters, a maximum efficiency of 9.812 % has been achieved for 80 μm thick silicon. Simulated heterojunction photovoltaic device has shown large temperature dependence. Cell performance has been further tested taking parameters of commercial available n-type Si and simulated results are found to be in accordance with reported experimental values. Optimum efficiency of 11.47 % has been achieved for 100 μm thick commercial silicon layer. As-shown above, efficiency did not change much with thickness of graphene as well Si suggests that the cost of cell can be reduced to about 30 %. We can conclude that if experimentally chemical doping can reduce the sheet resistance and enhance work function, then p-type multilayer graphene can act as a highly efficient transparent conducting electrode than n-type graphene.

Previously, experimental efficiency of graphene/silicon cells has been enhanced upto 9.27 % by chemically doping the multilayer graphene [22] and in other report [5], 7.7% efficiency was reported by tuning graphene work function, layer number and antireflection film. This chapter reports on further advancement in graphene/silicon cells in terms of tuned parameters optimized for graphene as well as of silicon. We achieved efficiency of 9.812 % on optimizing both p-graphene and n-c silicon layers

whereas 11.47 % was obtained for 100 μm commercial silicon by tuning graphene properties. In addition, temperature dependence of cell efficiency are discussed which is found similar to silicon cells.

References

[1] F. Giannazzo, S. Sonde and V. Raineri, Electronic properties of graphene probed at the nanoscale, Physics and Applications of Graphene - Experiments, edited by Sergey Mikhailov, InTech., 2011, pp. 353-376.

[2] M. G. Ancona, Electron transport in graphene from a diffusion-drift Perspective, IEEE Trans. on Electron Devices 57 (3) (2010) 681-689.

[3] K. Patel, P.K. Tyagi, Multilayer graphene as a transparent conducting electrode in silicon heterojunction solar cells, AIP Adv. 5 (2015) 077165.

[4] S. D. Sarma, S. Adam, E. H. Hwang, and E. Rossi, Electronic transport in two dimensional graphene, Reviews of Modern Physics83 (2011) 407- 470.

[5] Y. Lin, X. Li, D. Xie, T. Feng, Y. Chen, R. Song, H. Tian, T. Ren, M. Zhong, K. Wang, H. Zhu, Graphene/semiconductor heterojunction solar cells with modulated antireflection and graphene work function, Energy Environ. Sci. 6 (2013) 108–115.

[6] X. Miao, S. Tongay, M. K. Petterson, K. Berke, A.G. Rinzler, B.R. Appleton, A. F. Hebard, High efficiency graphene solar cells by chemical doping, Nano Lett. 12 (2012) 2745–2750.

[7] M. M. Abd El-Raheem, H. M. Ali, N.M. Al-Hosiny, M. S. Abd El Aal, Improvement of the optical properties of ITO/SiO$_2$/glass films for photovoltaic applications, J. Non oxide Glasses 2 (1) (2010) 67-76.

[8] T. Ohshima, T. Matsunaga, H. Kawasaki, Y. Suda, Y. Yagyu, Preparation of ITOthin films by pulsed laser deposition for use as transparent electrodes in electronic display devices, Trans. Mater. Res. Soc. Jpn. 35 (3) (2010) 583-587.

[9] S. Zare, H. Izadkhah, C. Vittoria, Deposition of magnetoelectric hexaferrite thin films on substrates of silicon, J. Magnetism Magnetic Mater. 420 (2016) 245-248.

[10] Z.H. Ni, H.M. Wang, J. Kasim, H.M. Fan, T. Yu, Y.H. Wu, Y.P. Feng, Z.X. Shen, Graphene thickness determination using reflection and contrast spectroscopy, Nano Lett. 7 (2007) 2758-2763.

[11] F.J. Nelson, V.K. Kamineni, T. Zhang, E.S. Comfort, J.U. Lee, A.C. Diebold, Optical properties of large-area polycrystalline chemical vapor deposited graphene byspectroscopic ellipsometry, Appl. Phys. Lett. 97 (2010) 253110.

[12] S. Zhong, X. Hua, W. Shen, Simulation of high-efficiency crystalline silicon solar cells with homo-hetero junctions, IEEE Trans. Electron Devices 60 (7) (2013) 2104-2110.

[13] U. Gangopadhyay, S. Roy, S. Garain, S. Jana, S. Das, Comparative simulation study between n- type and p- type silicon solar cells and the variation of efficiency of n- type solar cell by the application of passivation improvement layer with different thickness using AFORS HET and PC1D IOSR, J. Eng. 2 (8) (2012) 41-48.

[14] W. Lishing, C. Fengxiang, Simulation of high efficiency bifacial solar cells on ntype substrate with AFORS-HET, J. Optoelectron. Adv. Mater. 13 (1) (2011) 81-88.

[15] M. Mohammed, Z. Li, J. Cui, T. Chen, Junction investigation of graphene/silicon Schottky diodes, Nanoscale Res. Lett. 7:302 (2012).

[16] S. Tongay, M. Lemaitre, X. Miao, B. Gila, B.R. Appleton, A.F. Hebard, Rectification at graphene-semiconductor interfaces zero- gap semiconductorbased diodes, Phys. Rev. X, 2. (2012), 011002.

[17] Y.W. Tan, Y. Zhang, K. Bolotin, Y. Zhao, S. Adam, E.H. Hwang, S.D. Sarma, H.L. Stormer, P. Kim, Measurement of scattering rate and minimum conductivity in graphene, Phys. Rev. Lett. 99 (2007) 246803.

[18] E. Tiras, S. Ardali, T. Tiras, E. Arslan, S. Cakmakyapan, O. Kazar, J. Hassan, E. Janzen, E. Ozbay, Effective mass of electron in monolayer graphene: electron-phonon interaction, J. Appl. Phys. 113 (2013) 043708.

[19] K. Zou, X. Hong, J. Zhu, The effective mass of bilayer graphene: electron-hole asymmetry and electron-electron interaction, Phys. Rev. 84 (2011) 085408.

[20] G. Pirruccio, L.M. Moreno, G. Lozano, J.G. Rivas, Coherent and broadband enhanced optical absorption in graphene, ACS Nano 7 (6) (2013) 4810-4817.

[21] C.C. Hu, *Modern Semiconductor Devices for Integrated Circuits*, First ed, Ch1, Prentice Hall, United States, 2010, pp. 1-33.

[22] X. Li, D. Xie, H. Park, M. Zhu, T.H. Zeng, K. Wang, J. Wei, D. Wu, J. Kong, H. Zhu, Ion doping of graphene for high-efficiency heterojunction solar cells, Nanoscale 5 (2013) 1945-1948.

[23] T. Feng, D. Xie, Y. Lin, H. Zhao, Y. Chen, H. Tian, T. Ren, X. Li, Z. Li, K. Wang,D. Wu, H. Zhu, Efficiency enhancement of graphene/silicon-pillar-array solar cells by HNO_3 and PEDOT-PSS, Nanoscale 4 (2012) 2130-2133.

[24] T. Cui, R. Lv, Z.H. Huang, S. Chen, Z. Zhang, X. Gan, Y. Jia, X. Li, K. Wang, D. Wu,F. Kang, Enhanced efficiency of graphene/silicon heterojunction solar cells by molecular doping, J. Mater. Chem. A 1 (2013) 5736-5740.

[25] K. Ruan, K. Ding, Y. Wang, S. Diao, Z. Shao, X. Zhang, J. Jie, Flexible graphene/silicon heterojunction solar cells, J. Mater. Chem. A 3 (2015) 14370-14377.

[26] E. Shi, H. Li, L. Yang, L. Zhang, Z. Li, P. Li, Y. Shang, S. Wu, X. Li, J. Wei, K. Wang, H. Zhu, D. Wu, Y. Fang, A. Cao, Colloidal antireflection coating improves graphene-silicon solar cells, Nano Lett. 13 (2013) 1776-1781.

[27] T. Kirchartz, K. Ding, U. Rau, Fundamental electrical characterization of thin film solar cells, in: D. Abou-Ras, T. Kirchartz, U. Rau (Eds.), *Advanced Characterization Techniques for Thin Film Solar Cells*, Weinheim:Wiley-VCH, 2011, pp. 35-60.

[28] W. Xu, H. M. Dong, Photo-Induced Carrier Density, Optical Conductance and Transmittance in Graphene in the Presence of Optic-Phonon Scattering, in: Mikhailov S (Ed.) *Physics and Applications of Graphene – Theory*, InTech, 2011, pp. 509-512.

[29] P. Singh, N. M. Ravindra, Temperature dependence of solar cell performance—an analysis, Solar Energy Materials & Solar Cells 101 (2012) 36–45.

Chapter 7

Application of multilayer graphene (n-type) as

a transparent conducting electrode

7.1 Introduction

In this chapter, simulation of TCO (ITO)/n-Gr/p-cSi/Ag structure of an n-graphene/p-crystalline silicon solar cell was carried out and results have been discussed in details. Simulation has been performed using AFORS-HET software under the illumination conditions of AM1.5G. Details of simulation parameters for graphene and silicon layers are given in tabular form in addition to contact details. For each layer, the effects of parameter variations on cell parameters are described. After optimizing the n-graphene layer, the parameters of p-c silicon layer has been varied and their effects on cell response are discussed. For different optimized layer with maximum efficiency cells, spectral response, quantum efficiency and temperature dependence are also discussed in detail. The presented results in this chapter have been published in **Kamlesh Patel and Pawan K Tyagi, AIP Advances 5, 077165 (2015)** http://dx.doi.org/10.1063/1.4927545.

7.2   n-graphene/pc-Si solar cell structure

The proposed cell structure is configured as TCO (ITO)/n-Gr/p-cSi/Ag in **Fig. 7.1(a)**and transport of minority carriers is considered along the c-axis of graphene. We used the diffusion-drift solver and Metal -Schottky junction available in AFORS-HET for describing the equivalent model of our Gr/Si heterojunction cell. In simulation,

thickness of single layer graphene was fixed at one atom i.e. ~0.334 nm [1] and then the six parameters of graphene were varied in the practicable ranges. These parameters were taken as the donor concentration (N_D), effective conduction and valance band densities (N_C/N_V), bandgap (E_g), electron affinity (χ), relative permittivity (ε_r) and electron mobility (μ_n). Then the simulation was performed for multilayer graphene silicon cells for different layer numbers. On achieving an efficiency around 7.62 %, different parameters of p-crystalline silicon (p-cSi) were varied to achieve the highest efficiency [2-3].
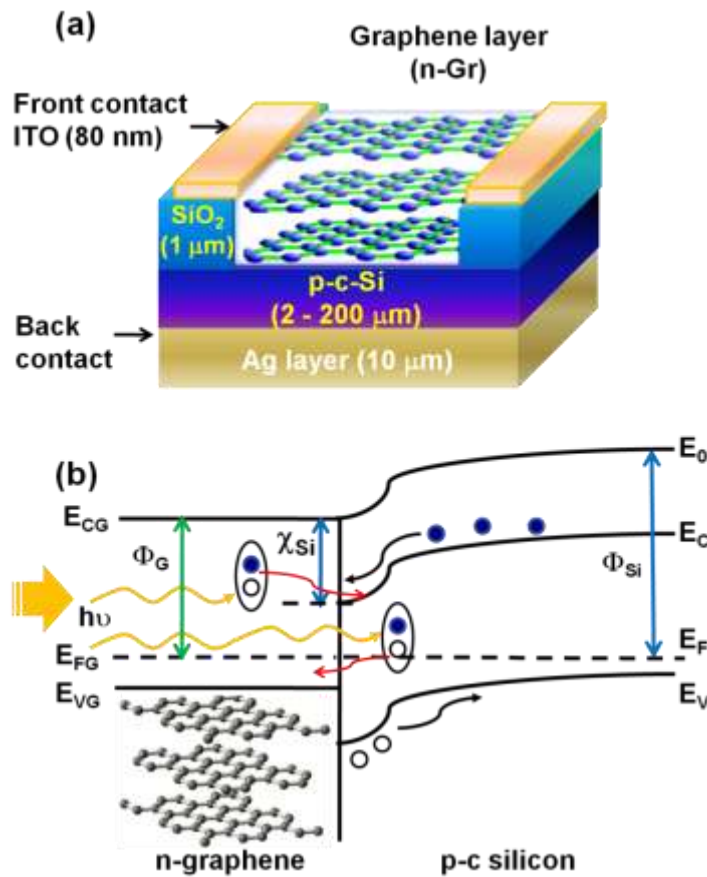
Fig. 7.1 n-Graphene/p-crystalline silicon heterojunction solar cell (a) Schematic of cell configuration used in simulation, (b) Band diagram of a forward biased junction, where Φ_G, Φ_{Si} and χ_{Si} are the graphene work function, silicon work function, and the silicon electron affinity, respectively.

We optimized the p-cSi layer for acceptor concentration (N_A), effective conduction and valance band densities (N_C/N_V), the electron affinity (χ) and thickness. The standard values of other parameters of p-cSi like the relative permittivity (ε_r), electron mobility (μ_n) and bandgap (E_g) were considered in simulation as reported [2-5].Finally, we have reported the highest efficiency achieved in n-Gr/p-cSi heterojunction cell after fully optimizing the parameters of both layers. As we know that the graphene and semiconductor interface barrier is ideally Schottky in nature, a built-in voltage (V_{BI}) developed at the depletion region of silicon wafer results due to recombination of the majority charge carriers at the interface, which are the electrons in n-Gr and the holes in the p-cSi wafer, respectively. However, the minority carriers i.e. electrons in p-cSi wafer transport towards the graphene layer and the energy levels bend downward near the interface [6]. This voltage (V_{BI}) is the difference of the barrier height (Φ_{BI}) and energy gap in the silicon, and the barrier height (Φ_{BI}) a difference of the work function of graphene and silicon, is given by the following equation [7],

$$\Phi_{BI} = \Phi_G - \Phi_{Si} = \Phi_G - \chi_{Si} - k_B T \ln \left(N_A \big/ N_V \right)_{Si} \tag{7.1}$$

where Φ_G, Φ_{Si} and χ_{Si} are the graphene work function, the silicon work function and the silicon affinity, respectively. Here N_A and N_V are the acceptor doping concentration and the effective valence band density of the p-cSi, respectively. After illumination, electron and hole (e-h) pairs are generated and then separated due to the built in voltage at interface. These photo-generated carriers then move towards n-Gr and p-cSi regions, respectively as shown in **Fig. 7.1(b)**[6].Since the carrier density becomes higher in the respective regions, the built-in voltage produces an open circuit voltage (V_{OC})when the cell is open circuited. When short circuiting the cell, the excess carriers are collected at

the respective electrodes, causing a short circuited current flow in the external circuit. The details of the front and back contacts have been given in Table 7.1. The values for various parameters and ranges for layers have been summarized in Table 7.2.

Table 7.1: Details of the front and back contact parameters of the cell used for simulation.

Contact Parameters	Front contact	Back contact
Width (cm)	8×10^{-6}	0.001
File	ITO.nk	Ag.nk
Metal work function	Yes (flatband)	Yes (flatband)
Absorption loss	ITO.abs	0
External reflection constant	aSicSi_ITO.ref	0
Surface condition	Plane	Plane
Internal reflection constant	0	0

Table 7.2: The values and ranges of layerparameters taken for the simulation of the cell structure.

Input Parameters	n-Gr	p-cSi
Relative permittivity, ε_r	4 - 11	11.9
Electron mobility, μ_n (cm^2/V.s)	$1 - 1\times10^6$	1350
Hole mobility, μ_p (cm^2/V.s)	10	450
Electron Affinity, χ (eV)	3.5 – 4.5	3.6 – 4.3
Band gap, E_g (eV)	0 – 0.25	1.12
Acceptor concentration N_A(cm^{-3})	0	1×10^{14}-5×10^{18}
Donor concentration N_D (cm^{-3})	$1\times10^{14} - 1\times10^{18}$	0
Effective conduction band density, N_C (cm^{-3})	3×10^{18} - 3×10^{21}	3×10^{19} - 6×10^{21}
Effective valance band density, N_V (cm^{-3})	3×10^{18} - 3×10^{21}	3×10^{19} - 6×10^{21}
Thermal velocity of electrons (cm/s)	1×10^7	1×10^7
Thermal velocity of holes (cm/s)	1×10^7	1×10^7
Layer density (g/cm)	2.328	2.328
Thickness (cm)	3.34×10^{-8} - 6.68×10^{-7}	2×10^{-3}-3×10^{-2}
Mid bandgap density of states (cm^{-3}/eV)	-	Single acceptor
Switch-over energy (eV)	-	0.56
Auger recombination coefficient for electron (cm^6/s)	0	0
Auger recombination coefficient for hole (cm^6/s)	0	0
Direct band-to-band recombination coefficient (cm^3/s)	0	0
Optical properties	n = 2.7, k = 1.45	cSi.nk

7.3 Optimization of n-graphene layer

At first, donor concentration (N_D) of graphene layer was optimized while keeping other parameters to some significant values as shown in **Fig. 7.2 (a-b) [8-9]**. Earlier, it was reported thatefficient electron injection can be obtained if the work function of the graphene layer as electrode is reduced **[10]**. By doping with nitrogen and phosphorus atoms, Φ_G of n-type graphene has been reported to reduce from 3.8 eV to 3.6 eV, which increases the Fermi level of graphene from the Dirac point and also leads to a significant increase in carrier density **[10]**. With increasing N_D, the conductivity of the graphene layer becomes higher due to collection of free carriers. The short-circuit current density (J_{SC}) getsreduceda little from 19.24 mA/cm^2 to 18.94mA/cm^2 as the rate of recombination also increased with N_D. An effective increase in V_{OC} from 150.8 to 175.8 mV was also observed during the process leading to improved efficiency (η). However, fill factor (FF) was found to have a constant value till higher N_D of 10^{17} cm^{-3}. After a higher value of N_D at 10^{17} cm^{-3}, the FF was found to increase suddenly, improving the cell quality. This further increment in FF may be due to lowering of the sheet resistance of graphene, which is inversely proportional to the carrier density in graphene. Resistance in graphene has been reported to be a part of series resistance of the cell that can be easily reduced by doping **[7]**. After N_D of 10^{18} cm^{-3}, η was found to be 1.994 %. The behaviour of V_{OC} and J_{SC} are found to be affected exponentially with the optimized range of N_D which is in well agreement with the previous report **[11]**.
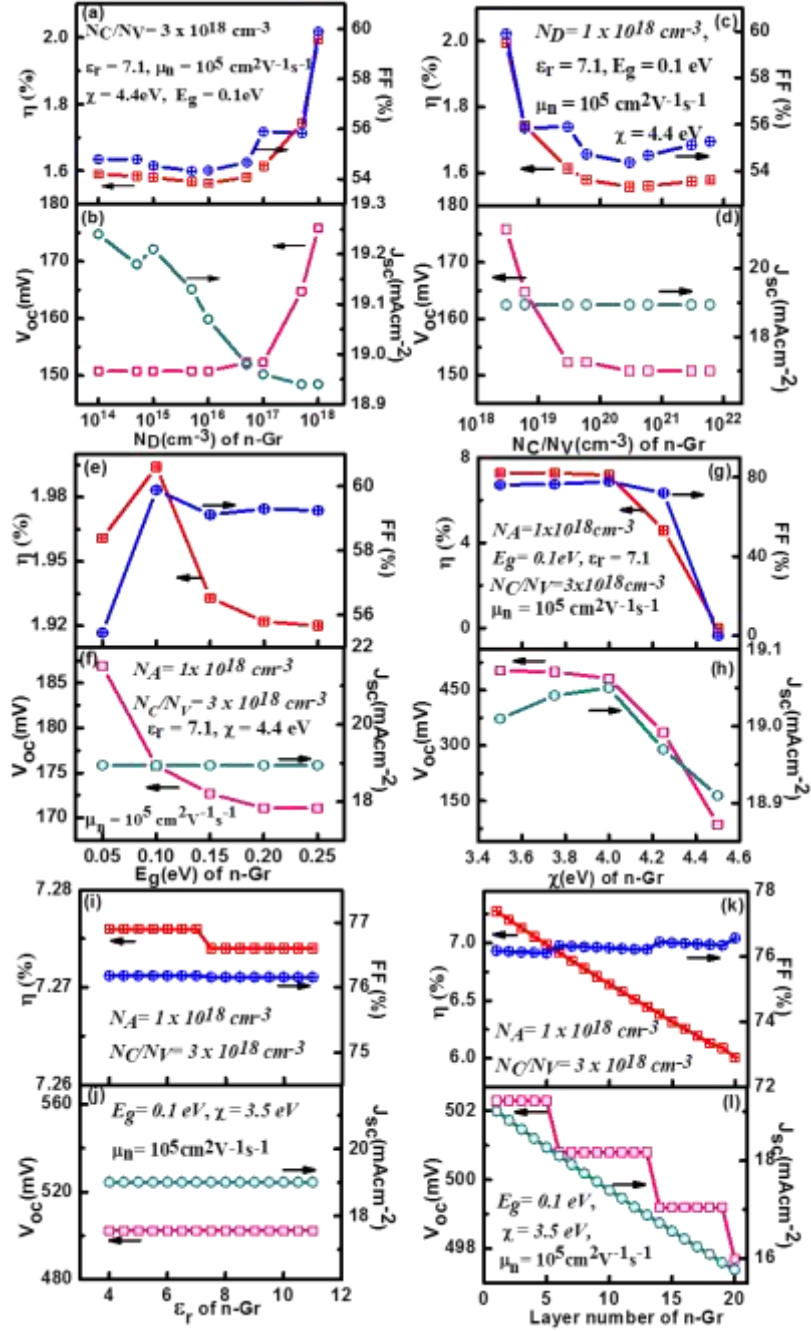
Fig. 7.2 Schematic representation for the optimization of the parameters of n-graphene layer, (a-b) the donor concentration (N_D) (cm^{-3}), (c-d) the effective density of states (N_C/N_V) (cm^{-3}), (e-f)) the bandgap energy (E_g) (eV), (g-h) the electron affinity (χ) (eV), (i-j) the relative permittivity (ε_r), and (k-l) layer number. The parameters of p-cSi used were: the acceptor concentration (N_A) = 1×10^{16} cm^{-3}, the effective density of states (N_C/N_V) = 3×10^{19} cm^{-3}, the electron affinity (χ) = 4.05 eV and thickness 100 μm. The other parameters are given in Table 7.2.

On varying N_C/N_V of n-Gr from 3×10^{18} to 3×10^{21} cm^{-3}, the observed minority carrier densities were trimmed down probably due to the higher recombination rate of photo-generated carriers near the junction. With the absence of free minority carriers, the Fermi level of n-Gr was pinned, which makes Φ_{Bl}independent ofΦ_G and the collection of the photo-generated carriers become independent of N_C/N_V [7].Therefore, J_{SC} was constant at 18.94 mA/cm^2. Also, in graphene the charge carriers were reported to be massless Dirac fermions [12]. In Fig. 7.2 (c-d), it has been demonstrated that the open circuit voltage (V_{OC}) reduces almost sharply with an increase in the band densities inside n-Gr layer with higher N_C/N_V. Thus, the reduced values of V_{OC} and constant J_{SC} led to a drop in η to 1.578 % at 3×10^{21} cm^{-3} of N_C/N_V. The maximum η of 1.994 % was obtained for N_C/N_V of 3×10^{18} cm^{-3}.

After optimizing N_D and N_C/N_V to 10^{18} cm^{-3} and 3×10^{18} cm^{-3}, respectively, the bandgap energy (E_g) of the n-Gr has been varied from 0 eV to 0.25 eV. As E_g increases, V_{OC} was decreased as built-in voltage is reduced and J_{SC} becomes almost constant as lower barrier voltage allows more photo-generated carriers to cross the n-Gr/p-cSi junction, which is shown in **Fig. 7.2(e-f)**. As the fill factor inversely depends on the effective resistance to the charge carriers in n-Gr layer, lower V_{OC} and FF reduced η from 1.994 % (@ E_g = 0.1 eV) to 1.92 % (@E_g = 0.25 eV). Simulation response of the electron affinity (χ) is shown in **Fig. 7.2 (g-h)**. On increasing χ from 3.5 eV to 4 eV, J_{SC} decreased slightly while V_{OC} remained almost constant. Both reduced on increasing χ above 4.0 eV as the reduction in barrier height probably enhances the transfer of minority charge carriers and collection of carriers is reduced, which results to decrease in J_{SC}. Thus, η almost linearly decreased for higher values of χ in n-Gr layer and for χ = 4.5 eV, η~ zero is obtained. The maximum η of 7.276 % was obtained at χ = 3.5 eV.

The relative permittivity (ε_r) of the graphene layer does not seem to contribute in the efficiency in the simulation ranges as shown in **Fig. 7.2 (i-j)** and the cell parameters were found to remain independent, providing η of 7.276 %. To study any role of graphene thickness in the carrier generation from the photon absorption with the above-optimized values, we simulated the cell for multilayer graphene up to 40 layers where the thickness of a single layer was taken as 0.334 nm. It was seen that the layer numbers can reduce the transmittance in order of 2.3 % absorbance per layer and the sheet resistance of the graphene **[7]**. With increase in the layer numbers, the sheet resistance was found to decrease along with a reduction in the graphene's transmittance. So it can be said that the improvement in η due to the reduced sheet resistance has been compensated largely with the lower transparency. In our simulation, the cell parameters were found to be reduced linearly except FF up to 20 layers. With 20 layers, η was reduced to 6.007 %. Therefore, n-graphene as a multilayer electrode can play an active role for the photo carrier generation in our simulated cell with providing a Schottky junction for the current movement.

7.4 Optimization of p-cSi layer

Most of published studies have been reported either simulated or experimental work on the Gr/Si heterojunction cells, the optimization of c-Si layer is still not performed. In order to get better efficiency in cell, the simulation of the p-cSi parameters is needed. When the acceptor concentration (N_A) in p-cSi layer was raised from 10^{14} cm^{-3}, Φ_{SI} decreased leading to an increase of Φ_{BI} (Eq. 7.1)as well as V_{OC}. Also the reduction in the depletion region resulted in higher V_{BI}, which accelerated the separation of photo-generated carriers. The quantum tunneling probability may increase

and enhance J_{SC} to the higher value due to better carrier separation at the interface. It can be seen in **Fig. 7.3 (b)**, J_{SC} becomes constant after 5×10^{15} cm^{-3}, while V_{OC} strengthens in proportion to N_A due to high carrier accumulation at the junction. At higher N_A values, J_{SC} increases probably due to carrier–carrier scattering in a p-cSi layer [2]. The voltage gradient at the junction was found improved possibly due to low carrier transport [2]. Beyond 10^{17} cm^{-3}, J_{SC} increased due to the excess charge carriers at higher N_A in p-cSi wafer. Consequently, η reached at its peak ~12.29 %, while the quality of cell improved due to lower contact resistance and confirmed by FF ~ 80.75% for 5×10^{18} cm^{-3} as shown in **Fig. 7.3 (a)**.

The effective conduction band density (N_C) and effective valence band density (N_V) play a crucial role in controlling the charge carrier flow inside the semiconductors. Here, we have varied N_C/N_V parameter in the range of 3×10^{19} to 6×10^{21} cm^{-3} and their effects on cell parameters are shown in **Fig. 7.3 (c-d)**. For simulated n-Gr/p-cSi cell, the p-cSi layer with N_C and N_V values at 3×10^{19} cm^{-3} have shown highest η upto 12.29 % and further increase in N_C/N_V has reduced the efficiency. Beyond this value, although J_{SC} infinitesimally was improved, increase in N_C and N_V values of p-cSi layer developed short-interval states for charge carriers, so V_{OC} and FF dropped in the cell. The efficiency (η) follows V_{OC} and reduces to 6.894 % at Nc/Nv values of 6×10^{21} cm^{-3}. Thus, the higher density values for thick p-cSi wafer degrade V_{OC} and FF in the cell and made J_{SC} to improve a little.

The electron affinity controls the transport at interfaces on both sides of p-cSi layer, where one side the graphene layer is placed and on the other side, Ag layer is there. We have optimized χ(eV) of graphene layer to 3.5 eV, where V_{OC} is maximum and leading to η≈ 13.66 % and other parameters, J_{SC} and FF shown a little increase

while enhancing χ (eV) of p-cSi wafer from 3.6 eV. However, as shown in **Fig. 7.3 (e-f)**, η is largely affected by χ (eV), which controls the barrier height at the interface and quality of cell. To study the effect of wafer thickness, we have taken 20 μm thick p-cSi wafer to start with significant values of J_{SC} and V_{OC} and then increased the thickness up to 300 μm. At lower thickness, both J_{SC} and V_{OC} were steeply raised due to increase of majority charge carriers i.e. holes and barrier voltage sharply increased as well as effective collection of carriers, shown in **Fig. 7.3 (g-h)**. In 100 μm thick p-cSi layer, the lifetime of minority charge carriers i.e. electrons get reduced that may be due to the reduction in their drift length. At this thickness, no improvement in J_{SC} and V_{OC} was observed even on increasing the thickness to 300 μm **[2]** and η remained at 13.66%.

This high efficiency of 13.66 % is impractical for a single layer n-Gr/p-cSi solar cell on 100 μm silicon substrate, since in the present simulation we have not considered the optical and electrical losses at the interface and contacts. So, we have simulated the electron affinity (χ) and thickness of p-cSi layer at most reported experimental values for Si such as $N_A \approx 2 \times 10^{16}$ cm^{-3}, $N_C \approx 2.8 \times 10^{19}$ cm^{-3}, $N_V \approx 1.04 \times 10^{19}$ cm^{-3}**[13]**. On these values, the simulated responses of cell parameters with χ (eV) are shown in **Fig. 7.3 (i-j)**, which are different from those reported in **Fig. 7.3 (e-f)**. A maximum efficiency was found only 8.491 % at χ = 4.2 eV of Si. The short-circuit current density J_{SC} has shown only a little decrement with χ, while V_{OC} was increased for large χ of 3.6 to 4.4 eV. Constant V_{OC} and FF observed at higher χ values, forces the efficiency η to be constant $\approx$ 8.491 % at χ = 4.4 eV. Similar to **Fig. 7.3 (g-h)**, the thickness of p-cSi has been varied on the new values of N_A, N_C/N_V and χ = 4.4 eV. The significant changes in cell parameters have been observed for lower thickness range only as illustrated in **Fig. 7.3(k-l)**.
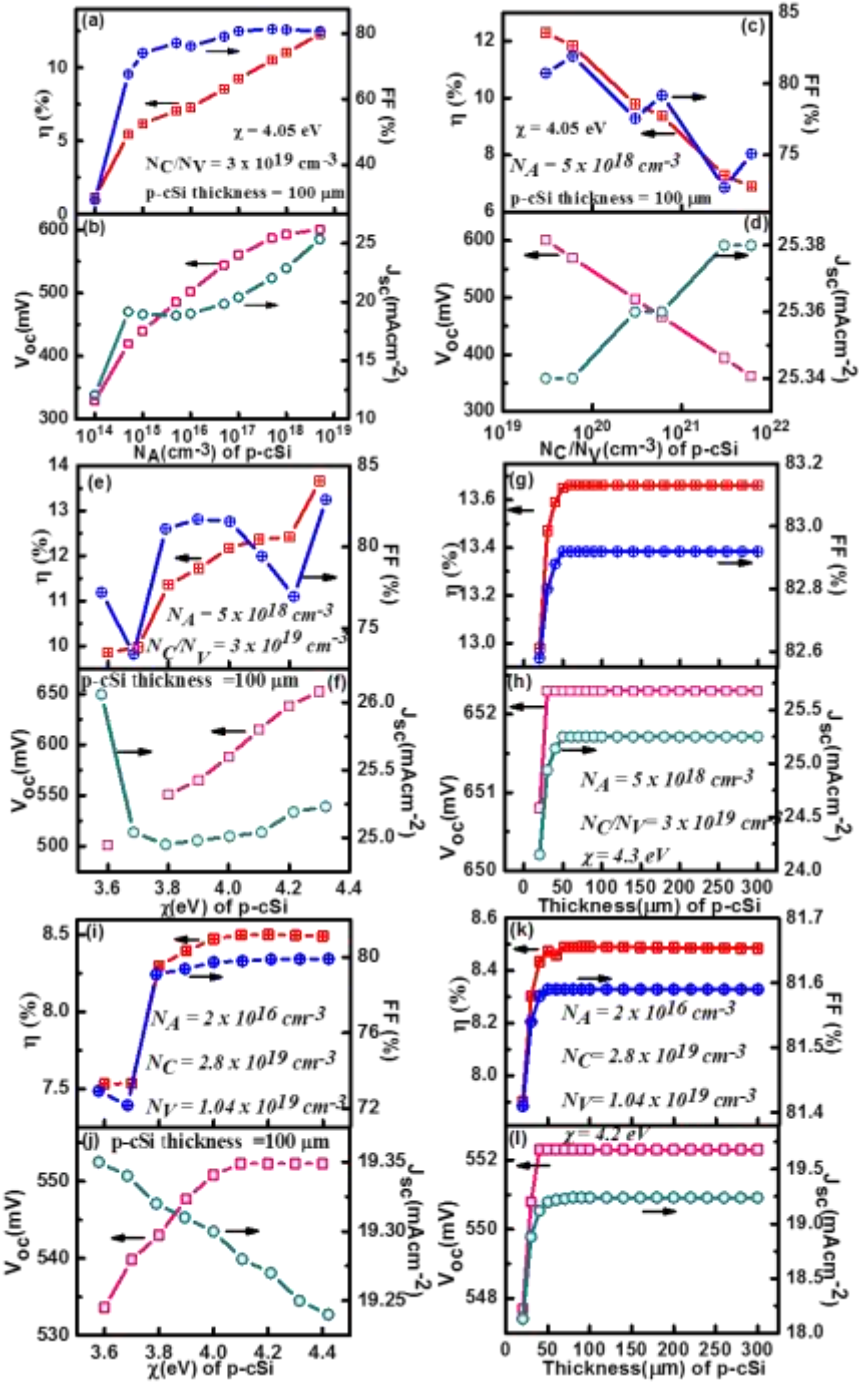
Fig. 7.3 Schematic representation of cell performance with the optimization of the parameters of p-cSi layer, (a-b) the acceptor concentration N_A (cm^{-3}), (c-d) the effective band density Nc/Nv (cm^{-3}), (e-f) the electron affinity χ (eV), (g-h) thickness (μm). At $N_D = 2 \times 10^{16}$ cm^{-3}, Nc $= 2.8 \times 10^{19}$ cm^{-3} and Nv $= 1.04 \times 10^{19}$ cm^{-3} for p-cSi, (i-j) the electron affinity χ (eV) and (k-l) thickness (μm). The optimized parameters of n-Gr were $N_D = 1 \times 10^{18}$ cm^{-3}, $N_C/N_V = 3 \times 10^{18}$ cm^{-3}, $E_g = 0.1$ eV, $\chi = 3.5$ eV, $\varepsilon_r = 7.1$, $\mu_n = 10^5$ cm^{2}V^{-1}s^{-1}.

For values greater than 50 μm, the high rate of carrier recombination forced V_{OC} and J_{SC} to exhibit a constant value inside the thick p-cSi layer with equivalent photo-carrier generation. In addition, the effective series resistance of the cell remains constant as the total cell area is increased with thickness, and resulted in fill factor independent of silicon layer thickness. The constant cell parameters kept η to the saturated value of 8.491 % irrespective of the layer thickness.

7.5 Spectral response, quantum efficiency and temperature dependence

The wavelength dependent characteristics, spectral response (SR), internal QE (IQE) and external QE (EQE) of the best optimized cell have been shown in **Fig. 7.4**. The graphene layer was found to be absorbing the major fraction of light in the wavelength range below 600 nm. This results in less numbers of photon reaching to p-cSi layer and subsequently photocurrent generation is low. With optimized graphene parameters, most photons having less energy in the range from 600 to 1000 nm and reached to Si layer, their energy is converted into electrical energy inside Si layer. So, only efficiency of 7.276 % was achieved by tuning the properties of graphene layer as illustrated in **Fig. 7.4 (a)**. On increasing the doping concentrations in the p-cSi layer, the SR enhances with higher J_{SC} due to high carrier generation. With the optimization of silicon layer, the absorption of the photons is found to be increased in the shorter wavelengths (300 nm to 600 nm) and the efficiency is reached to 13.66 % and 8.491 %, respectively for different values of N_A and N_C/N_V in 100 μm Si. As the silicon is an indirect bandgap semiconductor with $E_g = 1.12$ eV, the SR has been reaching zero with the longer wavelength > 1000 nm.

The internal quantum efficiency (IQE) of cell has been observed to increase further at the shorter wavelengths < 500 nm after optimizing the parameters of silicon layer, as shown in **Fig. 7.4(b)**. The optical losses are found to be dominant at the shorter wavelengths for graphene optimized cell as revealed by the low EQE response in **Fig. 7.4(c)**. The optimization of graphene and silicon layers led the reduction in reflection and transmission losses of the cells. Hence, higher EQE is obtained for the wavelengths in the range of 400 nm - 600 nm.
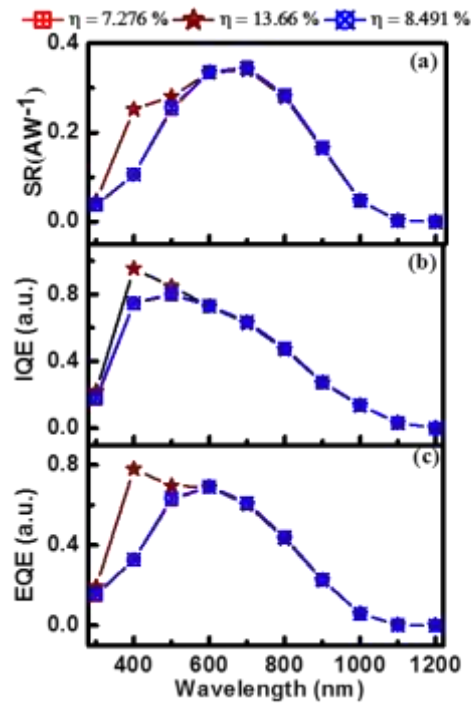
Fig. 7.4 (a) Spectral response (SR), (b) Internal quantum efficiency (IQE), and (c) External quantum efficiency (EQE) of best optimized single layer n-Gr/p-cSi cells (η = 7.276 % graphene layer optimized, η = 13.66 % with $N_A = 5 \times 10^{18}$ cm^{-3} and $N_C/N_V = 3 \times 10^{19}$ cm^{-3} for 100 μm p-cSi, respectively, η = 8.491 % with $N_A = 2 \times 10^{16}$ cm^{-3}, $N_C = 2.8 \times 10^{19}$ cm^{-3} and $N_C = 1.04 \times 10^{19}$ cm^{-3} for 100 μm p-cSi).

Higher EQE suggests that doping concentration and effective band density optimization significantly increases the electron-hole pair generation and subsequent collections of excess charge carriers and high efficiencies ~13.66 % and 8.491 % have been achieved. Similar IQE and EQE responses of cells with these efficiencies are indicating the same number of charge carriers collected at these wavelengths against the photons absorbed into the cells. For longer wavelengths, the photons are unable to generate the carriers and IQE and EQE are reduced to zero.
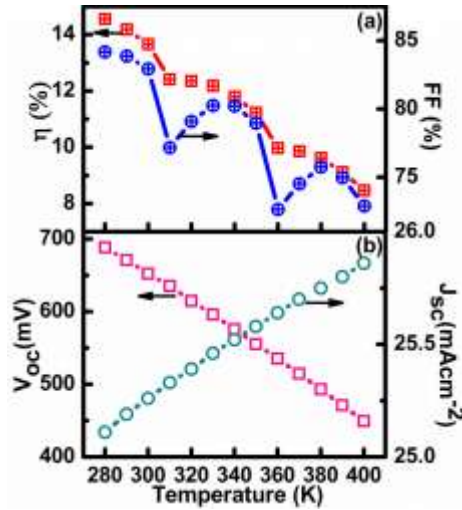
Fig. 7.5 Dependence of cell response ($\eta = 13.66$ %)(a) efficiency, (b) fill factor, (c) J_{SC} and (d) V_{OC} with temperature variation.

To observe the cell response in high as well as low temperature ranges due to seasonal changes on the earth is of high value, so simulation of best-optimized cell structure of efficiency 13.66 % was performed in 280 K to 400 K range and shown in **Fig. 7.5(a-b)**. As temperature rises from 300 K (RT), band bending reduced at graphene/Si interface. The optical scattering by phonons in graphene layer **[14]**, helps the electrons to move in the conduction band from the valance band through the photoemission. Hence, at the higher temperatures the more photo-generated electrons in

the conduction band enhanced J_{SC}. As temperature decreases from RT, carrier generation rate also decreased at the interface and resulted in lower J_{SC}. As V_{OC} and FF were found to be high, a higher efficiency of around 14.55 % was obtained at 280 K. For silicon cells, as the reverse saturation current density (J_0) controls the effect of temperature on V_{OC}, while J_0 decreases with temperature [15]. As a result, V_{OC} has been dropped linearly and FF and η reduced, although J_{SC} improved a little. Table 7.3 summarized the parameters of optimized cells with efficiencies 7.276 %, 13.66 % and 8.491 %. **Fig. 7.5** also represents the rate of change in V_{OC}, J_{SC}, FF and η with temperature and we found, $dV_{OC}/dT \approx - 0.63$ mV K^{-1}, $dJ_{SC}/dT \approx 0.013$ mAcm^{-2} K^{-1}, $dFF/dT \approx -0.04$ % K^{-1} and $dη/dT \approx -0.061$ % K^{-1}.

Table 7.3: Summary of the parameters of the best optimized graphene/silicon cells.

Cell parameters	n-graphene layer optimized cell	n-graphene layer and p-cSi layer optimized cell	
V_{OC} (mV)	502.3	652.3	552.3
J_{SC} (mAcm^{-2})	19.01	25.26	19.24
FF (%)	76.18	82.92	79.91
Efficiency (%)	**7.276**	**13.66**	**8.491**
	(On a p-cSi layer having $N_A = 1 \times 10^{16}$ cm^{-3}, $N_C = 3 \times 10^{19}$ cm^{-3}, $N_V = 3 \times 10^{19}$ cm^{-3}, $\chi = 4.05$ eV, thickness = 100 μm)	(On a p-cSi layer having $N_A = 5 \times 10^{18}$ cm^{-3}, $N_C = 3 \times 10^{19}$ cm^{-3}, $N_V = 3 \times 10^{19}$ cm^{-3}, $\chi = 4.3$ eV, thickness = 100 μm)	(On a p-cSi layer having $N_A = 2 \times 10^{16}$ cm^{-3}, $N_C = 2.8 \times 10^{19}$ cm^{-3}, $N_V = 1.04 \times 10^{19}$ cm^{-3}, $\chi = 4.2$ eV, thickness = 100 μm)

7.6   Summary

In this chapter, a graphene/silicon heterojunction solar cell as the TCO (ITO)/n-Gr/p-cSi/Ag structure has been studied under simulated conditions. The various parameters of the cell's layers have been optimized by using AFORS-HET software. Independent effects of seven parameters of graphene layer were analyzed and only donor concentration N_D, effective conduction band density (N_C)andeffective conduction band density (N_V), bandgap (E_g), electron affinity (χ) were found to be the influencing parameters in order to control n-Gr/p-cSi cell performance. After optimizing the various parameters of n-type multilayer graphene optimized, best power conversion efficiency of 7.276 % was achieved. Further optimization of the p-crystalline silicon parameters led to achieve a maximum efficiency of 13.66 %. On studying temperature dependence, an efficiency of 14.55 % has been obtained at 280 K. With increasing thickness of Si from 100 μm to 300 μm, infinitesimal enhancement in efficiency was observed, which suggested that the cost of cell can be reduced to about 50 %. We propose that several pre and post treatments on silicon wafers such as use of plasmonics on the contacts, proper cleaning, back surface field and texturing of silicon wafers may also further improve the efficiency.

Since doping with ZnMg, AlOx etc. makes graphene n-type [16-17] and the work function can reduced upto 3.5 eV [7]. Larger work funtion increases the built-in potential causing efficient charge carrier separation and more collections of change carriers at the cell contacts. Encouraged by this fact, we simulated n-graphene/p-crystalline silicon cell configuration for high efficiency, which is hardly explored [6, 18-19]. We used extensively the most experimental data available for graphene layer optimization and an efficiency of 7.276 % was achieved on 100 μm Si wafer. On further optimization of silicon layer provided 13.66 % efficiency whereas 8.49 % efficiency

was obtained for 100 μm commercial silicon by tuning graphene properties only. The simulation reported in this chapter confirms that n-type as well as p-type graphene can be act as efficient TCE for silicon heterojunction cells.

References

[1] Z. H. Ni, H.M. Wang, J. Kasim, H.M. Fan, T. Yu, Y.H. Wu, Y.P. Feng, Z.X. Shen, Graphene Thickness Determination using Reflection and Contrast Spectroscopy, Nano Lett., 7(2007) 2758–2763.

[2] S. Zhong, X. Hua, W. Shen, Simulation of high-efficiency crystalline silicon solar cells with homo–hetero junctions, IEEE Trans. on Electron Devices 60 (7) (2013) 2104-2110.

[3] U. Gangopadhyay, S. Roy, S. Garain, S. Jana, S. Das, Comparative simulation study between n- type and p- type silicon solar cells and the variation of efficiency of n- type solar cell by the application of passivation improvement layer with different thickness using AFORS HET and PC1D, IOSR Journal of Engineering 2 (8) (2012) 41-48.

[4] Z. Zhang, T. Cui, R. Lv, H. Zhu, K. Wang, D. Wu, and F. Kang, Improved efficiency of graphene/Si heterojunction solar cells by optimizing hydrocarbon feed rate, Journal of Nanomaterials 2014 (2014) 359305.

[5] Y. Lin, D. Xie, Y. Chen, T. Feng, Q. Shao, H. Tian, T. Ren, X. Li, X. Li, L. Fan, K. Wang, D. Wu, H. Zhu, Optimization of graphene/silicon heterojunction solar cells, in Proceedings of Photovoltaic Specialists Conference (PVSC) IEEE, 2012, pp. 002566-002570.

[6] M. Mohammed, Z. Li, J. Cui and T. Chen, Junction investigation of graphene/silicon Schottky diodes, Nanoscale Research Letters 7 (2012) 302.

[7] Y. Lin, X. Li, D. Xie, T. Feng, Y. Chen, R. Song, H. Tian, T. Ren, M. Zhong, K. Wang, H. Zhu, Graphene/semiconductor heterojunction solar cells with modulated antireflection and graphene work function, Energy Environ. Sci. 6 (2013) 108–115.

[8] S. Tongay, M. Lemaitre, X. Miao , B. Gila, B.R. Appleton, A.F. Hebard, Rectification at graphene-semiconductor interfaces zero- gap semiconductor-based diodes, Physical Review X, 2 (2012) 011002.

[9] J. Pezoldt, Ch. Hummel, F. Schwierz, Graphene field effect transistor improvement by graphene - silicon dioxide interface modification, Physica E 44 (2012) 985-988.

[10] D. G. Kvashnin, P. B. Sorokin, J. W. Brüning, and L. A. Chernozatonskii, The impact of edges and dopants on the work function of graphene nanostructures: The way to high electronic emission from pure carbon medium, App. Phy. Lett. 102 (2013) 183112.

[11] X. Miao, S. Tongay, M. K. Petterson , K. Berke, A.G. Rinzler, B.R. Appleton, A. F. Hebard, High efficiency graphene solar cells by chemical doping, Nano Lett. 12 (2012) 2745–2750.

[12] A. K. Geim and A. H. MacDonald, Graphene: Exploring carbon flatland, Physics Today 60 (2007) 35-41.

[13] C. C. Hu, *Modern Semiconductor Devices for Integrated Circuits*, 1st ed, Ch 1, Prentice Hall, United States, 2010, pp. 1- 33.

[14] W. Xu, H. M. Dong, Photo-Induced Carrier Density, Optical Conductance and Transmittance in Graphene in the Presence of Optic-Phonon Scattering, in:

Mikhailov S (Ed.) *Physics and Applications of Graphene – Theory*, InTech, 2011, pp. 509-512.

[15] P. Singh, N. M. Ravindra, Temperature dependence of solar cell performance-an analysis, Solar Energy Materials & Solar Cells 101 (2012) 36–45.

[16] X. Meng, S. Tongay, J. Kang, Z. Chen, F. Wu, S.S. Li, J.B. Xia, J. Li, J. Wu, Stable p and n-type doping of few-layer graphene/graphite, Carbon 57 (2013) 507-514.

[17] X. Shi, G. Dong, M. Fang, F. Wang, H. Lin,W.-C. Yen, K. S. Chan, Y.-L. Chueh, and J. C. Ho, Selective n-type doping in graphene via the aluminium nanoparticle decoration approach, J. Mater. Chem. C 2 (2014) 5417 – 5421.

[18] K. Batra, S. Nayak, S. K. Behura, and O. Jani, Optimizing performance parameters of chemically-derived graphene/p-Si heterojunction solar cell, J. Nanoscience and Nanotechnology 14 (2014) 1–6.

[19] S. K. Behura, S. Nayak, I. Mukhopadhyay, O. Jani, Junction characteristics of chemically-derived graphene/p-Si heterojunction solar cell, Carbon 67 (2014) 766 –774.

Chapter 8

Summary and Conclusions

8.1 Summary

Reported study aims to deduce the transmission and dielectric properties of CVD- grown graphene in wide frequency range from 100 MHz to 10 GHz. In this work, on one side the properties of graphene layer were investigated at the microwave frequency range, while on the other side a simulation study was performed for the single layer graphene or multilayer graphene as a transparent conducting electrode (TCE) in silicon heterojunction cells. Such qualitative information enabled application of graphene for microwave passive devices and provided the parameters of graphene as TCE for high cell efficiency in solar cell devices.

Graphene transferred on both glass and quartz substrates of the dimension $1''\times1''$ was procured from Graphene Industries, USA. Another set of graphene layers was grown by using Hot Filament Chemical Vapor Deposition (HFCVD) system on Cu sheet for two different synthesis conditions. In HFCVD, different synthesis parameters were taken as substrate temperature of 850 °C and 950 °C. Raman spectroscopy was performed to confirm single layer graphene transferred on glass and quartz. As-grown graphene on Cu substrates were also probed. Atomic force microscopy (AFM) was performed to find the uniformity of graphene layers on the respective substrates. The microwave properties of these graphene layers were characterized by using microstrip line based measurement fixture. A simple and efficient de-embedding method has been adopted, which uses the propagation constants obtained from the measured S-parameters and the physical lengths of the material sample and microstrip line. The

results of effective relative permittivity, phase velocity and group velocity were compared with those obtained using standard ABCD de-embedding method in 10 MHz to 10 GHz. Transmission, dielectric and optical properties of as-grown bilayer graphene (BLG) on Cu and single layer graphene (SLG) transferred on glass and quartz have been studied and compared in frequency range of 10 MHz to 26.5 GHz. The intrinsic properties (complex relative permittivity and refractive index) were evaluated by using the conformal mapping formulas. In addition, the behaviour of waves in single layer and bilayer graphene were observed in terms of variations in phase velocity and group velocity. Finally the optical mass of photons is evaluated using wave-particle duality in SLG and BLG.

As a transparent conducting electrode (TCE), application of graphene was studied in silicon heterojunction solar cells. Two structures, TCO (ITO)/p-Gr/n-cSi/Ag and TCO (ITO)/n-Gr/p-cSi/Ag of graphene/silicon heterojunction cell have been simulated in AFORS-HET software to achieve highest efficiency solar cell. In the simulation for both structures, first the parameters of graphene layer was optimized and then later optimization for silicon layer was performed. We also obtained best possible efficiency in silicon heterojunction cells by using the parameters of commercial available silicon wafers too. In addition, spectral response, quantum efficiency and temperature dependence were studied for maximum simulation efficiency cells in both structures.

8.2 Conclusions

The work presented in this thesis contributes in increasing the knowledge base of graphene in the field of microwave and photovoltaic. The specific contributions of the work are summarized here:

(1) Raman spectroscopy has confirmed single layer graphene transferred on glass and quartz and bilayer graphene on Cu substrates. Performed atomic force microscopy reveals that graphene layers are nearly uniform on the respective substrates.

(2) The effective relative permittivity determined using adopted method has been found to be in well agreement with values obtained by using the standard de-embedding method based on ABCD parameters as percent errors were found less than 4 % and 1 % in the real and imaginary parts of effective relative permittivity, respectively. In addition, percent error less than 3 % in phase and group velocities further confirmed that our adopted method can be used for obtaining the dispersive behaviour of any material at the microwave frequency.

(3) The phase velocity was found to be reduced, while group velocity was increased on loading the microstrip line with graphene/glass and graphene/quartz compared to bare glass and quartz. For graphene/substrate, higher effective relative permittivity and group velocity suggest that the amount of anomalous dispersion has been increased and graphene absorbs the microwaves.

(4) In BLG, high phase velocity and group velocity represent faster propagation of energy and their relation suggests the linear dispersion than SLG. In addition, the lower effective mass of photons in BLG resulted owing to smaller refractive index, which in turn suggests minor interaction between photon-charge carriers.

(5) In simulation study of graphene/silicon heterojunction cells, the doping concentration, effective band densities, bandgap and electron affinity etc. are found to be the influential parameters of graphene and silicon, which controls the built-in voltage at the interface.

(6) After optimizing the parameters of both layers of graphene and silicon, an efficiency of 9.812% was achieved and an optimum efficiency of 11.47 % has been achieved

for 100 μm thick commercial silicon layer in p-graphene/n-cSi cells, whereas in n-graphene/p-cSi cells, simulation efficiency of 13.66 % was achieved and an optimum efficiency of 8.491 % has been achieved for commercial silicon of same thickness.

(7) The p-doped multilayer graphene as well as n-doped multilayer graphene is highly efficient to be used as a transparent conducting electrode in graphene/silicon heterojunction cell.

8.3 Future directions

To use the graphene as a substrate material in the passive microwave devices, synthesis of multilayer graphene and study of its physical properties are required. On obtaining the microwave properties of these graphene samples using the method discussed in this thesis, flexible passive microwave devices like power divider, filters etc. can be designed and fabricated on multilayer graphene sandwiched between Cu sheets. By using different metals other than Cu for multilayer graphene, components in other transmission line like coplanar waveguide can be explored, which may pave way to develop switchable phase shifter on changing the bias voltage across graphene layers.

For solar cell application, the synthesis of graphene layers is to be performed in order to obtain the multilayer graphene with the parameters as reported in this work. On pre-knowledge of silicon wafer parameters, cost effective solar cells can be made on silicon wafers of thickness < 100 μm by transferring the graphene layer with optimized parameters.

Appendix A

MATLAB program for S-parameter de-embedding

```
clc;
clear all;
prompt = {'Length of Microstrip Line in meter:','Characteristic
Impedance of line in ohm:','Length of Superstrate in meter:'};
dlg_title = 'Input';
num_lines = 1;
defaultans = {'0','0','0'};
answer = inputdlg(prompt,dlg_title,num_lines,defaultans);
l=str2num(answer{1});
zo=str2num(answer{2});
lsub=str2num(answer{3});

[filename, pathname]=uigetfile({'*.s2p'},'Select the s2p file');
p=read(rfckt.datafile,filename);
s=p.AnalyzedResult.S_Parameters;
freq=p.AnalyzedResult.freq;
[p, n, m]=size(s);

for i=1:1:m
    f=freq(i,:);
    Smat=s(:,:,i);

    k=(sqrt(((1+Smat(1,1)-Smat(2,2)-
Smat(2,2)*Smat(1,1)+Smat(2,1)*Smat(1,2))^2)-
(4*(Smat(2,1))^2)))/(2*Smat(2,1));
    GaS1=-1*log(((1+Smat(1,1)-Smat(2,2)-
Smat(2,2)*Smat(1,1)+Smat(2,1)*Smat(1,2))/(2*Smat(2,1)))+k);
    GaS2=-1*log(((1+Smat(1,1)-Smat(2,2)-
Smat(2,2)*Smat(1,1)+Smat(2,1)*Smat(1,2))/(2*Smat(2,1)))-k);
    if real(GaS1)<0
        Gamma2x=GaS2;
    elseif real(GaS2)<0
        Gamma2x=GaS1;
    end

    Zcs1=zo*sqrt((((1+Smat(1,1))*(1+Smat(2,2)))-
(Smat(1,2)*Smat(2,1)))/(((1-Smat(1,1))*(1-Smat(2,2)))-
(Smat(1,2)*Smat(2,1))));
    Zcs2=-1*zo*sqrt((((1+Smat(1,1))*(1+Smat(2,2)))-
(Smat(1,2)*Smat(2,1)))/(((1-Smat(1,1))*(1-Smat(2,2)))-
(Smat(1,2)*Smat(2,1))));

    if real(Zcs1)<0
        Zc2(i,:)=Zcs2;
    elseif real(Zcs2)<0
        Zc2(i,:)=Zcs1;
    end

    A_1st=cosh(Gamma2x*(1/lsub)*(lsub));
    B_1st=Zc2(i,:)*sinh(Gamma2x*(1/lsub)*(lsub));
    C_1st=(1/Zc2(i,:))*sinh(Gamma2x*(1/lsub)*(lsub));
    D_1st=cosh(Gamma2x*(1/lsub)*(lsub));
```

```matlab
    ABCD1st=[A_1st B_1st;C_1st D_1st];
    ABCD_Z=[1 0;0 1];

    ABCDmatn=((ABCD_Z)^(-1))*(ABCD1st)*((ABCD_Z)^(-1));
    Amatn=ABCDmatn(1,1);
    Bmatn=ABCDmatn(1,2);
    Cmatn=ABCDmatn(2,1);
    Dmatn=ABCDmatn(2,2);

    denmn=(Amatn+(Bmatn/zo)+(Cmatn*zo)+Dmatn);
    S11matn=(Amatn+(Bmatn/zo)-(Cmatn*zo)-Dmatn)/denmn;
    S12matn=(2*((Amatn*Dmatn)-(Bmatn*Cmatn)))/denmn;
    S21matn=2/denmn;
    S22matn=(-Amatn+(Bmatn/zo)-(Cmatn*zo)+Dmatn)/denmn;

    S11m(i,:)=S11matn;
    S21m(i,:)=S21matn;
    S22m(i,:)=S22matn;
    S12m(i,:)=S12matn;

    S_par(:,:,i)=[S11m(i,:) S12m(i,:);S21m(i,:) S22m(i,:)];
end
rfwrite(S_par,freq,'Deembedded_S_Parameter_DB.s2p','Format','DB');
rfwrite(S_par,freq,'Deembedded_S_Parameter_RealImaginary.s2p');
```

Appendix B

B1. MATLAB program for two-layer parameter extraction
(used for bilayer graphene)

```
clc;
clear ;
close all;

% pause(1);
disp('"Select s2p for substrate of microstrip line"');
% pause(1);
l=50.8;%mm
w=3.024;%mm
h=1.5;%mm
h2=2.*3.34e-7;%mm
er=4.5-0.009i;
err=4.5;
t=0.018;%mm

Zo=50;
c=3e8;%m/s
Muo=4*pi*1.0e-7;%H/m
pc=1.054e-34;% Planck constant

% %---------selection of s2p file for I layer--------------------
[filename, pathname]=uigetfile({'*.s2p'},'Select the s2p file');
p=read(rfckt.datafile,filename);
s=p.AnalyzedResult.S_Parameters;
freq=p.AnalyzedResult.freq;
[p, n ,m]=size(s);

s11=zeros(m,1);
s12=zeros(m,1);
s21=zeros(m,1);
s22=zeros(m,1);

q11=zeros(m,1);
q1r1=zeros(m,1);
q1i1=zeros(m,1);
Erefffr1=zeros(m,1);
Erefffi1=zeros(m,1);
er1r1=zeros(m,1);
er1i1=zeros(m,1);

    for i=1:1:m
    f1=freq(i,:);
    Spar=s(:,:,i);

        S11c=Spar(1,1);
        S21c=Spar(2,1);
        S12c=Spar(1,2);
        S22c=Spar(2,2);

        s11(i,:)=S11c;
        p11=real(s11);
        p11i=imag(s11);
```

```matlab
        s12(i,:)=S12c;
        p12=real(s12);
        p12i=imag(s12);

        s21(i,:)=S21c;
        p21=real(s21);
        p21i=imag(s21);

        s22(i,:)=S22c;
        p22=real(s22);
        p22i=imag(s22);


wef=w+(((2.*h)./pi).*log(17.08.*(((w./(2.*h)))+0.92)));%effective line
width

        q1=1-(0.5.*(log(((pi.*wef)./h)-1)./(wef./h)));
        q1r=real(q1);
        q1i=imag(q1);
        q11(i,:)=q1;
        q1r1(i,:)=q1r;
        q1i1(i,:)=q1i;

%-----------------Ereff(f) from  formula----------------------------
        f=(freq./(10.^9));
        fn=f.*h.*0.1;
        % fn=47.713*f.*h;
        u=w./h;
        % u=wef./h;
        ff=freq;
        p1=0.27488+u.*(0.6315+0.525./(1+0.157.*fn).^20)-
    0.065683.*exp(-    8.7513.*u);
        p2=0.33622.*(1-exp(-0.03442.*err));
        p3=0.0363.*exp(-4.6.*u).*(1-exp(-(fn./3.87).^4.97));
        p4=1+2.751.*(1-exp(-(err./15.916).^8));
        pf=p1.*p2.*((0.1844+p3.*p4).*10.*fn).^1.5763;
        eff=((err+1)./2)+((err-1)./2).*(1./(1+12.*(h./w)).^(0.5));
        % efff=er-((er-eff)./(1+pf));
        efff=er.*q1+(1-q1);
        Erefffr=real(efff);
        Erefffi=imag(efff);
        Erefffr1(i,:)=Erefffr;
        Erefffi1(i,:)=Erefffi;

         %-----------ER1from formula----------------------------
        no=120.*pi;
        u=w./h;
        f3=6+(((2.*pi)-6).*(exp(-(30.666./u).^(0.7528))));
     Zod=(no./(2.*pi.*sqrt(eff))).*(log((f3./u)+sqrt(1+(4./(u.^2)))));
        G22=0.6+(0.009.*Zod);

        Fn2=(2.*h.*f.*Muo)./Zo;
        % er1=((efff.*(1+(G2.*Fn2.^2)))-(0.5.*(1-(1+((12.*h)./w)).^-
0.5)))./(0.5.*(1+(1+((12.*h)./w)).^-0.5+(G2.*Fn2.^2)));

        % q22=1-q1;
        er1=((efff -1+q1)./q1);
```

```matlab
        er1r=real(er1);
        er1i=imag(er1);
        er1r1(i,:)=er1r;
        er1i1(i,:)=er1i;
end
%-----------------gamma alpha beta ---------------------------------
G1c1=acosh(sqrt((((1+s11).*(1-s22))+(s12.*s21))./(2.*s21)).*((((1-
s11).*(1+s22))+(s12.*s21))./(2.*s21))));
tan_g=tanh(G1c1);

A1=real(tan_g);
B1=imag(tan_g);
[theta,rho] = cart2pol(A1,B1);
alpha=(1./(2.*l)).*atanh((2.*A1)./(1+abs(rho).^2)); %Np/m
bet=(1./(2.*l)).*atan((2.*B1)./(1-abs(rho).^2));%/m
 %-----------------------------beta new---------------------------
bd1=(2.*l.*((2.*pi.*ff)./(3e8)).*(sqrt(efff)));
% bdr=real(bd1);
% bdi=imag(bd1);
% bcal=(1./(2.*l)).*atan((2.*(abs(imag(tan_g))))./(1-
abs(tan_g)).^2));%rad/mm
Bgpc1=((2.*imag(tan_g))./(1-(abs(tan_g)).^2));% no unit
kpc=ceil((((2.*l.*(bd1))-(atan(Bgpc1)))./180);
kpcr=real(kpc);
kpci=imag(kpc);

NeB=(((kpc.*180)+((atan(Bgpc1).*(180./pi))))./(2.*l))./(2.*l); %
deg/mm
NeB_rad1=((pi./180).*NeB);%rad/mm

x1=alpha;
y1=NeB;
yy1=NeB_rad1;

NeG1c1 = x1+1i.*y1;%deg
newgamma=x1+1i.*yy1;%rad

g=(2.*pi*ff)./c;
go=complex(0,g);
ef=((NeG1c1./go).^2);
efr=real(ef);
efi=imag(ef);

er11=((ef -1+q1)./q1);
er11r=real(er11);
er11i=imag(er11);

Zc1=Zo.*(sqrt((1+s11+s22+(s11.*s22)-(s12.*s21))./(1-s11-
s22+(s11.*s22)-(s12.*s21))));
if real(Zc1)<0
    Zc1=-Zc1;
else
    Zc1=1.*Zc1;
end
Zc=smooth(Zc1);

%-------------------------------------------------------------------
```

```
ereff_new=(NeG1c1./go)./(Zc./Zo);
ereff_newr=real(ereff_new);
ereff_newi=imag(ereff_new);


%------------------frequency from 1 to 499-------------------------
fr1=freq(1:1:m-1);
%---------Refractive Index----------------------------

N1=((sqrt((er11r).^2+(er11i).^2)+er11r)./2).^0.5;


%----------Extinction coefficient------------------------
K1=((sqrt((er11r).^2+(er11i).^2)-er11r)./2).^0.5;


%------------Phase Velocity----------------------------
vp1=c./N1;


%----------Group Velocity----------------------------
lambda01=c./freq;
y=vp1;
x=lambda01;
dydx_approx_for=diff(y)./diff(x);
dydx_approx_back=diff(y)./diff(x);
dydx_approx_gradient=gradient(y,x);
dydx_approx_for(length(x))=NaN;
% dydx_approx_back=[NaN, dydx_approx_back];


figure(5);
plot(x,dydx_approx_gradient);
legend('centre difference formula');
legend('Location','NorthEast');
xlabel('lambda 0');
ylabel('dvp/dl0');
grid on;


%---------------------------------
vg1=vp1-(lambda01.*(dydx_approx_gradient));


%----------------Effective electron mass----------------

% NeB_rad11=NeB_rad1(2:2:end-1);
M1=((pc.*(NeB_rad1.*1000))./vg1);
M1r=real(M1);
M1i=imag(M1);
%-------------------------------------------------------
figure(1);
plot(freq/(10^9),
Erefffr1,'blue',freq/(10^9),efr,'green',freq/(10^9));
legend('Ereff(f)1 formula ','Ereff(f)1 measured');
legend('Location','NorthWest');
xlabel('Frequency(GHz)');
ylabel('Effective Dielectric Constant 1');
title('Effective Dielectric Constsnt(Real) Vs. Frequency');
grid on;


figure(2);
plot(freq/(10^9),
Erefffi1,'blue',freq/(10^9),efi,'green',freq/(10^9));
legend('Ereff(f)1 formula ','Ereff(f)1 measured');
```

```matlab
legend('Location','NorthWest');
xlabel('Frequency(GHz)');
ylabel('Effective Dielectric Constant 1');
title('Effective Dielectric Constsnt(Imaginary) Vs. Frequency');
grid on;


figure(3);
plot(freq/(10^9),er1r1,'black',freq/(10^9),er11r,'-.black');
legend('Er1 formula ','Er1 measured');
legend('Location','NorthEast');
xlabel('Frequency(GHz)');
ylabel('Er1');
title('Er1 (Real)Vs. Frequency');
grid on;


figure(4);
plot(freq/(10^9),er1i1,'black',freq/(10^9),er11i,'-.black');
legend('Er1 formula ','Er1 measured');
legend('Location','NorthEast');
xlabel('Frequency(GHz)');
ylabel('Er1');
title('Er1 (Imaginary) Vs. Frequency');
grid on;


figure(6);
plot(freq/(10^9),vp1);
xlabel('Frequency(GHz)');
ylabel('vp1(m/s)');
title('Phase Velocity Vs. Frequency ');
grid on;


figure(7);
plot(freq./(10^9),vg1);
xlabel('Frequency(GHz)');
ylabel('vg1 (m/s)');
title('Group Velocity Vs. Frequency ');
grid on;



%------------II layer----------------------------
pause(1);
disp('"Select s2p for superstrate 1 of microstrip line"');
pause(1);
[filename1, pathname1]=uigetfile({'*.s2p'},'Select the s2p file');
p1=read(rfckt.datafile,filename);
s1=p1.AnalyzedResult.S_Parameters;
freq2=p1.AnalyzedResult.freq;

[pp, n1 ,m1]=size(s1);
ss11=zeros(m1,1);
ss12=zeros(m1,1);
ss21=zeros(m1,1);
ss22=zeros(m1,1);

q11=zeros(m1,1);
q1r1=zeros(m1,1);
q1i1=zeros(m1,1);
```

```
q22=zeros(m1,1);
q2r1=zeros(m1,1);
q2i1=zeros(m1,1);

q32=zeros(m1,1);
q32r1=zeros(m1,1);
q32i1=zeros(m1,1);
efff2r1=zeros(m1,1);
efff2i1=zeros(m1,1);
er2r1=zeros(m1,1);
er2i1=zeros(m1,1);

    for i=1:1:m1
    f1=freq2(i,:);
    Spar=s1(:,:,i);

        S11c=Spar(1,1);
        S21c=Spar(2,1);
        S12c=Spar(1,2);
        S22c=Spar(2,2);

        ss11(i,:)=S11c;
        p11=real(ss11);
        p11i=imag(ss11);

        ss12(i,:)=S12c;
        p12=real(ss12);
        p12i=imag(ss12);

        ss21(i,:)=S21c;
        p21=real(ss21);
        p21i=imag(ss21);

        ss22(i,:)=S22c;
        p22=real(ss22);
        p22i=imag(ss22);

        H2=(h+h2)./h;

wef=w+(((2.*h)./pi).*log(17.08.*(((w./(2.*h)))+0.92)));%effective
line width
        v2=((2.*h)./pi).*atan((2.*pi.*(H2*h-h)./(pi.*wef-
4.*h)));%quantity v2

        xx=(v2.*pi)./(2.*h);

        q1=1-(0.5.*(log(((pi.*wef)./h)-1)./(wef./h)));
        q1r=real(q1);
        q1i=imag(q1);
        q11(i,:)=q1;
        q1r1(i,:)=q1r;
        q1i1(i,:)=q1i;


        q2=1-q1;
%        q2=1-q1-(0.5.*((h-
v2)./wef).*log((2.*wef).*cos(xx)./(2.*H2.*h-h+v2)+sin(xx)));
        q2r=real(q2);
        q2i=imag(q2);
```

```
        q22(i,:)=q2;
        q2r1(i,:)=q2r;
        q2i1(i,:)=q2i;

        ng=2.7-1.3i;
        ngr=real(ng);
        ngi=imag(ng);


        er21=((ng)^2);
        efff2=(er1.*q1)+(er21.*q2);
        efff2r=real(efff2);
        efff2i=imag(efff2);
        efff2r1(i,:)=efff2r;
        efff2i1(i,:)=efff2i;


        er2=(efff2./q2-(q1.*er1)./q2);
        er2r=real(er2);
        er2i=imag(er2);
        er2r1(i,:)=er2r;
        er2i1(i,:)=er2i;

    end
%--------------------------------------------------------------------

%----------------gamma alpha beta --------------------------------
G2=acosh(sqrt((((1+ss11).*(1-ss22))+(ss12.*ss21))./(2.*ss21)).*((((1-
ss11).*(1+ss22))+(ss12.*ss21))./(2.*ss21)))));
t_g=tanh(G2);

A2=real(t_g);
B2=imag(t_g);
[thet,rh] = cart2pol(A2,B2);
alpha2=(1./(2.*l)).*atanh((2.*A2)./(1+abs(rh).^2)); %Np/m
bet2=(1./(2.*l)).*atan((2.*B2)./(1-abs(rh).^2));%/m
%----------------------------beta new----------------------------
bd2=(2.*l.*((2.*pi.*freq2)./(3e8)).*(sqrt((efff2))));
Bgpc2=((2.*imag(t_g))./(1-(abs(t_g)).^2));% no unit
k=ceil(((2.*l.*(bd2))-(atan(Bgpc2)))./180);
kr=real(k);
ki=imag(k);

NB=(((k.*180)+((atan(Bgpc2).*(180./pi)))))./(2.*l))./(2.*l); % deg/mm
NeB_rad2=((pi./180).*NB);%rad/mm

x2=alpha2;
y2=NB;
yy2=NeB_rad2;

NeG1c2 = x2+1i.*y2;%deg
% newgamma2=x2+1i.*yy2;%rad


%--------------------------Zc-------------------------------------
---
Zc11=Zo.*(sqrt((1+ss11+ss22+(ss11.*ss22)-(ss12.*ss21))./(1-ss11-
ss22+(ss11.*ss22)-(ss12.*ss21)))));
if real(Zc11)<0
```

```matlab
    Zc11=-Zc11;
else
    Zc11=1.*Zc11;
end
Zc2=smooth(Zc11);


%-----------------------------------------------------------------------
-
% g1=(2.*pi)./((3e8)./ff);
% go1=complex(0,g1);
ef2=((NeG1c2./go).^2);
ef2r=real(ef2);
ef2i=imag(ef2);

er22=(ef2./q2-(q1.*er11)./q2);
er22r=real(er22);
er22i=imag(er22);


%-----------------------------------------------------------------------
-
ereff_new2=(NeG1c2./go)./(Zc2./Zo);



%------------------frequency from 1 to 499------------------------
fr2=freq2(1:1:m1-1);
%----------Refractive Index------------------------------

N2=((sqrt((er22r).^2+(er22i).^2)+er22r)./2).^0.5;

%-----------Extinction coefficient------------------------
K2=((sqrt((er22r).^2+(er22i).^2)-er22r)./2).^0.5;

%-------------Phase Velocity------------------------------
vp2=c./N2;

%----------Group Velocity----------------------------
lambda02=c./(freq2.*er22r);
y1=vp2;
x1=lambda02;
dydx_approx_for1=diff(y1)./diff(x1);
dydx_approx_back1=diff(y1)./diff(x1);
dydx_approx_gradient1=gradient(y1,x1);
dydx_approx_for1(length(x1))=NaN;
% dydx_approx_back=[NaN, dydx_approx_back];

figure(8);
plot(x1,dydx_approx_gradient1);
legend('centre difference formula');
legend('Location','NorthEast');
xlabel('lambda 0');
ylabel('dvp/dl0');
grid on;

vg2=vp2-(lambda02.*(dydx_approx_gradient1));



%-----------------Effective electron mass----------------
```

157

```
kgraphene=(2.*pi./lambda02);
M2=((pc.*(kgraphene.*1000))./vg2);


M2r=real(M2);
M2i=imag(M2);

figure(9);
plot(freq2/(10^9),ef2r,'blue',freq2/(10^9),efff2r1,'green',freq2/(10^9
));
legend('Efff(f) measured','Efff(f) formula');
legend('Location','NorthEast');
xlabel('Frequency(GHz)');
ylabel('Efff 2(f) real');
title('Efff 2(f) real Vs. Frequency ');
grid on;

figure(10);
plot(freq2/(10^9),ef2i,'blue',freq2/(10^9),efff2i1,'green',freq2/(10^9
));
legend('Efff(f) measured','Efff(f) formula');
legend('Location','NorthEast');
xlabel('Frequency(GHz)');
ylabel('Efff 2(f) imaginary');
title('Efff 2(f) imaginary Vs. Frequency ');
grid on;

figure(11);
plot(freq2/(10^9),er22r,'black',freq2/(10^9),er2r1,'-.black');
legend('Er2 measured','Er2 formula');
legend('Location','NorthEast');
xlabel('Frequency(GHz)');
ylabel('Er2 real');
title('Er2 Vs. Frequency ');
grid on;

figure(12);
plot(freq2/(10^9),er22i,'black',freq2/(10^9),er2i1,'-.black');
legend('Er2 measured','Er2 formula');
legend('Location','NorthEast');
xlabel('Frequency(GHz)');
ylabel('Er2 imaginary');
title('Er2 imaginary Vs. Frequency ');
grid on;

figure(13);
plot(freq2/(10^9),alpha2,'black',freq2/(10^9),NB,'-
.red',freq2/(10^9),NeB_rad2,'-.blue' );
legend('alpha2 ','NB real', 'NeB_rad2');
legend('Location','NorthEast');
xlabel('Frequency(GHz)');
ylabel('Gamma');
title('Gamma Vs. Frequency for II layer ');
grid on;

figure(14);
plot(freq2/(10^9),q1r1,'black',freq2/(10^9),q1i1,'-.black');
legend('q1 real ','q1 imag');
legend('Location','NorthEast');
```

```
xlabel('Frequency(GHz)');
ylabel('q1');
title('q1 Vs. Frequency ');
grid on;

figure(15);
plot(freq2/(10^9),q2r1,'black',freq2/(10^9),q2i1,'-.black');
legend('q2 real ','q2 imag');
legend('Location','NorthEast');
xlabel('Frequency(GHz)');
ylabel('q2');
title('q2 Vs. Frequency ');
grid on;

figure(16);
plot(freq2/(10^9),N2);
xlabel('Frequency(GHz)');
ylabel('n2');
title('n2 Vs. Frequency ');
grid on;

figure(17);
plot(freq2/(10^9),K2);
xlabel('Frequency(GHz)');
ylabel('k2');
title('k2 Vs. Frequency ');
grid on;

figure(18);
plot(freq2/(10^9),vp2);
xlabel('Frequency(GHz)');
ylabel('vp2(m/s)');
title('Phase Velocity Vs. Frequency ');
grid on;

figure(19);
plot(freq2./(10^9),vg2);
xlabel('Frequency(GHz)');
ylabel('vg2 (m/s)');
title('Group Velocity Vs. Frequency ');
grid on;

figure(20);
plot(freq2./(10^9),M2r,'red');
legend('m2 real');
legend('Location','NorthEast');
xlabel('Frequency(GHz)');
ylabel('m2 (kg)');
title('Effective electron mass Vs. Frequency ');
grid on;

file_2=[freq2/(10^9) ef2r ef2i efff2r1 efff2i1 er11r er11i er1r1 er1i1
er22r er22i er2r1 er2i1 q1r1 q1i1 q2r1 q2i1 N2 K2 vp2  ];
E_2 = {'Frequency(GHz)','Eff2(f) measured real','Eff2(f) measured
imag','Eff2(f) formula real','Eff2(f) formula imag','Er1 measured
real','Er1 measured imag','Er1 formula real','Er1 formula imag','Er2
measured real','Er2 measured imag','Er2 formula real','Er2 formula
imag','q1 real','q1 imag','q2 real','q2 imag','Refractive
index','Extinction coeff.','Phase velocity (m/s)'};
```

159

```
xlswrite('Results for second layer microstrip line.xlsx',E_2,1,'A1');
xlswrite('Results for second layer microstrip
line.xlsx',file_2,1,'A2');


file_22=[freq2/(10^9) vg2 M2r M2i ];
E_22 = {'Frequency(GHz)','Group Velocity (m/s)','Effective electron
mass (kg)real','Effective electron mass (kg)imag'};
xlswrite('Group Velocity and Effective electron mass for second layer
microstrip line.xlsx',E_22,1,'A1');
xlswrite('Group Velocity and Effective electron mass for second layer
microstrip line.xlsx',file_22,1,'A2');
```

B2. MATLAB program for three-layer parameter extraction (used for single layer graphene)

```
clc;
clear ;
close all;

% pause(1);
disp('"Select s2p for substrate of microstrip line"');
% pause(1);
l=50.8;%mm
w=3.024;%mm
h=1.5;%mm
h2=0.7;%mm
h3=3.34e-7;%mm
er=4.5-0.009i;
err=4.5;
t=0.018;%mm

Zo=50;
c=3e8;%m/s
Muo=4*pi*1.0e-7;%H/m
pc=1.054e-34;% Planck constant

% %---------selection of s2p file for I layer--------------------
[filename, pathname]=uigetfile({'*.s2p'},'Select the s2p file');
p=read(rfckt.datafile,filename);
s=p.AnalyzedResult.S_Parameters;
freq=p.AnalyzedResult.freq;
[p, n ,m]=size(s);

s11=zeros(m,1);
s12=zeros(m,1);
s21=zeros(m,1);
s22=zeros(m,1);

q11=zeros(m,1);
q1r1=zeros(m,1);
q1i1=zeros(m,1);
Erefffr1=zeros(m,1);
Erefffi1=zeros(m,1);
 er1r1=zeros(m,1);
 er1i1=zeros(m,1);


    for i=1:1:m
    f1=freq(i,:);
    Spar=s(:,:,i);

        S11c=Spar(1,1);
        S21c=Spar(2,1);
        S12c=Spar(1,2);
        S22c=Spar(2,2);

        s11(i,:)=S11c;
        p11=real(s11);
```

```
        p11i=imag(s11);

        s12(i,:)=S12c;
        p12=real(s12);
        p12i=imag(s12);

        s21(i,:)=S21c;
        p21=real(s21);
        p21i=imag(s21);

        s22(i,:)=S22c;
        p22=real(s22);
        p22i=imag(s22);


wef=w+(((2.*h)./pi).*log(17.08.*(((w./(2.*h)))+0.92)));%effective line
width

        q1=1-(0.5.*(log(((pi.*wef)./h)-1)./(wef./h)));
        q1r=real(q1);
        q1i=imag(q1);
        q11(i,:)=q1;
        q1r1(i,:)=q1r;
        q1i1(i,:)=q1i;


    %-----------------Ereff(f) from  formula-------------------------
-----
        f=(freq./(10.^9));
        fn=f.*h.*0.1;
        % fn=47.713*f.*h;
        u=w./h;
        % u=wef./h;
        ff=freq;
        p1=0.27488+u.*(0.6315+0.525./(1+0.157.*fn).^20)-
0.065683.*exp(-8.7513.*u);
        p2=0.33622.*(1-exp(-0.03442.*err));
        p3=0.0363.*exp(-4.6.*u).*(1-exp(-(fn./3.87).^4.97));
        p4=1+2.751.*(1-exp(-(err./15.916).^8));
        pf=p1.*p2.*((0.1844+p3.*p4).*10.*fn).^1.5763;
        eff=((err+1)./2)+((err-1)./2).*(1./(1+12.*(h./w)).^(0.5));
        efff=er.*q1+(1-q1);
        Erefffr=real(efff);
        Erefffi=imag(efff);
        Erefffr1(i,:)=Erefffr;
        Erefffi1(i,:)=Erefffi;

        %------------ER1from formula----------------------------
        no=120.*pi;
        u=w./h;
        f3=6+(((2.*pi)-6).*(exp(-(30.666./u).^(0.7528))));

Zod=(no./(2.*pi.*sqrt(eff))).*(log((f3./u)+sqrt(1+(4./(u.^2)))));
        G22=0.6+(0.009.*Zod);

        Fn2=(2.*h.*f.*Muo)./Zo;
        % er1=((efff.*(1+(G2.*Fn2.^2)))-(0.5.*(1-(1+((12.*h)./w)).^-
0.5)))./(0.5.*(1+(1+((12.*h)./w)).^-0.5+(G2.*Fn2.^2)));
```

```matlab
        er1=((efff -1+q1)./q1);
         er1r=real(er1);
         er1i=imag(er1);

        er1r1(i,:)=er1r;
        er1i1(i,:)=er1i;
end
%----------------gamma alpha beta ----------------------------------
--------
G1c1=acosh(sqrt((((((1+s11).*(1-s22))+(s12.*s21))./(2.*s21)).*((((1-
s11).*(1+s22))+(s12.*s21))./(2.*s21)))));
tan_g=tanh(G1c1);

A1=real(tan_g);
B1=imag(tan_g);
[theta,rho] = cart2pol(A1,B1);
alpha=(1./(2.*l)).*atanh((2.*A1)./(1+abs(rho).^2)); %Np/m
bet=(1./(2.*l)).*atan((2.*B1)./(1-abs(rho).^2));%/m
 %----------------------------beta new--------------------------
bd1=(2.*l.*((2.*pi.*ff)./(3e8)).*(sqrt(efff)));
Bgpc1=((2.*imag(tan_g))./(1-(abs(tan_g)).^2));% no unit
kpc=ceil(((2.*l.*(bd1))-(atan(Bgpc1)))./180);
kpcr=real(kpc);
kpci=imag(kpc);

NeB=(((kpc.*180)+((atan(Bgpc1).*(180./pi))))./(2.*l))./(2.*l); %
deg/mm
NeB_rad1=((pi./180).*NeB);%rad/mm

x1=alpha;
y1=NeB;
yy1=NeB_rad1;

NeG1c1 = x1+1i.*y1;%deg
newgamma=x1+1i.*yy1;%rad

g=(2.*pi*ff)./c;
go=complex(0,g);
ef=((NeG1c1./go).^2);
efr=real(ef);
efi=imag(ef);

er11=((ef -1+q1)./q1);
er11r=real(er11);
er11i=imag(er11);

Zc1=Zo.*(sqrt((1+s11+s22+(s11.*s22)-(s12.*s21))./(1-s11-
s22+(s11.*s22)-(s12.*s21))));
if real(Zc1)<0
    Zc1=-Zc1;
else
    Zc1=1.*Zc1;
end
Zc=smooth(Zc1);

%-------------------------------------------------------------------
----
```

```matlab
ereff_new=(NeG1c1./go)./(Zc./Zo);
ereff_newr=real(ereff_new);
ereff_newi=imag(ereff_new);


%-----------------------------------------------------------
%------------------frequency from 1 to 499--------------------------
-------
fr1=freq(1:1:m-1);
%----------Refractive Index----------------------------

N1=((sqrt((er11r).^2+(er11i).^2)+er11r)./2).^0.5;

%-----------Extinction coefficient------------------------
K1=((sqrt((er11r).^2+(er11i).^2)-er11r)./2).^0.5;

%-------------Phase Velocity-------------------------------
vp1=c./N1;

%----------Group Velocity-----------------------------
lambda01=c./freq;

y=vp1;
x=lambda01;
dydx_approx_for=diff(y)./diff(x);
dydx_approx_back=diff(y)./diff(x);
dydx_approx_gradient=gradient(y,x);
dydx_approx_for(length(x))=NaN;
% dydx_approx_back=[NaN, dydx_approx_back];

figure(1);
plot(x,dydx_approx_gradient);
legend('centre difference formula');
legend('Location','NorthEast');
xlabel('lambda 0');
ylabel('dvp/dl0');
grid on;
vg1=vp1-(lambda01.*(dydx_approx_gradient));

%------------------Effective electron mass----------------

M1=((pc.*(NeB_rad1.*1000))./vg1);
M1r=real(M1);
M1i=imag(M1);
%-----------------------------------------------------------

%-----------II layer---------------------------
pause(1);
disp('"Select s2p for superstrate 1 of microstrip line"');
pause(1);
[filename1, pathname1]=uigetfile({'*.s2p'},'Select the s2p file');
p1=read(rfckt.datafile,filename);
s1=p1.AnalyzedResult.S_Parameters;
freq2=p1.AnalyzedResult.freq;

[pp, n1 ,m1]=size(s1);
ss11=zeros(m1,1);
ss12=zeros(m1,1);
ss21=zeros(m1,1);
```

```
ss22=zeros(m1,1);

q11=zeros(m1,1);
q1r1=zeros(m1,1);
q1i1=zeros(m1,1);

q22=zeros(m1,1);
q2r1=zeros(m1,1);
q2i1=zeros(m1,1);

q32=zeros(m1,1);
q32r1=zeros(m1,1);
q32i1=zeros(m1,1);

 efff2r1=zeros(m1,1);
 efff2i1=zeros(m1,1);

 er2r1=zeros(m1,1);
 er2i1=zeros(m1,1);

    for i=1:1:m1
    f1=freq2(i,:);
    Spar=s1(:,:,i);

        S11c=Spar(1,1);
        S21c=Spar(2,1);
        S12c=Spar(1,2);
        S22c=Spar(2,2);

        ss11(i,:)=S11c;
        p11=real(ss11);
        p11i=imag(ss11);

        ss12(i,:)=S12c;
        p12=real(ss12);
        p12i=imag(ss12);

        ss21(i,:)=S21c;
        p21=real(ss21);
        p21i=imag(ss21);

        ss22(i,:)=S22c;
        p22=real(ss22);
        p22i=imag(ss22);

        H2=(h+h2)./h;

wef=w+(((2.*h)./pi).*log(17.08.*(((w./(2.*h)))+0.92)));%effective line
width
        v2=((2.*h)./pi).*atan((2.*pi.*(H2*h-h)./(pi.*wef-
4.*h)));%quantity v2

        xx=(v2.*pi)./(2.*h);

        q1=1-(0.5.*(log(((pi.*wef)./h)-1)./(wef./h)));
        q1r=real(q1);
        q1i=imag(q1);
```

```matlab
        q11(i,:)=q1;
        q1r1(i,:)=q1r;
        q1i1(i,:)=q1i;

        q2=1-q1-(0.5.*((h-v2)./wef).*log((2.*wef)./(2.*H2.*h-
h+v2).*cos(xx)+sin(xx)));
        q2r=real(q2);
        q2i=imag(q2);
        q22(i,:)=q2;
        q2r1(i,:)=q2r;
        q2i1(i,:)=q2i;

        q32=1-q1-q2;
        q32r=real(q32);
        q32i=imag(q32);
        q32(i,:)=q32;
        q32r1(i,:)=q32r;
        q32i1(i,:)=q32i;


        % er21r=5.27@100kHz;Corning Eagle glass
        % tandel=0.001 @100kHz;
        er21=5.27-0.005i;

        % efff2=(er1.*q1)+(er21.*q2);
        efff2=(er1.*q1)+((er21.*((1-q1).^2)./((er21.*(1-q1-q2))+q2)));
        efff2r=real(efff2);
        efff2i=imag(efff2);
        efff2r1(i,:)=efff2r;
        efff2i1(i,:)=efff2i;

        er2=((er1.*q1.*q2)-(efff2.*q2))./((efff2.*(1-q1-q2))-
(er1.*q1.*(1-q1-q2))-(1-q1).^2);
        er2r=real(er2);
        er2i=imag(er2);
        er2r1(i,:)=er2r;
        er2i1(i,:)=er2i;

    end
%-----------------gamma alpha beta --------------------------------
--------
G2=acosh(sqrt((((((1+ss11).*(1-ss22))+(ss12.*ss21))./(2.*ss21)).*((((1-
ss11).*(1+ss22))+(ss12.*ss21))./(2.*ss21)))));
t_g=tanh(G2);

A2=real(t_g);
B2=imag(t_g);
[thet,rh] = cart2pol(A2,B2);
alpha2=(1./(2.*l)).*atanh((2.*A2)./(1+abs(rh).^2));%Np/m
bet2=(1./(2.*l)).*atan((2.*B2)./(1-abs(rh).^2));%/m
%------------------------------beta new--------------------------
bd2=(2.*l.*((2.*pi.*freq2)./(3e8)).*(sqrt(efff2)));
Bgpc2=((2.*imag(t_g))./(1-(abs(t_g).^2)));% no unit
k=ceil(((2.*l.*(bd2))-(atan(Bgpc2)))./180);
kr=real(k);
ki=imag(k);
```

```matlab
NB=(((k.*180)+((atan(Bgpc2).*(180./pi))))./(2.*l))./(2.*l); % deg/mm
NeB_rad2=((pi./180).*NB);%rad/mm


x2=alpha2;
y2=NB;
yy2=NeB_rad2;


NeG1c2 = x2+1i.*y2;%deg
% newgamma2=x2+1i.*yy2;%rad


%------------------------Zc-----------------------------------
---
Zc11=Zo.*(sqrt((1+ss11+ss22+(ss11.*ss22)-(ss12.*ss21))./(1-ss11-
ss22+(ss11.*ss22)-(ss12.*ss21)))));
if real(Zc11)<0
    Zc11=-Zc11;
else
    Zc11=1.*Zc11;
end
Zc2=smooth(Zc11);


%-------------------------------------------------------------
-
g1=(2.*pi)./((3e8)./ff);
go1=complex(0,g1);
ef2=((NeG1c2./go1).^2);
ef2r=real(ef2);
ef2i=imag(ef2);


er22=((er11.*q1.*q2)-(ef2.*q2))./((ef2.*(1-q1-q2))-(er11.*q1.*(1-q1-
q2))-(1-q1).^2);
er22r=real(er22);
er22i=imag(er22);


%-------------------------------------------------------------
-
ereff_new2=(NeG1c2./go)./(Zc2./Zo);



%------------------frequency from 1 to 499------------------------
fr2=freq2(1:1:m1-1);
%---------Refractive Index------------------------------

N2=((sqrt((er22r).^2+(er22i).^2)+er22r)./2).^0.5;

%----------Extinction coefficient-----------------------
K2=((sqrt((er22r).^2+(er22i).^2)-er22r)./2).^0.5;


%-----------Phase Velocity-----------------------------
vp2=c./N2;

%---------Group Velocity---------------------------
lambda02=c./freq2;
y1=vp2;
x1=lambda02;
dydx_approx_for1=diff(y1)./diff(x1);
```

```
dydx_approx_back1=diff(y1)./diff(x1);
dydx_approx_gradient1=gradient(y1,x1);
dydx_approx_for1(length(x1))=NaN;
% dydx_approx_back=[NaN, dydx_approx_back];


figure(2);
plot(x1,dydx_approx_gradient1);
legend('centre difference formula');
legend('Location','NorthEast');
xlabel('lambda 0');
ylabel('dvp/dl0');
grid on;



vg2=vp2-(lambda02.*(dydx_approx_gradient1));

%----------------Effective electron mass----------------

% NeB_rad22=NeB_rad2(2:2:end-1);
M2=((pc.*(NeB_rad2.*1000))./vg2);
M2r=real(M2);
M2i=imag(M2);

% figure(3);
%
plot(freq2/(10^9),ef2r,'blue',freq2/(10^9),efff2r1,'green',freq2/(10^9
));
% legend('Efff(f) measured','Efff(f) formula');
% % plot(freq2/(10^9),ef2r,'blue',freq2/(10^9),efff2r,'green');
% % legend('Efff(f) measured','Efff(f) formula');
% legend('Location','NorthEast');
% xlabel('Frequency(GHz)');
% ylabel('Efff 2(f) real');
% title('Efff 2(f) real Vs. Frequency ');
% grid on;
%
% figure(4);
%
plot(freq2/(10^9),ef2i,'blue',freq2/(10^9),efff2i1,'green',freq2/(10^9
));
% legend('Efff(f) measured','Efff(f) formula');
% % plot(freq2/(10^9),ef2i,'blue',freq2/(10^9),efff2i,'green');
% % legend('Efff(f) measured','Efff(f) formula')
% legend('Location','NorthEast');
% xlabel('Frequency(GHz)');
% ylabel('Efff 2(f) imaginary');
% title('Efff 2(f) imaginary Vs. Frequency ');
% grid on;
%
% figure(5);
% plot(freq2/(10^9),er22r,'black',freq2/(10^9),er2r1,'-.black');
% legend('Er2 measured','Er2 formula');
% legend('Location','NorthEast');
% xlabel('Frequency(GHz)');
% ylabel('Er2 real');
% title('Er2 Vs. Frequency ');
% grid on;
%
% figure(6);
```

168

```matlab
% plot(freq2/(10^9),er22i,'black',freq2/(10^9),er2i1,'-.black');
% legend('Er2 measured','Er2 formula');
% legend('Location','NorthEast');
% xlabel('Frequency(GHz)');
% ylabel('Er2 imaginary');
% title('Er2 imaginary Vs. Frequency ');
% grid on;
%
% figure(7);
% plot(freq2/(10^9),kr,'black',freq2/(10^9),ki,'-.red');
% legend('k real ','k imag');
% legend('Location','NorthEast');
% xlabel('Frequency(GHz)');
% ylabel('k');
% title('k Vs. Frequency for II layer ');
% grid on;
%
% figure(8);
% plot(freq2/(10^9),alpha2,'black',freq2/(10^9),NB,'-
.red',freq2/(10^9),NeB_rad2,'-.blue' );
% legend('alpha2 ','NB real', 'NeB_rad2');
% legend('Location','NorthEast');
% xlabel('Frequency(GHz)');
% ylabel('Gamma');
% title('Gamma Vs. Frequency for II layer ');
% grid on;
% %
%
% figure(9);
%
% plot(freq2/(10^9),q1r1,'black',freq2/(10^9),q1i1,'-.black');
% legend('q1 real ','q1 imag');
% legend('Location','NorthEast');
% xlabel('Frequency(GHz)');
% ylabel('q1');
% title('q1 Vs. Frequency ');
% grid on;
%
% figure(10);
%
% plot(freq2/(10^9),q2r1,'black',freq2/(10^9),q2i1,'-.black');
% legend('q2 real ','q2 imag');
% legend('Location','NorthEast');
% xlabel('Frequency(GHz)');
% ylabel('q2');
% title('q2 Vs. Frequency ');
% grid on;
%
% % figure(11);
% % plot(freq2/(10^9),N2);
% % xlabel('Frequency(GHz)');
% % ylabel('n2');
% % title('n2 Vs. Frequency ');
% % grid on;
% %
% % figure(12);
% % plot(freq2/(10^9),K2);
% % xlabel('Frequency(GHz)');
% % ylabel('k2');
% % title('k2 Vs. Frequency ');
```

```matlab
% % grid on;
% %
% figure(13);
% plot(freq2/(10^9),vp2);
% xlabel('Frequency(GHz)');
% ylabel('vp2(m/s)');
% title('Phase Velocity Vs. Frequency ');
% grid on;
%
% figure(14);
% plot(freq2./(10^9),vg2);
% xlabel('Frequency(GHz)');
% ylabel('vg2 (m/s)');
% title('Group Velocity Vs. Frequency ');
% grid on;
%
% figure(15);
% plot(freq2./(10^9),M2r,'red');
% legend('m2 real');
% legend('Location','NorthEast');
% xlabel('Frequency(GHz)');
% ylabel('m2 (kg)');
% title('Effective electron mass Vs. Frequency ');
% grid on;
%


% file_2=[freq2/(10^9) ef2r ef2i efff2r1 efff2i1 er11r er11i er1r1
er1i1 er22r er22i er2r1 er2i1 q1r1 q1i1 q2r1 q2i1 N2 K2 vp2  ];
% E_2 = {'Frequency(GHz)','Eff2(f) measured real','Eff2(f) measured
imag','Eff2(f) formula real','Eff2(f) formula imag','Er1 measured
real','Er1 measured imag','Er1 formula real','Er1 formula imag','Er2
measured real','Er2 measured imag','Er2 formula real','Er2 formula
imag','q1 real','q1 imag','q2 real','q2 imag','Refractive
index','Extinction coeff.','Phase velocity (m/s)'};

% xlswrite('Results for second layer microstrip
line.xlsx',E_2,1,'A1');
% xlswrite('Results for second layer microstrip
line.xlsx',file_2,1,'A2');
%
% file_22=[freq2/(10^9) vg2 M2r M2i ];
% E_22 = {'Frequency(GHz)','Group Velocity (m/s)','Effective electron
mass (kg)real','Effective electron mass (kg)imag'};
% xlswrite('Group Velocity and Effective electron mass for second
layer microstrip line.xlsx',E_22,1,'A1');
% xlswrite('Group Velocity and Effective electron mass for second
layer microstrip line.xlsx',file_22,1,'A2');


% %------------III layer----------------------------
pause(1);
disp('"Select s2p for superstrate 2 of microstrip line"');
pause(1);
[filename2, pathname2]=uigetfile({'*.s2p'},'Select the s2p file');
p2=read(rfckt.datafile,filename);
s2=p2.AnalyzedResult.S_Parameters;
freq3=p2.AnalyzedResult.freq;
[ppp, n2 ,m2]=size(s2);
```

```
        sss11=zeros(m2,1);
        sss12=zeros(m2,1);
        sss21=zeros(m2,1);
        sss22=zeros(m2,1);


        q11=zeros(m2,1);
        q1r1=zeros(m2,1);
        q1i1=zeros(m2,1);


        q22=zeros(m2,1);
        q2r1=zeros(m2,1);
        q2i1=zeros(m2,1);


        q33=zeros(m2,1);
        q3r1=zeros(m2,1);
        q3i1=zeros(m2,1);


        q44=zeros(m2,1);
        q4r1=zeros(m2,1);
        q4i1=zeros(m2,1);


        efff3r1=zeros(m2,1);
        efff3i1=zeros(m2,1);

        er3r1=zeros(m2,1);
        er3i1=zeros(m2,1);



            for i=1:1:m2
            f1=freq3(i,:);
            Spar=s2(:,:,i);

                S11c=Spar(1,1);
                S21c=Spar(2,1);
                S12c=Spar(1,2);
                S22c=Spar(2,2);

                sss11(i,:)=S11c;
                p11=real(sss11);
                p11i=imag(sss11);

                sss12(i,:)=S12c;
                p12=real(sss12);
                p12i=imag(sss12);

                sss21(i,:)=S21c;
                p21=real(sss21);
                p21i=imag(sss21);

                sss22(i,:)=S22c;
                p22=real(sss22);
                p22i=imag(sss22);

%----------------single layer filling factor----------------
                H1=h./h;
                q1=1-(0.5.*(log(((pi.*wef)./h)-1)./(wef./h)));
                q1r=real(q1);
```

```
        q1i=imag(q1);
        q11(i,:)=q1;
        q1r1(i,:)=q1r;
        q1i1(i,:)=q1i;
%----------------double layer filling factor----------------
        H2=(h+h2)./h;

wef=w+(((2.*h)./pi).*log(17.08.*(((w./(2.*h)))+0.92)));%effective line
width
        v2=((2.*h)./pi).*atan((2.*pi.*(H2*h-h)./(pi.*wef-
4.*h)));%quantity v2
        v22=v2./h;

        xx=(v2.*pi)./(2.*h);

        q2=1-q1-(0.5.*((h-v2)./wef).*log((2.*wef).*cos(xx)./(2.*H2.*h-
h+v2)+sin(xx)));
        q2r=real(q2);
        q2i=imag(q2);
        q22(i,:)=q2;
        q2r1(i,:)=q2r;
        q2i1(i,:)=q2i;


%---------------- three layer filling factor----------------
        H3=(h+h2+h3)./h;
        wefn=wef/h;
        v3=((2.*h)./pi).*atan((2.*pi.*h.*(H3-1)./(pi.*wef-
4.*h)));%quantity v3
        vn3=v3/h;
        xxx=(v3.*pi)./(2.*h);

        q3=1-q1-q2-(0.5.*((h-
v3)./wef).*log((2.*wef).*cos(xxx)./(2.*H3.*h-h+v3)+sin(xxx)));
        q3r=real(q3);
        q3i=imag(q3);
        q33(i,:)=q3;
        q3r1(i,:)=q3r;
        q3i1(i,:)=q3i;

        q4=1-q1-q2-q3;
        q4r=real(q4);
        q4i=imag(q4);
        q44(i,:)=q4;
        q4r1(i,:)=q4r;
        q4i1(i,:)=q4i;



        %-----------------------------------------------------------
-------------------
        ng=2.98- 1.44i;

        % ngr=real(ng);
        % ngi=imag(ng);
        % er31r=((ngr).^2-(ngi).^2);
        er31=(ng^2);
        efff3=(q1.*er1)+(((1-q1).^2)./((q2./er2)+(q3./er31)+(1-q1-q2-
q3)));
        efff3r=real(efff3);
```

```matlab
        efff3i=imag(efff3);
        efff3r1(i,:)=efff3r;
        efff3i1(i,:)=efff3i;

        % er3=(er2.*q3.*(efff3-q1.*er1)./(er2.*(1-q1-q2).^2-(1-q1-q2-
q3).*(efff3-q1.*er1)));

        numer3=((efff3-q1.*er1).*er2.*q3);
        dener3=(((1-q1).^2).*er2-(q2+er2.*(1-q1-q2-q3)).*(efff3-
q1.*er1));
        er3=numer3./dener3;
        er3r=real(er3);
        er3i=imag(er3);
        er3r1(i,:)=er3r;
        er3i1(i,:)=er3i;

    end
%-----------------gamma alpha beta ----------------------------------
--------
G3=acosh(sqrt(((((1+sss11).*(1-
sss22))+(sss12.*sss21))./(2.*sss21)).*((((1-
sss11).*(1+sss22))+(sss12.*sss21))./(2.*sss21)))));
t_g3=tanh(G3);

A3=real(t_g3);
B3=imag(t_g3);
[thet3,rh3] = cart2pol(A3,B3);
alpha3=(1./(2.*l)).*atanh((2.*A3)./(1+abs(rh3).^2)); %Np/m
bet3=(1./(2.*l)).*atan((2.*B3)./(1-abs(rh3).^2));%/m
%---------------------------beta new-------------------------------
bd3=(2.*l.*((2.*pi.*freq3)./(3e8)).*(sqrt(efff3)));
Bgpc3=((2.*imag(t_g3))./(1-(abs(t_g3)).^2));% no unit
k3=ceil(((2.*l.*(bd3))-(atan(Bgpc3)))./180);

NB3=(((k3.*180)+((atan(Bgpc3).*(180./pi))))./(2.*l))./(2.*l); % deg/mm
NeB_rad3=((pi./180).*NB3);%rad/mm

x3=alpha3;
y3=NB3;
NeG1c3 = x3+1i*y3;
%------------------------Zc---------------------------------------
---
Zc33=Zo.*(sqrt((1+sss11+sss22+(sss11.*sss22)-(sss12.*sss21))./(1-
sss11-sss22+(sss11.*sss22)-(sss12.*sss21))));
if real(Zc33)<0
    Zc33=-Zc33;
else
    Zc33=1.*Zc33;
end
Zc3=smooth(Zc33);
%-----------------------------Erff-----------------------------
---
% g2=(2.*pi)./((3e8)./ff);
% go2=complex(0,g2);
ef3=((NeG1c3./go).^2);
ef3r=real(ef3);
ef3i=imag(ef3);
```

```
% er33=((ef3-q1.*er11).*er22.*q3)./(((q2+q3+q4).^2).*er22-
(q2+er22.*q4).*(ef3-q1.*er11));
% er33=(((ef3-q1.*er11).*er22.*q3)./(((1-q1).^2).*er22-(q2+er22.*(1-
q1-q2-q3)).*(ef3-q1.*er11)));


%numer3=((efff3-q1.*er1).*er2.*q3);
numer33=((ef3-q1.*er11).*er22.*q3);


%dener3=(((1-q1).^2).*er2-(q2+er2.*(1-q1-q2-q3)).*(efff3-q1.*er1));
dener33=(((1-q1).^2).*er22-(q2+er22.*(1-q1-q2-q3)).*(ef3-q1.*er11));
er33=numer33./dener33;
er33r=real(er33);
er33i=imag(er33);
%-----------------------------------------------------------------
----


%-----------------frequency from 1 to 499------------------------
-------
fr3=freq3(1:1:m2-1);
%---------Refractive Index----------------------------


N3=((sqrt((er33r).^2+(er33i).^2)+er33r)./2).^0.5;


%-----------Extinction coefficient------------------------
K3=(((sqrt((er33r).^2+(er33i).^2)-er33r)./2).^0.5);


%-------------Phase Velocity----------------------------
vp3=c./N3;


%---------Group Velocity----------------------------
% lambda03=c./freq3;
lambda03=c./(freq3.*sqrt(er33r));


y2=vp3;
x2=lambda03;
dydx_approx_for2=diff(y2)./diff(x2);
dydx_approx_back2=diff(y2)./diff(x2);
dydx_approx_gradient2=gradient(y2,x2);
dydx_approx_for2(length(x2))=NaN;
% dydx_approx_back=[NaN, dydx_approx_back];


figure(16);
plot(x2,dydx_approx_gradient2);
legend('centre difference formula');
legend('Location','NorthEast');
xlabel('lambda 0');
ylabel('dvp/dl0');
grid on;


vg3=vp3-(lambda03.*(dydx_approx_gradient2));


%-----------------Effective electron mass---------------
% NeB_rad33=NeB_rad3(2:2:end-1);
M3=((pc.*(NeB_rad3.*1000))./vg3);
% kgraphene=(2.*pi./lambda03);
% kgraphene33=kgraphene(2:2:end-1);
% M3=((pc.*(kgraphene.*1000))./vg3);
M3r=real(M3);
```

```
M3i=imag(M3);
%-------------------------------------------------------
figure(17);
plot(freq3/(10^9),ef3r,'blue',freq3/(10^9),efff3r1,'green',freq3/(10^9
));
legend('Efff 3(f) measured','Efff 3(f) formula');
legend('Location','NorthEast');
xlabel('Frequency(GHz)');
ylabel('Efff 3(f) real');
title('Efff 3(f) real Vs. Frequency ');
grid on;

figure(18);
plot(freq3/(10^9),ef3i,'blue',freq3/(10^9),efff3i1,'green',freq3/(10^9
));
legend('Efff 3(f) measured','Efff 3(f) formula');
legend('Location','NorthEast');
xlabel('Frequency(GHz)');
ylabel('Efff 3(f) imaginary');
title('Efff 3(f) imaginary Vs. Frequency ');
grid on;

figure(19);
plot(freq3/(10^9),er33r,'black',freq3/(10^9),er3r1,'-.black');
legend('Er3 measured ','Er3 formula');
legend('Location','NorthEast');
xlabel('Frequency(GHz)');
ylabel('Er3 real');
title('Er3 Vs. Frequency (For graphene on glass layer) ');
grid on;

figure(20);
plot(freq3/(10^9),er33i,'black',freq3/(10^9),er3i1,'-.black');
legend('Er3 measured ','Er3 formula');
legend('Location','NorthEast');
xlabel('Frequency(GHz)');
ylabel('Er3 imag');
title('Er3 Vs. Frequency (For graphene on glass layer) ');
grid on;

figure(21);
plot(freq3/(10^9),q3r1,'black',freq3/(10^9),q3i1,'-.red');
legend('q3 real','q3 imag');
legend('Location','NorthEast');
xlabel('Frequency(GHz)');
ylabel('q3');
title('q3 Vs. Frequency ');
grid on;

figure(22);
plot(freq3/(10^9),NB3,'black',freq3/(10^9),NeB_rad3,'-.red');
legend('NB3','NeB_rad3');
legend('Location','NorthEast');
xlabel('Frequency(GHz)');
ylabel('Beta');
title('Beta Vs. Frequency');
grid on;

figure(23);
```

```matlab
plot(freq3/(10^9),N3);
xlabel('Frequency(GHz)');
ylabel('n3');
title('n3 Vs. Frequency');
grid on;


figure(24);
plot(freq3/(10^9),K3);
xlabel('Frequency(GHz)');
ylabel('k3');
title('k3 Vs. Frequency ');
grid on;
%
figure(25);
plot(freq3/(10^9),vp3);
xlabel('Frequency(GHz)');
ylabel('vp3(m/s)');
title('Phase Velocity Vs. Frequency ');
grid on;


figure(26);
plot(freq3./(10^9),vg3);
xlabel('Frequency(GHz)');
ylabel('vg3 (m/s)');
title('Group Velocity Vs. Frequency ');
grid on;


figure(27);
plot(freq3./(10^9),M3r,'red');
legend('m3 real');
legend('Location','NorthEast');
xlabel('Frequency(GHz)');
ylabel('m3 (kg)');
title('Effective electron mass Vs. Frequency ');
grid on;



file_3=[freq3./(10.^9) ef3r ef3i efff3r1 efff3i1 er11r er11i er1r1
er1i1 er22r er22i er2r1 er2i1 er3r1 er3i1 er33r er33i q1r1 q1i1 q2r1
q2i1 q3r1 q3i1 N3 K3 vp3];
E_3 = {'Frequency(GHz)','Eff3(f) measured real','Eff3(f) measured
imag','Eff3(f) formula real','Eff3(f) formula imag','Er1 measured
real','Er1 measured imag','Er1 formula real','Er1 formula imag','Er2
measured real','Er2 measured imag','Er2 formula real','Er2 formula
imag','Er3 measured real','Er3 measured imag','Er3 formula real','Er3
formula imag', 'q1 real','q1 imag','q2 real','q2 imag','q3 real','q3
imag','Refractive index','Extinction coeff.','Phase velocity (m/s)'};
xlswrite('Results for third layer microstrip line.xlsx',E_3,1,'A1');
xlswrite('Results for third layer microstrip
line.xlsx',file_3,1,'A2');


file_33=[freq3./(10.^9) vg3 M3r M3i ];
E_33 = {'Frequency(GHz)','Group Velocity (m/s)','Effective electron
mass (kg) real' };
xlswrite('Group Velocity and Effective electron mass for third layer
microstrip line.xlsx',E_33,1,'A1');
xlswrite('Group Velocity and Effective electron mass for third layer
microstrip line.xlsx',file_33,1,'A2');
```
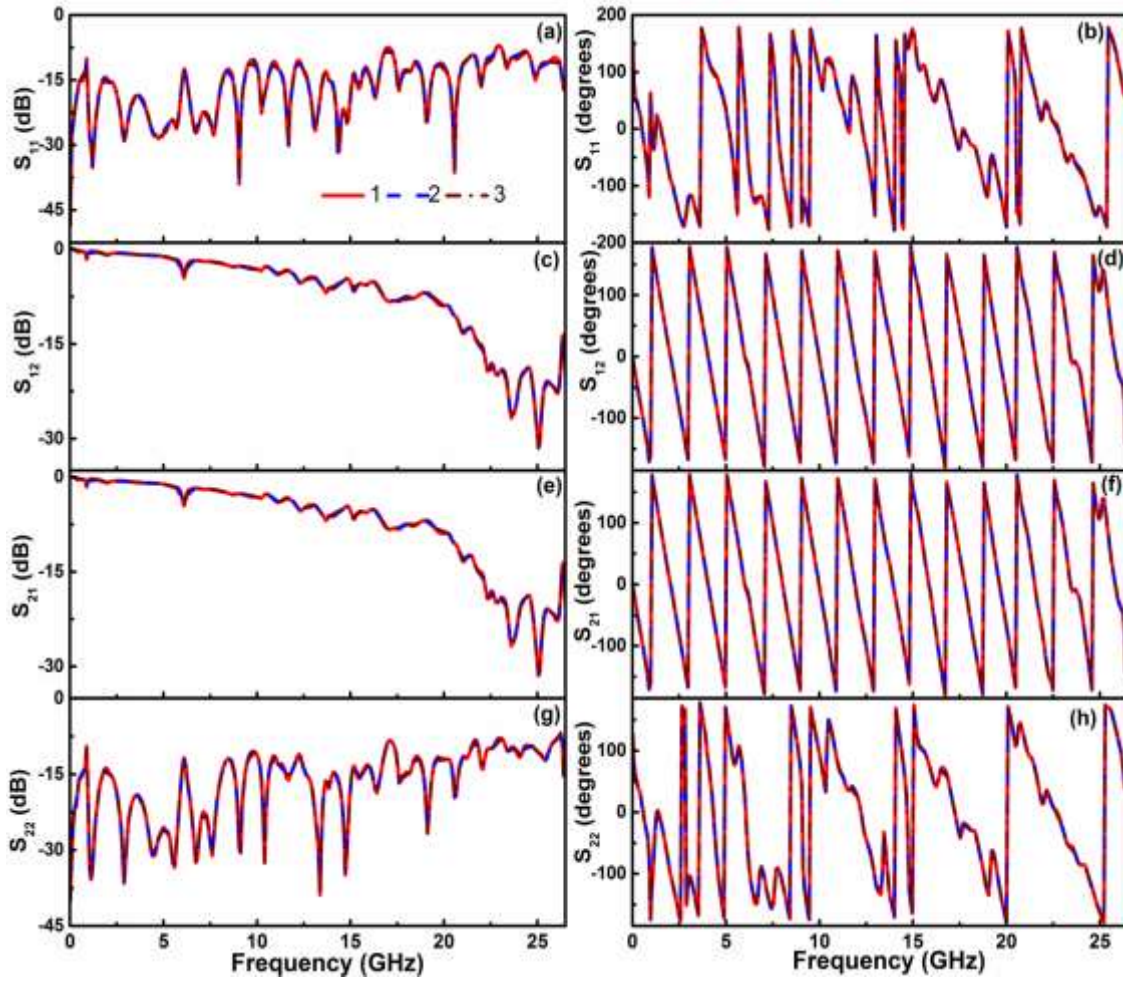
176

Appendix C

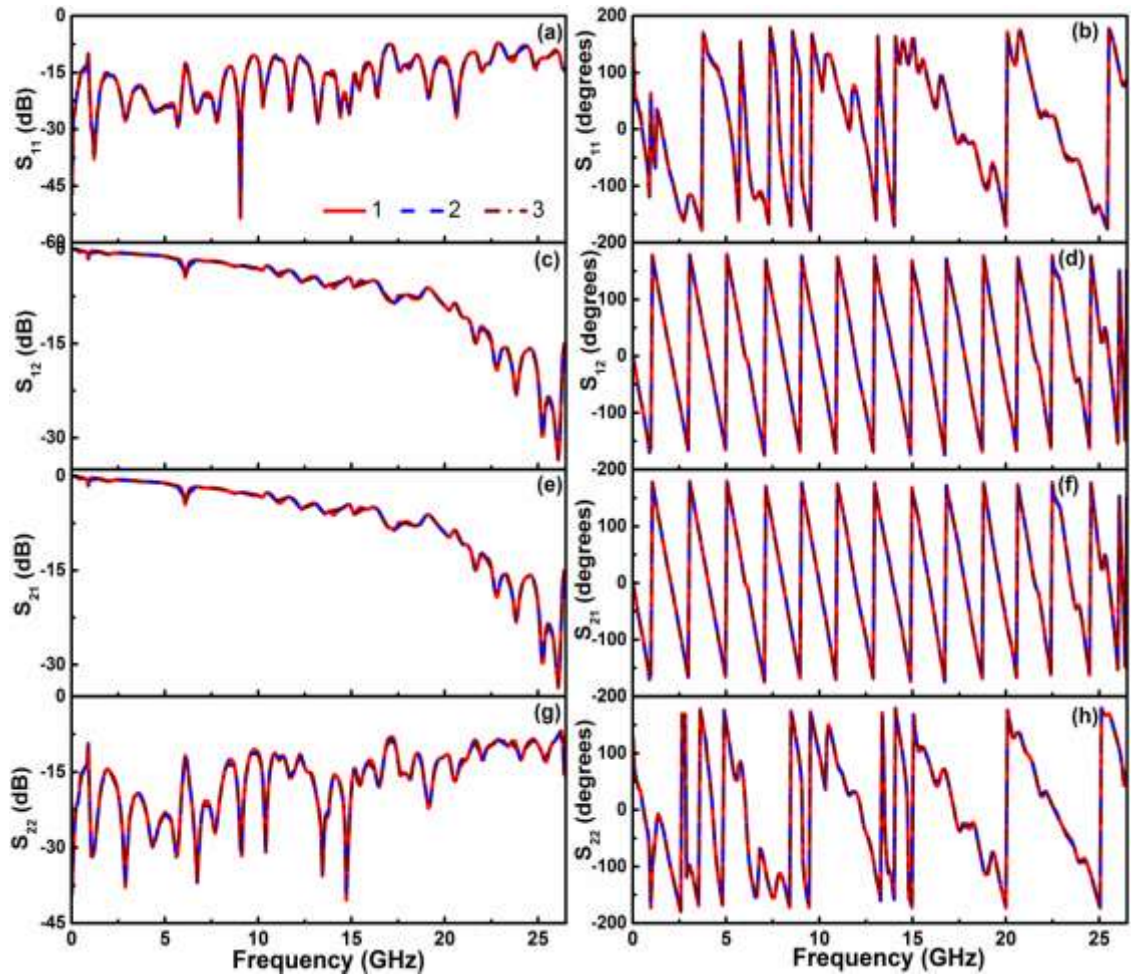## Three measurement results for estimating measurement error
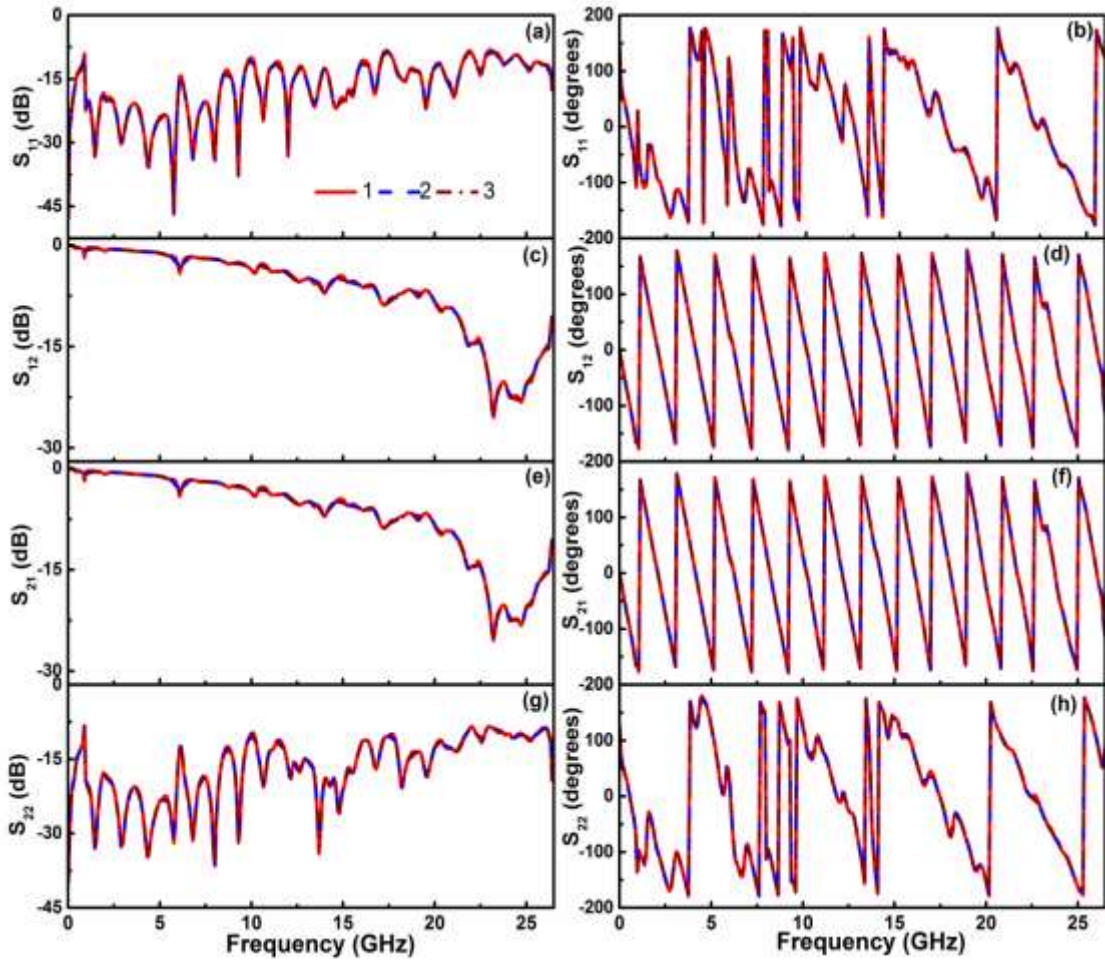
Fig. C1. Three measurement results for unloaded microstrip line, (a) magnitude of S_{11}, (b) phase of S_{11}, (c) magnitude of S_{12}, (d) phase of S_{12}, (e) magnitude of S_{21}, (f) phase of S_{21}, (g) magnitude of S_{22} and (h) phase of S_{22}.
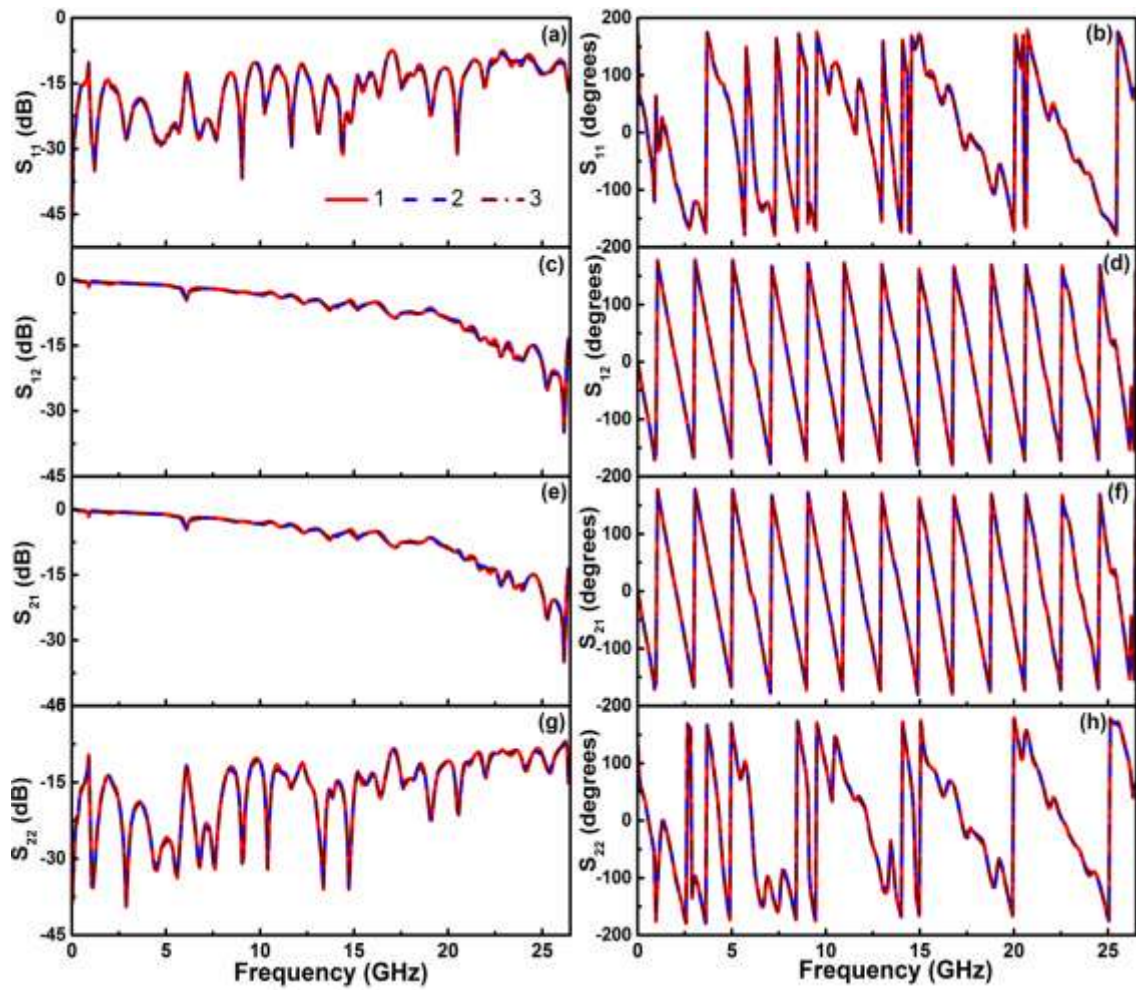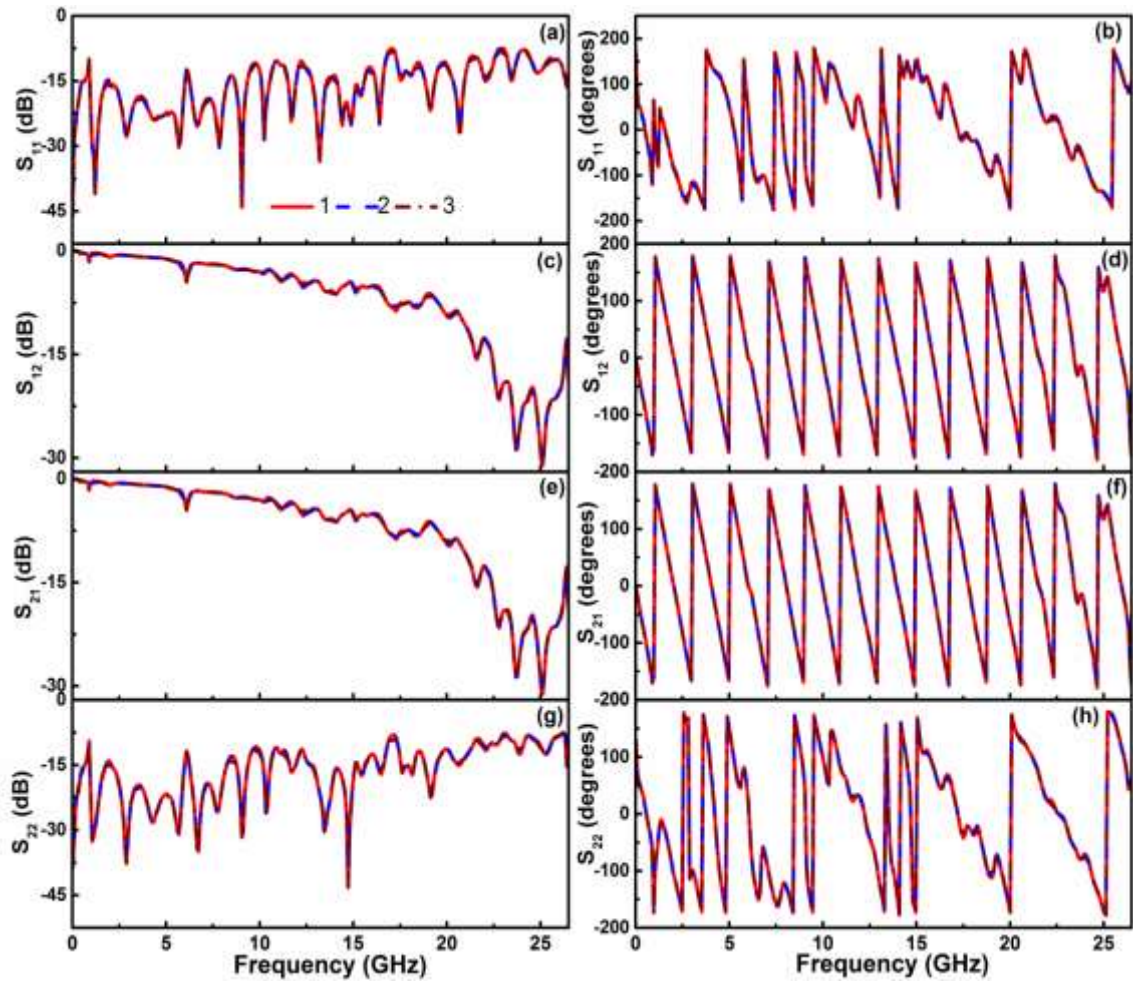
Fig. C2. Three measurement results for microstrip line loaded with glass, (a) magnitude of S_{11}, (b) phase of S_{11}, (c) magnitude of S_{12}, (d) phase of S_{12}, (e) magnitude of S_{21}, (f) phase of S_{21}, (g) magnitude of S_{22} and (h) phase of S_{22}.
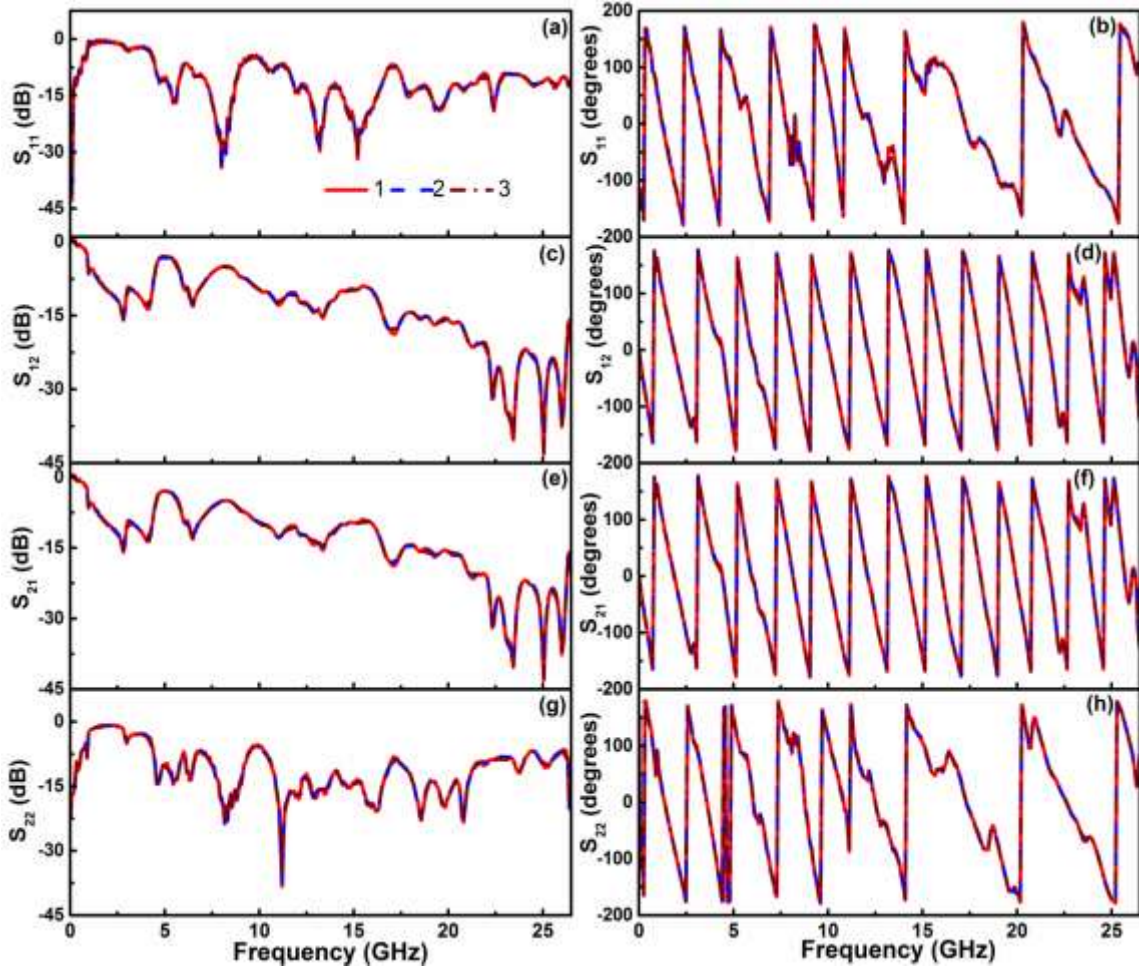
Fig. C3. Three measurement results for microstrip line loaded with quartz, (a) magnitude of S_{11}, (b) phase of S_{11}, (c) magnitude of S_{12}, (d) phase of S_{12}, (e) magnitude of S_{21}, (f) phase of S_{21}, (g) magnitude of S_{22} and (h) phase of S_{22}.

Fig. C4. Three measurement results for microstrip line loaded with SLG/glass, (a) magnitude of S_{11}, (b) phase of S_{11}, (c) magnitude of S_{12}, (d) phase of S_{12}, (e) magnitude of S_{21}, (f) phase of S_{21}, (g) magnitude of S_{22} and (h) phase of S_{22}.

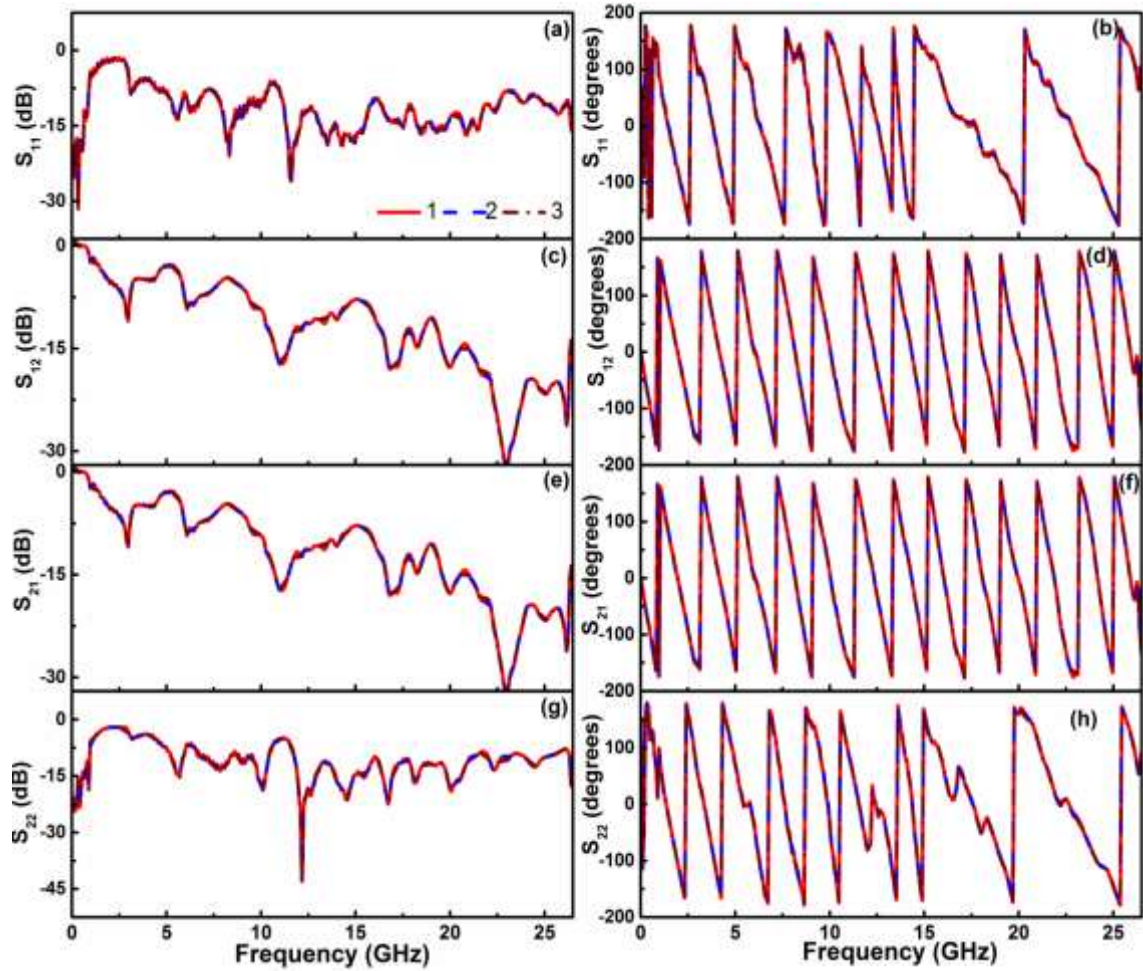**Fig. C5**. Three measurement results for microstrip line loaded with SLG/quartz, (a) magnitude of S_{11}, (b) phase of S_{11}, (c) magnitude of S_{12}, (d) phase of S_{12}, (e) magnitude of S_{21}, (f) phase of S_{21}, (g) magnitude of S_{22} and (h) phase of S_{22}.

Fig. C6. Three measurement results for microstrip line loaded with BLG/Cu$_1$, (a) magnitude of S$_{11}$, (b) phase of S$_{11}$, (c) magnitude of S$_{12}$, (d) phase of S$_{12}$, (e) magnitude of S$_{21}$, (f) phase of S$_{21}$, (g) magnitude of S$_{22}$ and (h) phase of S$_{22}$.

Fig. C7. Three measurement results for microstrip line loaded with BLG/Cu$_2$, (a) magnitude of S_{11}, (b) phase of S_{11}, (c) magnitude of S_{12}, (d) phase of S_{12}, (e) magnitude of S_{21}, (f) phase of S_{21}, (g) magnitude of S_{22} and (h) phase of S_{22}.

Table C1- Maximum measurement errors (±) associated with mean of three results for all samples shown in Fig. C1 to C7

Parameter values with maximum standard deviation	S_{11}(dB)	S_{11}(degrees)	S_{12}(dB)	S_{12}(degrees)	S_{21}(dB)	S_{21}(degrees)	S_{22}(dB)	S_{22}(degrees)
Unloaded microstrip line	- 46.38 ± 0.50	141.39 ± 2.07	- 25.43 ± 0.05	76.57 ± 0.37	- 22.49 ± 0.4	82.61 ± 0.27	-39.57 ± 0.15	44.83 ± 0.86
Glass loaded microstrip line	- 48.38 ± 0.21	96.99 ± 1.95	- 30.75 ± 0.04	138.68 ± 0.45	- 31.47 ± 0.05	138.82 ± 0.38	- 38.74 ± 0.12	- 91.11 ± 0.42
Quartz loaded microstrip line	- 53.00 ±1.28	**- 92.49 ±5.21**	- 31.08 ±0.12	- 94.94 ±0.71	- 28.50 ±0.09	151.98 ±1.08	- 40.28 ±0.12	12.46 ±1.97
SLG/glass loaded microstrip line	- 30.94 ± 0.18	- 169.47 ± 0.85	- 34.97 ± 0.08	- 153.99 ± 0.39	- 34.92 ± 0.13	38.16 ± 0.38	- 33.77 ± 0.12	- 44.49 ± 0.77
SLG/quartz loaded microstrip line	43.87 ± 0.20	- 72.29 ± 1.47	- 26.46 ± 0.07	- 22.69 ± 0.25	- 31.09 ± 0.07	-15.57 ± 0.42	43.16 ± 0.28	38.64 ± 0.79
BLG/Cu$_1$ loaded microstrip line	**- 25.47 ± 1.72**	**- 41.27 ± 4.60**	- 40.06 ± 0.54	111.23 ± 2.68	- 40.14 ± 0.58	81.16 ± 2.80	**- 36.97 ± 1.74**	172.24 ± 3.71
BLG/Cu$_2$ loaded microstrip line	- 25.28 ± 0.19	- 177.04 ± 2.50	- 32.83 ± 0.17	- 167.28 ± 1.03	- 30.21 ± 0.14	-160.03 ± 0.94	- 20.94 ± 0.33	- 66.83 ± 3.44

Brief bio-data of the Research Scholar

Kamlesh Patel

Research Scholar
Department of Applied Physics
Delhi Tecnological University
Delhi, India

Qualifications:

- **Ph.D. (Applied Physics):** 2011- Present,Delhi Tecnological University
  Dissertation: "Characterization and applications of cvd-grown graphene for passive microwave devices"

- **M.Tech. (Microwave Electronics)**: 2001-2003, University of Delhi, Delhi

- **M. Sc. (Electronics)**: 1997-1999, Rani Durgavati University, Jabalpur, MP

Research Interest: Microwave and RF component and characterization, Microwave properties of materials, Thin film solar cells.

Publications:

- Journal publications: **24**
- Conference proceedings: **6**

Software skills: ANSYS HFSS, QUCS, CST

Research Project Grants:

S. No.	Funding agencies	Project Title	Duration	Grant Received
1.	University of Delhi	Characterization and Application of Graphene at the Microwave frequencies	2014-2015	Rs.2.3 Lakhs
2.	University of Delhi	Simulation, fabrication of Coplanar waveguide components and characterization with graphene	2015-2016	Rs. 3.0 Lakhs

Expert: Laboratory Assessor (ISO 17025:2005) for RF calibration, National Accreditation Board of Testing & Calibration Laboratories (NABL), Department of Science & Technology, India.

Work Experience:

Organization	Designation	Duration	Role
Dept. of Electronic Science, University of Delhi South Campus New Delhi	Assistant Professor	21.05.2013 -till date	Teaching & Research
National Physical Laboratory, New Delhi	Scientist	01.10.2004 to 20.05.2013	i) Apex level calibration and dissemination of RF standards ii) R & D for the advancement of microwave standards iii) R & D in thin film silicon solar cells
The Scientific Instruments Company Ltd. (SICO), Ghaziabad, U.P.	Engineer	Sept 2003-Sept 2004	Design, development of MIC components, testing of microwave waveguide components
St. Aloysius' College, Jabalpur, M.P.	Adhoc Lecturer	Aug 2000-Apr 2001	Teaching & Practical In-charge: Graduate courses in Electronics
Dept. of Physics & Electronics, Rani Durgavati University, Jabalpur	Adhoc Lecturer	Sept 1999-Apr 2000	Teaching Post Graduate courses in Electronics

Training Received:

❑ Awareness cum Implementation training programme on "**Laboratory Accreditation under ISO 17025:2005**" from 1st to 2nd Sept 2005 at CDC, New Delhi.

❑ Training Course on **"Evaluation and Expression of Uncertainty in Measurements"** on 13th Sept 2005 at National Physical Laboratory, New Delhi.

❑ **"Laboratory Assessor course (NABL)"** from 08th to 12th October 2007 at National Physical Laboratory, New Delhi.

❑ **"Attachment Training on attenuator calibration"** from 13th to 17th Oct 2008 at **National Measurement Institute (NMI) Australia**.

❑ **"Leadership Development Programme"** from05^{th} to 17th Dec 2009 (Module 2) and 07th to 11th 2010 (Module 3) at HRDC (CSIR), Ghaziabad, UP.

Membership of Professional Bodies:

- Member, IEEE

Life Member –

- Metrology Society of India
- Material Research Society of India
- Solar Energy Society of India